

# UC San Diego

## UC San Diego Electronic Theses and Dissertations

### Title

Effects of ductile phase volume fraction on the mechanical properties of Ti-Al<sub>3</sub>Ti metal-intermetallic laminate (MIL) composites

### Permalink

<https://escholarship.org/uc/item/0bg5t877>

### Author

Price, Richard David

### Publication Date

2010

Peer reviewed|Thesis/dissertation

UNIVERSITY OF CALIFORNIA, SAN DIEGO

Effects of Ductile Phase Volume Fraction on the Mechanical Properties of  
Ti-Al<sub>3</sub>Ti Metal-Intermetallic Laminate (MIL) Composites

A Thesis submitted in partial satisfaction of the requirements for the degree Master of Science

in

Engineering Sciences (Mechanical Engineering)

by

Richard David Price

Committee in charge:

Professor Kenneth S. Vecchio, Chair  
Professor Vlado Lubarda  
Professor David J. Benson

2010

Copyright

Richard David Price, 2010

All rights reserved.

The Thesis of Richard David Price is approved and it is acceptable in quality and form for publication on microfilm and electronically:

---

---

---

Chair

University of California, San Diego

2010



*Dedicated to*

My family and friends

*With special thanks to*

Jiang, Heesh, and Robb

Boy, ain't nothin' easy.

*F. Arnall*

## TABLE OF CONTENTS

Signature Page.....	iii
Dedication .....	iv
Epigraph.....	v
Table of Contents .....	vi
List of Figures .....	ix
List of Tables.....	xvi
Acknowledgements .....	xvii
Abstract of the Thesis.....	xviii
Chapter 1 Introduction .....	1
Chapter 2 Background.....	4
2.1 Metal-Intermetallic Laminate Composite Materials .....	4
2.2 Synthesis of Ti-Al <sub>3</sub> Ti Laminate Composites.....	7
2.2.1 Review of Synthesis Methods .....	7
2.2.2 Reactive Foil Sintering.....	13
2.3 Ductile/Brittle Modeling .....	15
2.3.1 Toughening Mechanisms in MIL Composites .....	15
2.3.2 Ductile/Brittle Reinforcement .....	22
2.3.3 Resistance Curve Behavior .....	24
2.3.4 Laminate Failure.....	25
2.4 Previous Research in Ti-Al <sub>3</sub> Ti MIL Composites .....	28

Chapter 3	Experimental Procedure.....	30
3.1	Materials and Processing.....	30
3.1.1	Materials Used.....	30
3.1.2	Sample Preparation.....	31
3.1.3	Synthesis Apparatus .....	31
3.1.4	Processing Method .....	32
3.2	Characterization and Microscopy.....	33
3.3	Mechanical Testing .....	34
3.3.1	Quasi-Static Compression Testing .....	34
3.3.2	Quasi-Static Four Point Bend Testing.....	36
3.3.3	High Strain-Rate Compression Testing.....	40
3.3.4	High Strain-Rate Four Point Bend Testing .....	41
Chapter 4	Results and Discussion .....	45
4.1	MIL Composite Physical Properties.....	45
4.1.1	Composites Produced .....	45
4.1.2	Phases Present .....	48
4.2	Mechanical Properties .....	52
4.2.1	Quasi-Static Compression Testing .....	52
4.2.1.1	Layers Parallel to the Applied Load.....	54
4.2.1.2	Layers Perpendicular to the Applied Load.....	63
4.2.2	Quasi-Static Four Point Bend Testing.....	71

4.2.2.1	Layers Parallel to the Applied Load.....	73
4.2.2.2	Layers Perpendicular to the Applied Load.....	80
4.2.3	High Strain-Rate Compression Testing.....	90
4.2.3.1	Layers Parallel to the Applied Load.....	91
4.2.3.2	Layers Perpendicular to the Applied Load.....	97
4.2.4	High Strain-Rate Four Point Bend Testing .....	103
4.2.4.1	Layers Parallel to the Applied Load.....	104
4.2.4.2	Layers Perpendicular to the Applied Load.....	112
Chapter 5	Summary and Conclusions .....	120
5.1	Specimens Produced.....	120
5.2	Compression Testing.....	121
5.3	Four Point Bend Testing.....	122
5.4	Conclusions .....	124
Chapter 6	Future Work.....	126
References	.....	127

## LIST OF FIGURES

Figure 2.1 – Temperature dependence of (a) the compressive yield stress and (b) tensile elongation of several Ti-Al compounds [17].....	5
Figure 2.2 – Temperature dependence of ductility of some intermetallic compounds with high melting points [19]. .....	6
Figure 2.3 – The Ti-Al phase diagram showing the location of Al <sub>3</sub> Ti [21]. .....	7
Figure 2.4 – Microstructure of the Ti-Al layered composite produced in vacuum from 0.15 mm thick Ti and Al foils at (a) low magnification and (b) high magnification [24]. .....	9
Figure 2.5 – Effect of initial foil thickness on the tensile behavior of a Ti-Al <sub>3</sub> Ti MIL composite fabricated in vacuum via SHS [24]. .....	9
Figure 2.6 – Optical micrograph of MIL composite microstructure formed by reactive foil metallurgy. HIP reaction at (a) 1300 °C, 65 min and 2000 bar and (b) 1390 °C, 70 min and 2000 bar [27]. .....	10
Figure 2.7 – Layered structure of two composites formed from a pulsed-current hot pressing method. The presence of several other aluminide layers can be seen in the magnified images [28].....	12
Figure 2.8 – Intermetallic layer thickness vs. reaction time based on interrupted reaction studies of the reactive foil sintering process [29]. .....	14
Figure 2.9 – EDS spectra across an entire intermetallic layer of a sample prepared by reactive foil sintering confirming the intermetallic region is Al <sub>3</sub> Ti with no other phases present [29].....	15
Figure 2.10 – Diagram of mutual competition between intrinsic mechanisms of damage/crack advance and extrinsic mechanisms of crack-tip shielding involved in crack growth [38].....	16
Figure 2.11 – Extrinsic toughening mechanisms for laminated metal composites [36].....	18
Figure 2.12 – Schematic diagram illustrating crack bridging: (a) crack-arrester orientation and (b) crack-divider orientation. Planes AA and BB indicate cross sections of the laminate composite near the crack tip. The arrows between the planes indicate bridging tractions over the length of <i>b</i> [39].....	20
Figure 2.13 – The apparent fracture toughness as a function of the crack length parameter $\tilde{a}$ in a laminate with an outer layer under residual compressive stress [40]. .....	21
Figure 2.14 – Crack bridging process caused by intercepted ductile particles and a process zone of plastically distorted ductile particles [37].....	22

Figure 2.15 – Moment-Displacement curves showing delamination (a) after and (b) before crack extension [48].	27
Figure 2.16 – SEM micrographs showing the aluminum oxides ( $\text{Al}_2\text{O}_3$ ) and microvoids in MIL composites constructed with (a) Ti-6Al-4V and (b) commercially pure Ti. [51]	29
Figure 3.1 – Rendering of the synthesis apparatus (not to scale).	32
Figure 3.2 – Apparatus used in quasi-static compression testing.	35
Figure 3.3 – Schematic diagram of the typical dimensions of samples used in 4PB tests. Dimensions in millimeters.	35
Figure 3.4 –Schematic diagrams of SE(B) in (a) crack-arrester and (b) crack-divider orientations	36
Figure 3.5 – Novel apparatus designed to test small samples in quasi-static 4PB: (a) overall setup in the load frame; (b) close-up of the bending area. As the crack opens, the sample pushes down on the shaft and tab, which is recorded by the deflectometer.	37
Figure 3.6 – Photographs of (a) broken and unbroken crack-divider samples and (b) the end-on view of the fracture surface. (c) SEM image of the notch depth measurement of a crack-divider sample.	39
Figure 3.7 – Split-Hopkinson Pressure Bar with pulse shaper and momentum trap used for high strain-rate compression and bend testing [55].	40
Figure 3.8 – (a) Schematic of the sample mounting setup. (b) SHPB setup for dynamic fracture toughness experiments: (1) photo gate trigger, (2) pulse shaper, (3) strain gage, (4) SE(B) specimen, (5) lighting for (6) high speed camera, (7) data acquisition, (8) power supply [59].	43
Figure 3.9 – (a) Photograph showing strain gage placement. (b) Schematic of the strain-gage amplifier [39].	44
Figure 4.1 – The effect of processing time on (a) layer thickness and (b) volume fraction.	46
Figure 4.2 – MIL composite specimens produced via reactive foil sintering. SEM micrographs taken of specimens (a) MIL-48, (b) MIL-42, (c) MIL-16, (d) MIL-11, (e) MIL-3, and (f) MIL-1.	47
Figure 4.3 – SEM micrograph of the Al layer of specimen MIL-11 showing the points used in EDS analysis.	49
Figure 4.4 – SEM micrograph of a broken portion of the Al layer of specimen MIL-3 showing the points used in EDS analysis.	50

Figure 4.5 – SEM micrograph of a broken and segmented portion of the Al layer of specimen MIL-1 showing the points used in EDS analysis. ....	51
Figure 4.6 – SEM micrographs of crack propagation and creep caused by residual thermal stresses in (a) MIL-3 and (b) MIL-1.....	51
Figure 4.7 – Affect of residual aluminum volume fraction on compressive stress in parallel and perpendicular loading orientations.....	53
Figure 4.8 – Representative stress-strain curves of each specimen tested under quasi-static compression at 0.001/s with layers oriented parallel to the applied load. ....	54
Figure 4.9 – SEM micrograph of MIL-48 sample (cold-mounted and polished after quasi-static compression) showing (a) buckling and (b) minor delamination cracking near the load face.....	55
Figure 4.10 – SEM micrograph of MIL-42 sample under quasi-static compression (0.001/s) in parallel loading showing Al <sub>3</sub> Ti centerline cracking, shear band formation, and transverse cracking at regions of (a) large and (b) small deformation. ....	55
Figure 4.11 – Fracture of MIL-16 under quasi-static compression (0.001/s) with layers oriented parallel the applied load: (a) cracked Al-Al <sub>3</sub> Ti layers and intact Ti layers, (b) magnification of fracture surface, (c) crack bridging by Al layer and shear band formation (arrows).....	57
Figure 4.12 – Diagram of two modes of shear failure common to MIL composites loaded parallel to the layers: (a) bisecting shear fracture propagating from interface to interface (a-type); (b) shear fracture that cuts diagonally across all layers of the composite simultaneously (b-type) [51]......	58
Figure 4.13 – Fracture of MIL-11 under quasi-static compression (0.001/s) with layers oriented parallel to the applied load. SEM micrographs showing: (a) crack blunting in Al layer; (b) magnification of microcracking and plastic deformation; (c) fracture without clean delamination .....	59
Figure 4.14 – Fracture of MIL-3 under quasi-static compression (0.001/s) with layers oriented parallel to the applied load. SEM micrographs showing: (a) ductile Ti buckling and brittle Al <sub>3</sub> Ti fracture ignoring the residual Al, (b) transverse cracking in Al <sub>3</sub> Ti, (c) and (d) unique crack opening in intermetallic bilayers. ....	61
Figure 4.15 – SEM micrograph of MIL-1 showing: (a) and (b) a-type shear fracture with and without Ti layer failure (unpolished sample); (c) and (d) transverse cracking and Al <sub>3</sub> Ti bilayer delamination from Ti layers (sample polished prior to testing)...	62
Figure 4.16 – Representative stress-strain curves of each specimen tested under quasi-static compression at 0.001/s with layers oriented perpendicular to the applied load. ....	63
Figure 4.17 – SEM micrographs of MIL-48 and (a) stopped before the failure strain showing small scale delamination, and (b) macroscopic deformation and Al expulsion of a failed sample.....	64



Figure 4.18 – SEM micrograph of MIL-42 showing: (a) arrested a-type shear fracture, (b) intermetallic cracking and segmentation, (c) aluminum expulsion, and (d) stress relief cracking and delamination (pre-fail).....	65
Figure 4.19 – SEM micrograph of MIL-16 showing: (a) a-type shear fracture; (b) intermetallic segmentation, Ti deformation, ductile Al reinforcement; (c) and (d) shear band formation in a sample stopped between yield and failure strain. ....	66
Figure 4.20 – SEM micrographs comparing catastrophic failure and cracking before failure in (a), (b) MIL-11 and (c), (d) MIL-3.....	69
Figure 4.21 – SEM micrographs of MIL-1: (a) and (b) catastrophic failure by a-type shear fracture; (c) Al <sub>3</sub> Ti crack ignored residual Al centerline in a sample stopped before failure. ....	70
Figure 4.22 – Affect of residual aluminum volume fraction on fracture toughness in parallel and perpendicular loading orientations.....	72
Figure 4.23 – Representative stress-strain curves of each specimen tested under quasi-static 4PB at 0.001/s with layers oriented parallel to the applied load. ....	73
Figure 4.24 – SEM micrograph of the fracture surface of MIL-48 in quasi-static bending showing ductile fracture, tearing, and delamination.....	74
Figure 4.25– SEM micrographs of the fracture surface of MIL-42 crack divider samples in quasi-static bending. (a) Ductile fracture of Ti layers, Al layer tearing, and Al <sub>3</sub> Ti layer cracking. (b) Detail of image (a) showing Al <sub>3</sub> Ti cracking. (c) Segmented Al <sub>3</sub> Ti fragments still bonded to Al layer .....	75
Figure 4.26 – SEM micrographs of the fracture surfaces of MIL-16 in the crack divider orientation after quasi-static 4PB testing showing stair step Al <sub>3</sub> Ti fracture and slanted Ti fracture.....	77
Figure 4.27 – SEM micrographs of the fracture surfaces of (a)-(c) MIL-11 and (d)-(f) MIL-3 in the crack divider orientation after quasi-static 4PB testing .....	78
Figure 4.28 – SEM micrographs of the fracture MIL-1 in the crack divider orientation after quasi-static 4PB testing: (a) overview of fracture surface showing a higher percentage of Al <sub>3</sub> Ti flat cleavage fracture; (b) magnified image showing Al <sub>3</sub> Ti delamination from residual Al; (c) magnified image. ....	79
Figure 4.29 – Photograph of an arrester samples from each specimen after testing in quasi-static 4PB. Notice the lack of fracture in the notch direction. ....	80
Figure 4.30 – Representative stress-strain curves of each specimen tested under quasi-static 4PB at 0.001/s with layers oriented perpendicular to the applied load. ....	81
Figure 4.31 – SEM micrographs of MIL-48 arrester samples after quasi-static 4PB testing showing the surface texture of a delaminated layer of aluminum. ....	81

Figure 4.32 – SEM micrographs of MIL-42 arrester samples after quasi-static 4PB testing showing: (a) ductile crack termination without significant microstructural damage; (b) Al delamination and plastic deformation, and (c) Ti necking and fracture at the notch nip. ....	82
Figure 4.33 – Failure of MIL-16 crack-arrester samples under quasi-static 4PB. (a) and (b) show vertical intermetallic cracking and shear band formation in the Ti layers. (c-e) show plastic deformation and Al and Ti crack tip bridging. ....	84
Figure 4.34 – Failure of MIL-11 crack-arrester samples under quasi-static 4PB. (a) and (b) show vertical intermetallic cracking and shear band formation in the Ti layers. (c) and (d) show plastic deformation and Al and Ti crack bridging. ....	85
Figure 4.35 – Failure of MIL-3 crack-arrester samples under quasi-static 4PB. (a) Stitched panorama of the transverse delamination that propagated from the crack tip and (b, c) cracking and arresting at the tip. (d) Optical micrograph of the region in (b) showing shear band deformation and crack bridging by Ti layers. ....	87
Figure 4.36 – Failure of MIL-1 crack-arrester samples under quasi-static 4PB. SEM micrographs of: (a) significant $Al_3Ti$ cracking without propagation of a single fracture; (b) delamination and fracture at the notch tip; (c) inter- and intragranular fracture of $Al_3Ti$ grains near the crack tip. ....	88
Figure 4.37 – Optical micrographs showing the failure evolution of four crack-arrester samples after quasi-static 4PB. Notice the increasing microstructural damage from MIL-16 to MIL-3 as the residual Al content decreases. ....	89
Figure 4.38 – Affect of residual aluminum volume fraction on compressive yield stress in dynamic testing of parallel and perpendicular loading orientations. ....	91
Figure 4.39 – Representative stress-strain curves of each specimen tested under dynamic compression at 1000/s with layers oriented parallel to the applied load. ....	92
Figure 4.40 – SEM micrograph of MIL-48 cold-mounted and polished after dynamic compression showing large scale delamination and buckling without shear fracture. ....	93
Figure 4.41 – SEM micrographs of MIL-42 cold-mounted and polished after dynamic compression showing (a) large scale delamination, buckling, and (b) $Al_3Ti$ centerline fracture. Light layers are Ti, dark layers are Al. ....	93
Figure 4.42 – SEM micrographs of MIL-16 cold-mounted and polished after dynamic compression showing (a) delamination cracking, buckling, and (b) $Al_3Ti$ centerline fracture. ....	94
Figure 4.43 – SEM micrographs of MIL-11 cold-mounted and polished after dynamic compression showing (a, b) intermetallic layer reinforcement by plastic deformation of Ti layers, and (c) $Al_3Ti$ centerline fracture. ....	95

Figure 4.44 – SEM micrographs of MIL-3 cold-mounted and polished after dynamic compression showing (a) shear fracture, buckling, and (b) Al <sub>3</sub> Ti centerline fracture. ....	95
Figure 4.45 – (a) and (b) are SEM micrographs of MIL-1 cold-mounted and polished after dynamic compression showing failure by delamination at the intermetallic centerline (arrows).....	96
Figure 4.46 – Representative stress-strain curves of each specimen tested under dynamic compression at 1000/s with layers oriented perpendicular to the applied load. ....	97
Figure 4.47 - SEM micrographs of MIL-48 cold-mounted and polished after dynamic compression showing .....	99
Figure 4.48 - SEM micrographs of MIL-42 cold-mounted and polished after dynamic compression showing .....	100
Figure 4.49 - SEM micrographs of MIL-16 cold-mounted and polished after dynamic compression showing (a) shear fracture and (b) and magnified image of intermetallic cracking and Ti shear deformation.....	100
Figure 4.50 - SEM micrographs of MIL-11 cold-mounted and polished after dynamic compression showing (a) shear fracture and (b) and magnified image of intermetallic cracking and Ti shear deformation.....	101
Figure 4.51 - SEM micrograph of MIL-3 cold-mounted and polished after dynamic compression showing a lack of intermetallic cracking.....	101
Figure 4.52 - SEM micrographs of MIL-1 cold-mounted and polished after dynamic compression showing .....	102
Figure 4.53 – Affect of residual aluminum volume fraction on racture toughness $K_{IC}$ in parallel and perpendicular loading orientations. The parallel orientation curves generated by the high-speed camera and strain gage methods show almost identical trends. ....	104
Figure 4.54 – Representative load-time curves of each specimen tested under high strain-rate 4PB with layers oriented parallel to the applied load.....	105
Figure 4.55 – SEM micrographs of the fracture surface of MIL-48 in dynamic 4PB showing: (a) a fracture surface similar to quasi-static 4PB samples; (b) Al layer tearing, and Ti layer microvoid coalescence and slant fracture; (c) the thin intermetallic layer still bonded to the Ti layer.....	107
Figure 4.56 – SEM micrographs of the fracture surface of MIL-42 in dynamic 4PB showing: (a) wide-spread ply separation and intermetallic segmentation; (b) and (c) magnifications of intermetallic segmentation.....	108

Figure 4.57 – SEM micrographs of the fracture surfaces of MIL-16 in the crack divider orientation after dynamic 4PB testing showing (a) stair-step Al <sub>3</sub> Ti fracture and slanted Ti fracture. (b) Magnification of (a).....	108
Figure 4.58 – SEM micrographs of the fracture surface of MIL-11 after dynamic 4PB testing showing: (a) less interfacial fracture than MIL-16; (b) and (c) the Al centerline prevented transverse fracture of the Al <sub>3</sub> Ti bilayers. ....	109
Figure 4.59 – SEM micrographs of the fracture surface of MIL-3 after dynamic 4PB testing showing: (a) increased presence of intermetallic flat cleavage fracture; (b) and (c) the residual Al centerline (indicated by arrows) was not thick enough to prevent transverse fracture in the Al <sub>3</sub> Ti bilayers. ....	110
Figure 4.60 – SEM micrographs of the fracture surface of MIL-1 after dynamic 4PB testing showing: (a), (b), (d) emergence of intermetallic centerline fracture as a primary failure mechanism; (c) plastic tearing of the Ti layer; (e) magnified image of (d) showing inter- and intragranular (arrows) cracking. ....	111
Figure 4.61 – Optical micrograph of a broken strain gage spanning the transverse crack of a crack-arrester sample.....	112
Figure 4.62 – Representative load-time curves of each specimen tested under high strain-rate 4PB with layers oriented perpendicular to the applied load. ....	113
Figure 4.63 – High-speed camera images showing the failure of (a, b) MIL-48 and (c, d) MIL-42 crack-arrester samples under dynamic 4PB.....	114
Figure 4.64 – Optical micrographs depicting the evolution of failure of MIL-16, MIL-11, MIL-3, and MIL-1 crack-arrester samples under dynamic 4PB. Microstructural damage increases up to MIL-1, where delamination plays a larger role. ....	116
Figure 4.65 – (a) High-speed camera images showing the failure of MIL-11 under dynamic 4PB. (b) Optical micrograph of the notch tip seen in (a) at 222 microseconds.....	117
Figure 4.66 – (a) High-speed camera images showing the failure of MIL-3 under dynamic 4PB. (b) Optical micrograph of the notch tip seen in (a) at 222 microseconds.....	118
Figure 4.67– (a) High-speed camera images showing the failure of MIL-1 under dynamic 4PB. (b) Optical micrograph of the notch tip seen in (a) at 222 microseconds.....	119

## LIST OF TABLES

Table 3.1 – Chemical compositions and properties of components.....	30
Table 3.2 – Temperature profile for each sample (in °C).....	33
Table 4.1 – Specimens produced: designation and microstructure. ....	45
Table 4.2 – Composition of the residual aluminum layer of MIL-11 determined by EDS.....	49
Table 4.3 – Composition of the residual aluminum layer of MIL-3 determined by EDS.....	50
Table 4.4 – Composition of the residual aluminum layer of MIL-1 determined by EDS.....	51
Table 4.5 – Summary of yield stresses observed in quasi-static compression testing. ....	53
Table 4.6 – Summary of fracture toughness values observed in quasi-static 4PB testing. ....	72
Table 4.7 – Summary of yield stresses observed in dynamic compression testing.....	90
Table 4.8 – Summary of fracture toughness values observed in dynamic 4PB testing.....	103
Table 5.1 – Summary of average yield stresses observed in quasi-static and dynamic compression.....	121
Table 5.2 – Summary of average toughness values observed in quasi-static and dynamic 4PB testing.....	124

## ACKNOWLEDGEMENTS

I would like to cordially thank Dr. Vecchio, my boss and advisor, for hiring me as an undergrad, for giving me the opportunity to research such an interesting topic, and for helping me get out as soon as possible.

Special thanks are due to the researchers I have had the privilege of working with: Fengchun Jiang for his invaluable advice and tireless assistance throughout, Robb Kulin for his technical input and high-speed camera expertise, Tsukasa Takahashi for his commiseration and encouragement, and Hesham “Heesh” Khalifa for all the questions he answered and wisdom he shared. I would not have finished without their help.

My family, who with their prayers kept me alive, and my friends, who despite my complaining supported me, deserve any and all remaining credit for my success.

Chapter 1, in part, is currently being prepared for submission for publication of the material. The dissertation author was the primary investigator and author of this material.

Chapter 2, in part, is currently being prepared for submission for publication of the material. The dissertation author was the primary investigator and author of this material.

Chapter 3, in part, is currently being prepared for submission for publication of the material. The dissertation author was the primary investigator and author of this material.

Chapter 4, in part, is currently being prepared for submission for publication of the material. The dissertation author was the primary investigator and author of this material.

Chapter 5, in part, is currently being prepared for submission for publication of the material. The dissertation author was the primary investigator and author of this material.

Chapter 6, in full, is currently being prepared for submission for publication of the material. The dissertation author was the primary investigator and author of this material.

## ABSTRACT OF THE THESIS

Effects of Ductile Phase Volume Fraction on the Mechanical Properties of  
Ti-Al<sub>3</sub>Ti Metal-Intermetallic Laminate (MIL) Composites

by

Richard David Price

Master of Science in Engineering Sciences (Mechanical Engineering)

University of California, San Diego, 2010

Professor Kenneth S. Vecchio, Chair

The mechanical properties of Ti-Al<sub>3</sub>Ti metal-intermetallic laminate (MIL) composites have been investigated with an emphasis on the effect of residual Al at the intermetallic centerline on failure mechanisms in order to ascertain the possible success or failure of using Ti-6Al-4V instead of Ti-3Al-2.5V. MIL composites consisting of alternating layers of Ti, Al, and the intermetallic phase Al<sub>3</sub>Ti were synthesized by reactive foil sintering in open air. Six initially identical stacks of alternating Ti-3Al-2.5V and 1100-Al foils were processed for different lengths of time, yielding specimens with different metal and intermetallic compositions. Samples were cut from each composite plate (in layer orientations parallel and

perpendicular to the intended load direction) for mechanical testing in compression and four point bending, under quasi-static and high strain-rate loading conditions. Examination of the specimens and their fracture surfaces by optical and scanning electron microscopy was performed to establish a correlation between the failure mechanisms present, composite strength, and composition. Results indicated that regardless of loading direction, cracks always initiated in the intermetallic region, and crack propagation and failure were heavily influenced by the thickness of the residual aluminum layers. There is an ideal residual aluminum volume fraction that represents the amount of ductile reinforcement able to most effectively contain the oxides and impurities between intermetallic layers and thereby improve the mechanical properties of the MIL composite.



## Chapter 1

### Introduction

Several plates of a Ti–Al<sub>3</sub>Ti MIL composite have been produced from titanium and aluminum foils by a controlled reaction process in open air incorporating high temperature and pressure. The microstructures of these metal-intermetallic laminate composites can be designed to optimize the desirable characteristics of their constituent components, the end result being a material possessing the high strength and stiffness of the intermetallic phase and the high toughness and ductility of the residual metals. The volume fraction of each component in the laminate is determined both by initial foil thickness and the synthesis process, which allows for fine tailoring of the bulk mechanical properties of the material for specific applications. There are several advantages of this approach to MIL fabrication that make it a viable large scale structural material: one, the use of commercially available foils lowers cost; two, the use of ductile foils allows for the fabrication of non-planar structures [1]. Some of the previous research in the Ti-Al<sub>3</sub>Ti laminate system incorporated Ti-6Al-4V [8, 39, 43, 42, 51 52], which has more desirable mechanical properties than Ti-3Al-2.5V, but possesses an oxide-rich surface finish (a product of the hot-rolling process). Additionally, the composites produced were “fully reacted,” such that no elemental aluminum remained in the microstructure. Results from those studies showed that failure in mechanical testing was heavily influenced by the oxides that accumulated at the intermetallic “centerline” where the aluminum layers had been. The present research uses the less oxide-heavy Grade 9 titanium (Ti-3Al-2.5V) to investigate the possible benefits allowing layers of aluminum to remain in the MIL composite to reinforce the intermetallic centerline.

Tests will be performed to examine how compressive strength and fracture toughness change with respect to the thickness of the residual aluminum layers. In addition to quasi-static compression and bending, high strain-rate tests will be performed to characterize behavior under dynamic loading. Dynamic performance of the composites is important given the applications to the aerospace industry. The primary goal is to establish whether or not a residual aluminum layer increases the performance of the Ti-Al<sub>3</sub>Ti laminate composite in order to ascertain the possible success or failure of using Ti-6Al-4V instead of Ti-3Al-2.5V.

Chapter 2 will provide a background of information regarding the basic concepts behind laminate composites and intermetallics, as well as the physical properties of the metals involved. Other research in the field of MIL composites will be reviewed, with an emphasis on work done on other aspects of the Ti-Al<sub>3</sub>Ti system. A description of the production method will be provided with an overview of the kinetics of reactive foil sintering. General laminate strengthening and ductility properties will be discussed, focusing on the theory of ductile/brittle reinforcement as well as concepts of fracture mechanics and toughening mechanisms. This background will be necessary to evaluate the mechanical behavior of the laminate composites.

A description of the composite synthesis process will be detailed in Chapter 3, including the materials used, foil preparation, the working apparatus, and the control methodology used during fabrication. Post-fabrication characterization with optical and scanning electron microscopy (SEM) will be discussed, as well as sample preparation for mechanical testing. The quasi-static and high strain-rate compression and four point bend testing procedures will be explained, including the basic theory behind the split-Hopkinson Pressure Bar.

Chapter 4 contains the results of work completed, as well as the discussion thereof. SEM micrographs of representative composites produced are shown, and the volume fractions

of each sample are tabulated. The range of residual aluminum content varies across the sample set from 48% to <1%. In quasi-static compression testing where the applied load is perpendicular to the composite layers, the observed trend is a general increase in yield stress with decreasing residual aluminum content, though primarily motivated by increasing intermetallic content. However, when loaded parallel to the composite layers, a decrease in yield stress is seen below a certain Al volume fraction (corresponding to the onset of a failure mechanism). A similar trend is seen in high strain-rate compression tests. Throughout all failed samples, delamination and laminar boundary fracture occurs primarily at Ti-Al<sub>3</sub>Ti interfaces, indicative of a strong bond between Al<sub>3</sub>Ti and residual Al. In quasi-static four point bend testing of crack-divider samples, a decreasing trend exists with no indication of a change in microstructural behavior. The intermetallic phase fails by brittle cleavage, and the Ti and Al layers fail by microvoid coalescence, necking, and tearing. Crack-arrester samples, however, do show a trend indicative of an optimal residual Al content (similar to the compression test results). In the arrester orientation, samples fail by delamination and intermetallic layer cracking, and exhibit several extrinsic laminate strengthening mechanisms. High strain-rate bend tests show very similar results to quasi-static tests, with the exception of the crack-divider orientation: a peak is seen corresponding to the optimal aluminum volume fraction of parallel-oriented samples tested in quasi-static and dynamic compression.

This chapter is currently being prepared for submission for publication of the material. The dissertation author was the primary investigator and author of this material.

## Chapter 2

### Background

#### 2.1 Metal-Intermetallic Laminate Composite Materials

Metal-Intermetallic composites are hybrid laminate structures designed to optimize the desirable mechanical qualities of intermetallics by incorporating layers of ductile reinforcement. The macrostructure of the Ti-Al<sub>3</sub>Ti MIL is composed of bonded layers of titanium, aluminum, and the intermetallic phase titanium tri-aluminide (Al<sub>3</sub>Ti). Al<sub>3</sub>Ti is formed during a sintering process that consumes an amount of Al and Ti related to initial foil thickness and processing parameters. Because brittle intermetallics have strength without toughness, great effort has been made to reinforce them with particles [2-5], fibers [2-4, 6-8], and layers of ductile metals [4, 9-14]. Two of the basic principles behind ductile phase reinforcement are: one, the generation of zones of bridging ligaments by crack-particle (or laminate) interactions that restrict crack propagation by means of closure tractions in the crack wake; two, increasing fracture resistance by employing the work of plastic deformation in the ductile phase.

An intermetallic forms when the bond strength between unlike atoms is stronger than between like atoms, and the crystal structure is determined by the strength and character of the bonding. Binary titanium tri-aluminide possesses a very stable crystalline structure, D0<sub>22</sub>, which has tetragonal symmetry and long-period order. The orbital on the central Al atom is strongly polarized: bonding with second neighbor Al atoms and anti-bonding with second neighbor Ti atoms. Off-center Al atoms, however, are bonded (as opposed to anti-bonded) with the second neighbor Ti atoms. These anisotropic bonds lead to structural stability, but they increase the resistance of atoms on crystallographic planes to displacement under applied stress [15]. The slip process necessary for plastic deformation is inhibited, which makes the bulk material very brittle.

The Young's modulus of polycrystalline  $\text{Al}_3\text{Ti}$  is 216 GPa [16], which is higher than other titanium aluminides. Figure 2.1 [17] shows the effects of increasing temperature on the compressive yield stress and tensile elongation of Ti and several Ti-Al intermetallics. As far as Ti, TiAl and  $\text{Ti}_3\text{Al}$  are concerned, the positive temperature dependence of  $\sigma_y$  is anomalous compared to other metals; the yield strength rises and then falls as the temperature increases. The temperature dependence of  $\text{Al}_3\text{Ti}$  is less marked. At low temperatures, the major deformation mode is ordered twinning in  $(111)[11\bar{2}]$  and slip along the  $[110]$  and  $[100]$  directions. At high temperature,  $(001)[110]$  slip and twinning deformation in  $(111)[11\bar{2}]$  provide a slight increase in ductility. Figure 2.2 [19] shows very sharp ductile/brittle transitions in the temperature dependence of ductility in intermetallic compounds. In comparison to other titanium aluminides, the high aluminum content of  $\text{Al}_3\text{Ti}$  produces several desirable properties: low density ( $3.3 \text{ g/cm}^3$ ), higher oxidation resistance than  $\text{Ti}_3\text{Al}$  and TiAl.

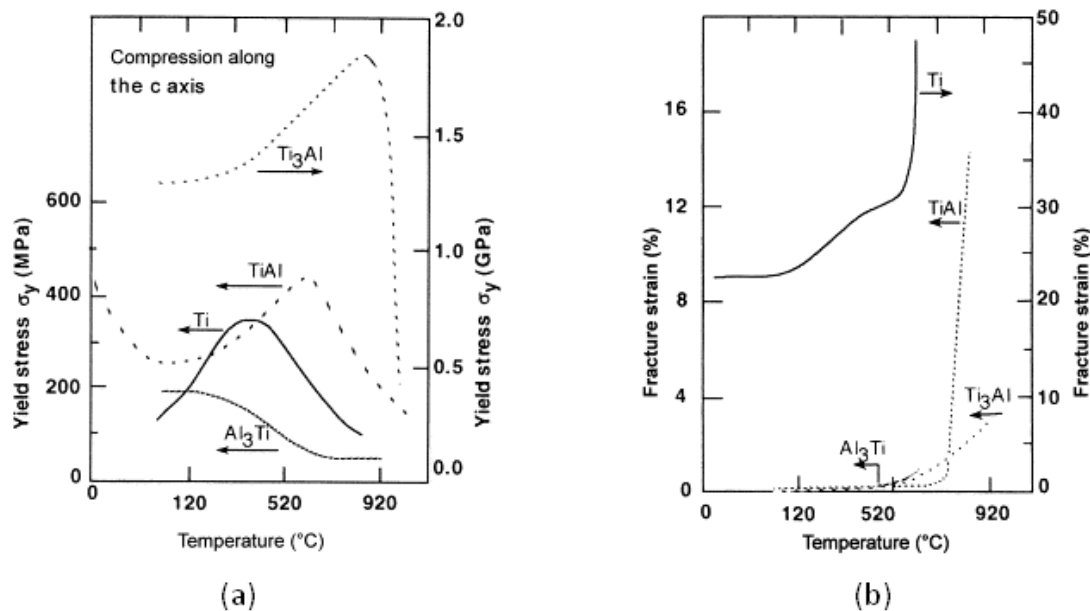


**Figure 2.1 - Temperature dependence of (a) the compressive yield stress and (b) tensile elongation of several Ti-Al compounds [17].**

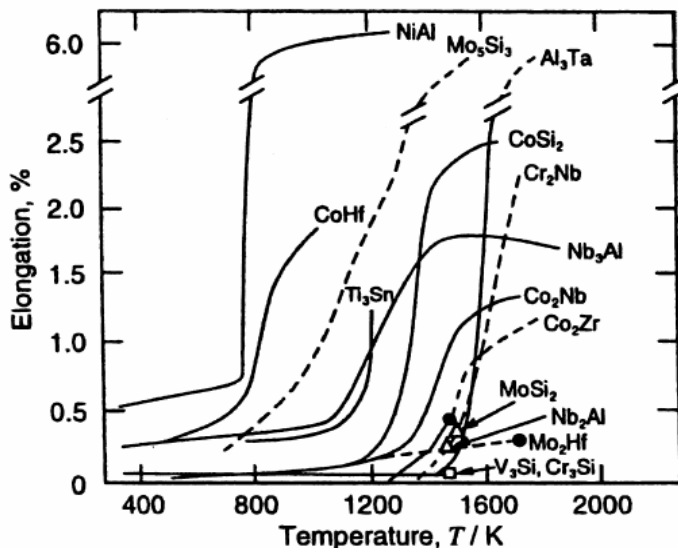


Figure 2.2 - Temperature dependence of ductility of some intermetallic compounds with high melting points [19].

Due to the low free energy of formation and fast diffusivity,  $\text{Al}_3\text{Ti}$  is the first aluminide to form during the reaction between  $\text{Ti}(\text{s})$  and  $\text{Al}(\text{l})$  [20]. As seen in the Ti-Al phase diagram in Figure 2.3 [21], the formation of  $\text{TiAl}_2$  and  $\text{TiAl}_5$  requires a series of solid/liquid or solid/solid reactions with  $\text{TiAl}$ .  $\text{Ti}_3\text{Al}$  and  $\text{TiAl}$  are titanium rich and thus do not form if excess  $\text{Al}(\text{l})$  is present at the start.  $\text{Al}_3\text{Ti}$  is a line compound that melts incongruently at  $1340\text{ }^\circ\text{C}$ .

On the periodic table, titanium is a group IVA transition metal. Structurally, it has an HCP lattice (space group  $\text{P63}/\text{mmc}$ ) that changes into body-centered cubic at  $882\text{ }^\circ\text{C}$ . Titanium has a high tensile strength to density ratio, high corrosion resistance, high fatigue and crack resistance, and good resistance to creep at elevated temperatures. Its modulus of elasticity is  $116\text{ GPa}$ , its molar mass is  $47.9\text{ g/mol}$ , its density is  $4.5\text{ g/cm}^3$ , and it melts at  $1660\text{ }^\circ\text{C}$ . Titanium is as strong as some steels and is 45% lighter. Commercially pure titanium contains up to 0.6% contaminants (oxygen, carbon, iron, nitrogen), which leads to a range of yield strengths from  $275\text{--}689\text{ MPa}$  among grades [22].

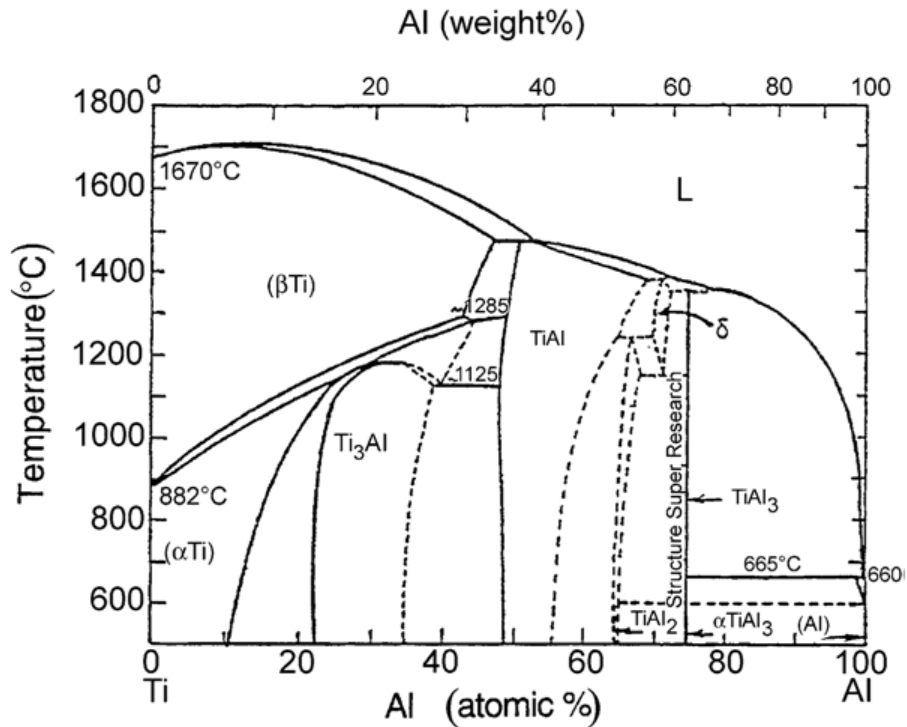


Figure 2.3 - The Ti-Al phase diagram showing the location of Al<sub>3</sub>Ti [21].

Aluminum is in group 13 in the periodic table, and has a face-centered cubic (FCC) crystal lattice at room temperature. Its melting point is 660.4 °C. Aluminum has a Young's modulus of 70 GPa (nearly half that of titanium), and a shear modulus of 26 GPa. The yield strength of pure aluminum is 7–11 MPa, while aluminum alloys have yield strengths ranging from 200 MPa to 600 MPa [23]. Its atomic weight is 27 g/mol and its density is 2.7 g/cm<sup>3</sup> (half that of titanium).

## 2.2 Synthesis of Ti-Al<sub>3</sub>Ti Laminate Composites

### 2.2.1 Review of Synthesis Methods

Researchers at the US Bureau of Mines fabricated Ti-Al<sub>3</sub>Ti laminate composites using a vacuum hot press furnace [24-26]. Their study showed that metal-intermetallic composites can be formed through a self-propagating, high-temperature synthesis reaction (SHS) at the

interface between metal (Fe, Ni, or Ti) and Al foils [24]. The processing technique involved placing a stack of alternating Ti and Al foils between the platens of an induction-heated vacuum hot press. The stacked foils were heated to 900 K and held for an hour with no pressure applied. During this stage the SHS reaction took place, and no pressure was applied to prevent molten aluminum from being squeezed out the sides of the sample. The samples were then heated to 1000 K for 15 minutes, thermally aged, densified under pressure (27.5 MPa and 1100 K) for an hour, then furnace cooled to room temperature. They claimed that an increase in temperature (recorded by embedded thermocouples) before the melting point of Al was evidence of the SHS reaction [26]. The generated heat melts the aluminum, which then reacts with Ti to precipitate a solid intermetallic.

The results of this process can be seen in Figures 2.4 and 2.5 [24]. Beginning with Ti and Al foils of equal thickness (0.15mm), a layered composite was produced (Figure 2.4 [24]) with Ti and  $\text{Al}_3\text{Ti}$  layer thicknesses of 0.044 and 0.111 mm, respectively. They also produced a composite with an initial Ti thickness of 0.25mm and an Al thickness of 0.15mm (not shown). A comparison of the stress-strain curves for these two composites (Figure 2.5 [24]) clearly shows the effect of initial layer thickness on the mechanical properties of the fabricated MIL.



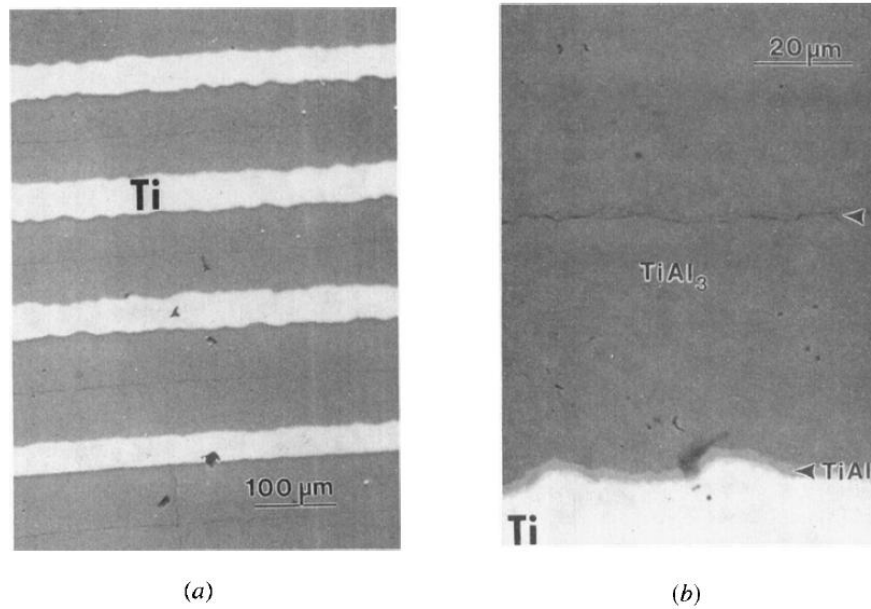


Figure 2.4 – Microstructure of the Ti-Al layered composite produced in vacuum from 0.15 mm thick Ti and Al foils at (a) low magnification and (b) high magnification [24].

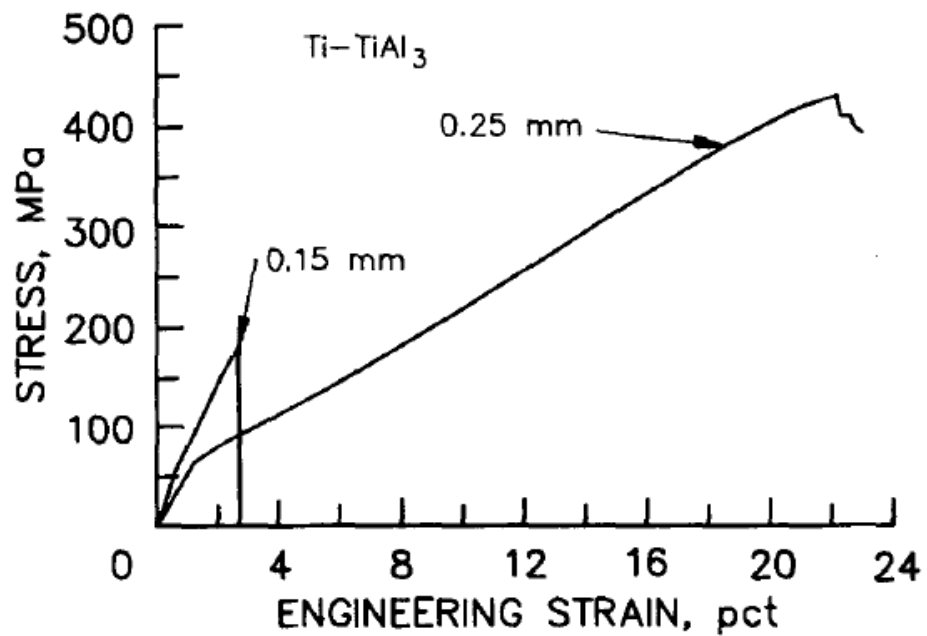
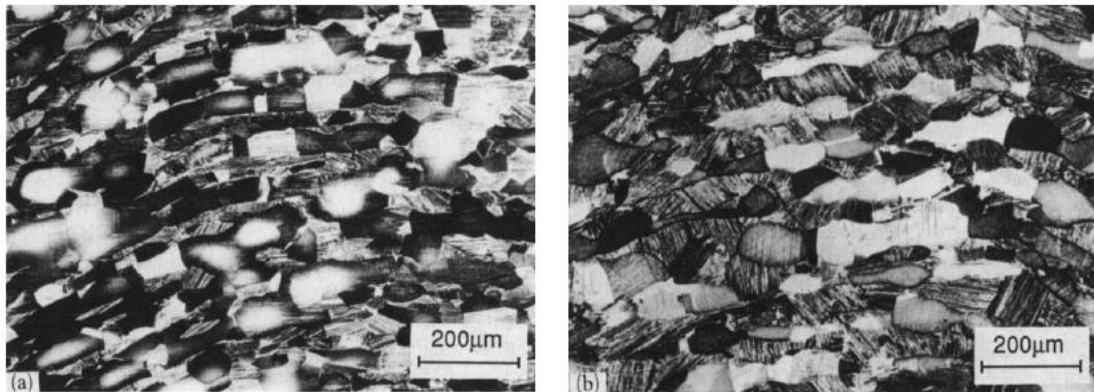


Figure 2.5 – Effect of initial foil thickness on the tensile behavior of a Ti-Al<sub>3</sub>Ti MIL composite fabricated in vacuum via SHS [24].

Other researchers produced Ti-Al intermetallic composites by reactive annealing and hot pressing rolls of pure titanium and aluminum foil [27]. This process, which the researchers deemed reactive foil metallurgy, was based on reactive isostatic pressing (HIP) of a cold-extruded titanium-aluminum elemental powder mixture. A coil of alternating layers of Ti and Al was encapsulated in a titanium can (grade 2 Ti), which was evacuated and welded. The coil was then reaction annealed at 625 °C (below the liquidus temperature of aluminum) for 28 hours, and then isostatically pressed at 1300 °C and 2000 bar for 65 minutes. During the reaction anneal, all the aluminum reacted with part of the titanium to form the intermetallic  $\text{Al}_3\text{Ti}$ . After the annealing, the former coil of elemental foils consisted of alternating layers of  $\text{Al}_3\text{Ti}$ , Ti, and voids. Specimens produced by foil metallurgy had relatively low oxygen contents and a duplex layer structure, as seen in Figure 2.6 [27].



**Figure 2.6 – Optical micrograph of MIL composite microstructure formed by reactive foil metallurgy. HIP reaction at (a) 1300 °C, 65 min and 2000 bar and (b) 1390 °C, 70 min and 2000 bar [27].**

Researchers in Japan fabricated an  $\text{Al}_3\text{Ti}$ -reinforced Ti matrix composite by a combination of combustion synthesis and pulsed-current hot pressing (PCHP) processes [28]. A stack of alternating elemental foils was heated past the melting point of aluminum, and the resulting combustion synthesis reaction at the foil interfaces yielded the formation of porous Ti-aluminides. The pores were eliminated through PCHP, during which a high electric current was applied to the sample, causing spark discharge, evaporation, and melting. The latter two events were highly localized to voids and pores. A composite formed with this process can be produced at low temperatures without being time-intensive. Figure 2.7 [28] shows the results of the combustion synthesis/PCHP process. The three images in the left column show a laminate structure that had initial Ti and Al foil thicknesses of 0.04 and 0.012 mm, respectively. The right three images are of a composite with the same initial Ti thickness and a doubled Al thickness. The authors found that all the aluminum present initially alloyed to form Ti-aluminides during PCHP. Each composite contained layers of several different aluminides, including:  $\text{Al}_2\text{Ti}$ ,  $\text{TiAl}$ ,  $\text{Ti}_3\text{Al}$ ,  $\text{Ti}_3\text{Al}$ . Due to processing conditions, the  $\text{Al}_3\text{Ti}$  layer was composed of many grains and grain boundaries, suggesting weak bonding between grains. In both composites, Al content in the Ti layer decreased with increasing distance from the central part of the layered aluminides. A solid solution of Ti matrix was formed by Al diffusion, caused by the evaporation and melting of the interface between Ti and the aluminides. The presence of this solid solution was not reported in other combustion synthesis methods [24]. Regardless, their results showed that the thickness of the  $\text{Al}_3\text{Ti}$  layer in the final composite could be controlled by the initial Al foil thickness.

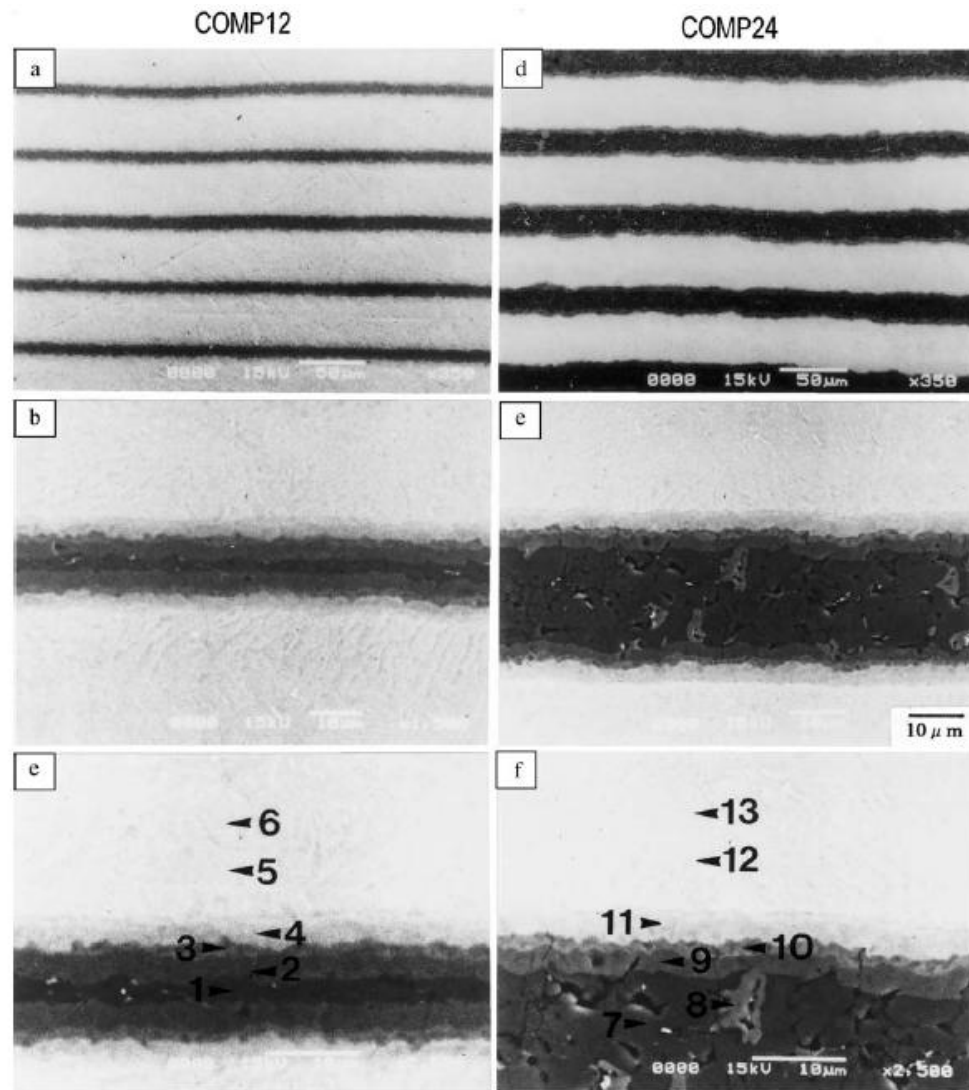


Figure 2.7 - Layered structure of two composites formed from a pulsed-current hot pressing method. The presence of several other aluminide layers can be seen in the magnified images [28].

### 2.2.2 Reactive Foil Sintering

The methods reviewed previously [24-28] all involve reactions that take place in vacuum, and therefore have inherent limitations. Harach and Vecchio [29] established a method to synthesize Ti-Al<sub>3</sub>Ti MIL composites in open air. The ability to perform the fabrication process outside the confines of a vacuum chamber decreases apparatus cost and processing time, while increasing geometric flexibility. These qualities of an open air process make MIL sheet fabrication more viable when considering applications in the aerospace industry.

The present research utilizes this fabrication method—its creators deemed it reactive foil sintering—so the exact procedure will not be explained in this section (see Section 3.1). However, the Ti-Al reaction mechanism and the reaction kinetics have been explored in detail [20, 29-34]. Via a series of interrupted reaction steps, the kinetics of the process were determined to be divisible into two linear regimes, as shown in Figure 2.8 [29]. The first region represents a linear relationship between diffusion-based intermetallic growth and time: diffusion of Al through a thin layer of aluminum oxide (Al<sub>2</sub>O<sub>3</sub>) reacts with Ti to form the intermetallic phase Al<sub>3</sub>Ti. At this stage the oxide layer blocks the diffusion of Ti. Layer growth is linearly dependent on time in the early stages of diffusion when oxide films are present [31]. Aluminum was found to be the only diffusing species.

The second region is a much steeper linear relationship, marking the evolution of the intermetallic layer and the breakdown of the oxide layer. The reaction that forms Al<sub>3</sub>Ti is exothermic, so diffusion eventually increases to the point where the temperature rises past the melting point of Al. The presence of liquid Al then allows reacting Al<sub>3</sub>Ti to migrate away from the Ti layer, signifying the change in aluminide formation from a diffusion-controlled process to a faster, reaction-controlled process (consistent with early research [32]). Some research [32, 34] suggests that the formation of Al<sub>3</sub>Ti proceeds as a continuous aluminide

layer that cracks and fissures under stress. This detaches aluminide particles from the reaction front, exposing unreacted Ti to the molten Al. The studies by Harach and Vecchio support this theory, that as the liquid aluminide phase forms it becomes a sphere, solidifies, and is ejected into the molten Al. Thus, a continuous reaction interface is maintained, which enables a high reaction rate. When the interface moving upward away from one layer meets its reciprocal moving downward from the next layer, the migration ends and the oxides at the front of each interface come together to form the centerline of the intermetallic layer. This centerline can vary in strength depending on the amount of oxide present, which is controlled by several factors: initial foil preparation (oxide removal), processing conditions, foil composition and purity, and foil thickness. Comparing Figure 2.9 [29] to Figure 2.7 [28] illustrates the benefits of the reactive foil sintering process when considering the aim is to create a laminate in which the only aluminide phase present is  $\text{Al}_3\text{Ti}$ .

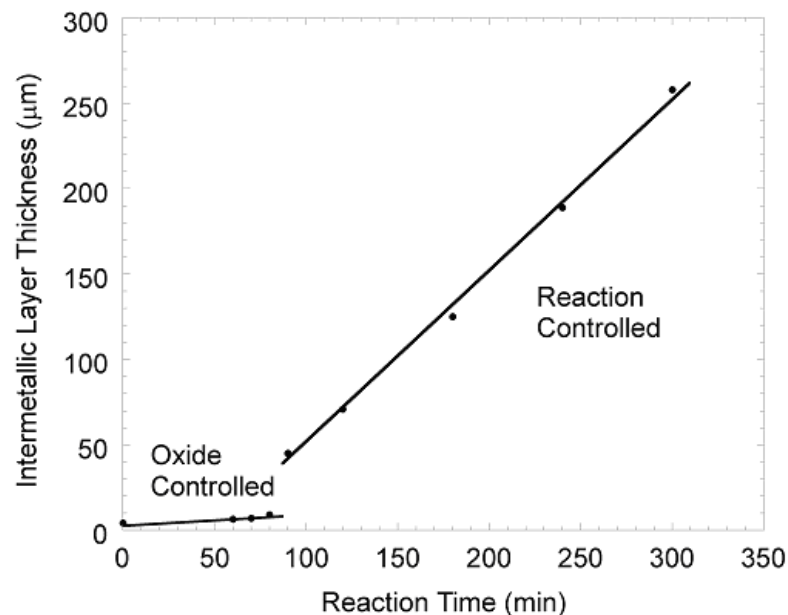


**Figure 2.8 - Intermetallic layer thickness vs. reaction time based on interrupted reaction studies of the reactive foil sintering process [29].**

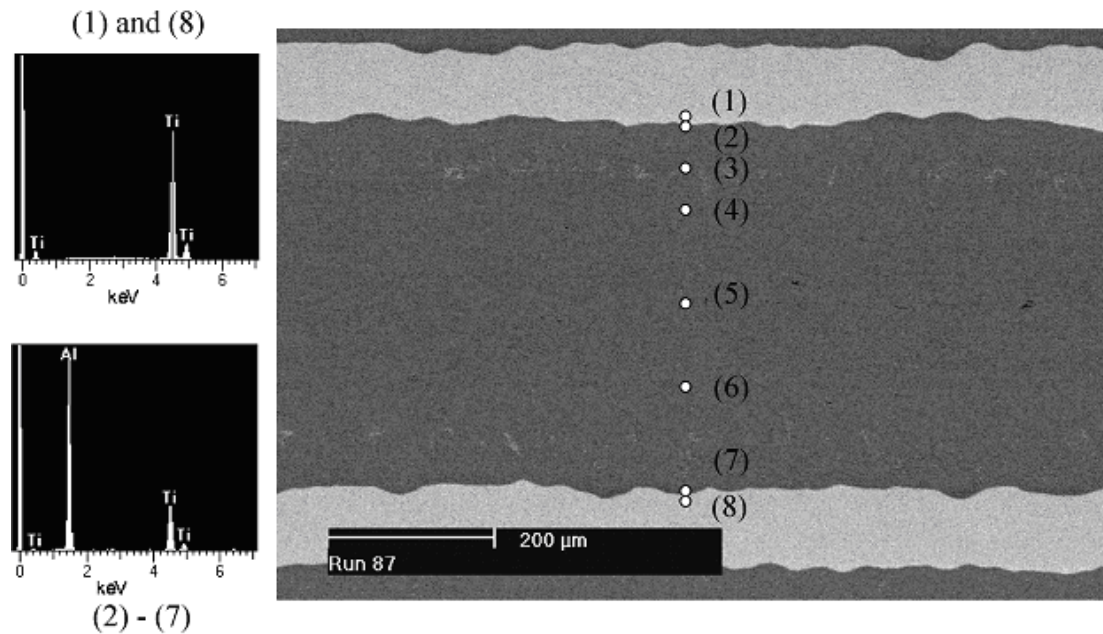


**Figure 2.9 - EDS spectra across an entire intermetallic layer of a sample prepared by reactive foil sintering confirming the intermetallic region is  $\text{Al}_3\text{Ti}$  with no other phases present [29].**

### 2.3 Ductile/Brittle Modeling

#### 2.3.1 Toughening Mechanisms in MIL Composites

In fracture mechanics terms, the extension of a crack is driven by the presence of a "crack-driving force" (generally described by a field-characterizing parameter) and opposed by the resistance of the microstructure [35]. Strain and deformation fields are characterized in terms of the stress intensity factor,  $K_I$ , or the path-independent integral,  $J$ . To restrain the advance of a crack, it is possible to toughen a material by changing its composition or microstructure.

Crack propagation in laminate composites can be studied in two extreme orientations. In compression tests, the layers can be either parallel or perpendicular to the applied force. The same applies to bending tests, but in that case the two orientations are referred to specifically as crack-divider (parallel) and crack-arrester (perpendicular). In the arrester orientation, the crack tip or notch (using a single-edged notched bend beam) terminates in an

individual layer of the sample. During loading the crack front propagates through each layer interface sequentially. In the divider orientation, the crack front intersects all the layers of the sample simultaneously.

In order to fully utilize the strength of inherently brittle compounds, methods have been proposed to increase their crack-growth resistance. Toughening mechanisms fall under two categories: intrinsic and extrinsic [19, 36-40, 43]. Figure 2.10 [38] illustrates the difference between the two classifications. By considering crack growth as a balance between intrinsic damage mechanisms, which promote crack extension ahead of the tip, and extrinsic crack-tip shielding mechanisms, which impede crack growth primarily behind the crack tip, a commonality of behavior between the fatigue of ductile and brittle materials can be found [35].

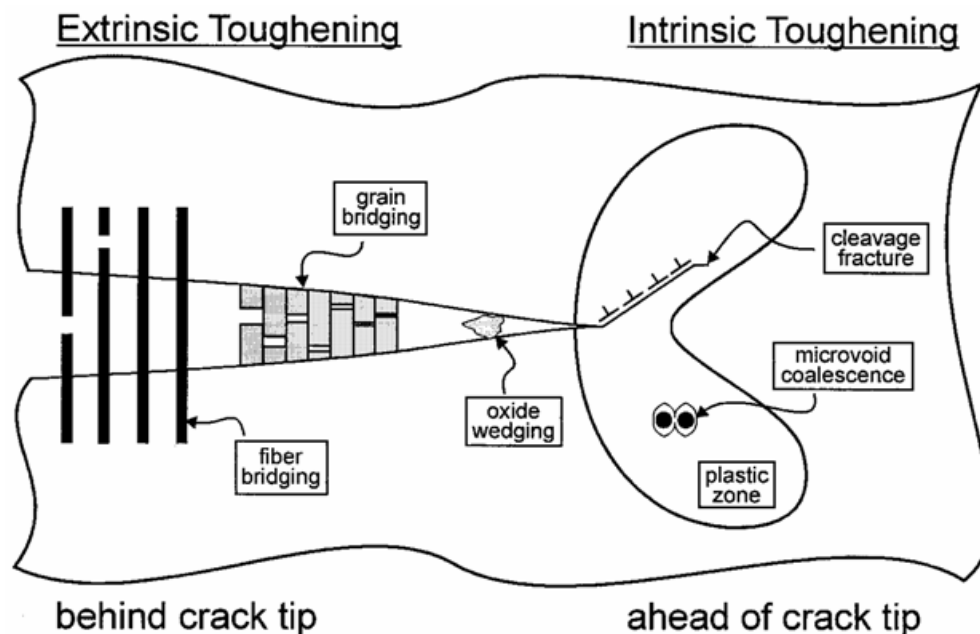


**Figure 2.10 - Diagram of mutual competition between intrinsic mechanisms of damage/crack advance and extrinsic mechanisms of crack-tip shielding involved in crack growth [38].**



Intrinsic toughening is a case where the microstructure exhibits an inherent resistance to crack propagation. This resistance can be attributed to grain size and morphology, particle size and spacing, ductility, bond strength, alloying elements, precipitates, and anything else that can influence dislocation mobility or plastic-zone dimensions [35]. In metals, intrinsic damage mechanisms typically involve processes which create microcracks or voids, e.g., by dislocation pile-ups or interface decohesion in the highly stressed region ahead of the crack tip [38]. This leads to failure by cleavage, intergranular cracking, or microvoid coalescence. Thus, intrinsic toughening is brought about by plastic deformation, where a large plastic-zone size and crack-tip blunting yield high toughness [39]. It is important to note that intrinsic mechanisms are inherent properties of a material, and are independent of crack length and specimen geometry.

Intermetallic compounds permit very little dislocation motion, and so have almost no intrinsic resistance to crack propagation. Failure in a brittle material occurs when the crack driving force reaches or exceeds the fracture resistance ( $K_{IC}$  or  $G_{IC}$ ) of the material. Increasing the toughness of a brittle material by incorporating a ductile phase in the form of particles, fibers, or lamina is one example of an extrinsic mechanism. Most extrinsic toughening mechanisms act behind the crack tip to reduce the local stress intensity (i.e. the local “driving force” for crack growth) by mechanical, microstructural, or environmental means. Extrinsic factors contributing to the brittle nature of intermetallics include interstitial impurities, notches, and other surface defects [19]. The distinct layers present in MIL’s toughen brittle materials by way of various extrinsic mechanisms—shown schematically in Figure 2.11 [36]—resulting from the creation of plastic zones surrounding the crack or from physical contact between the crack surfaces via wedging, bridging, sliding or combinations thereof.

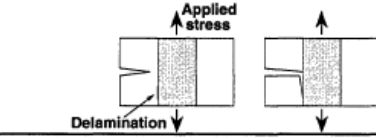
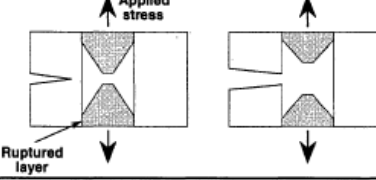
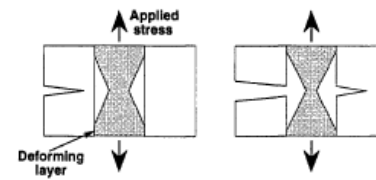
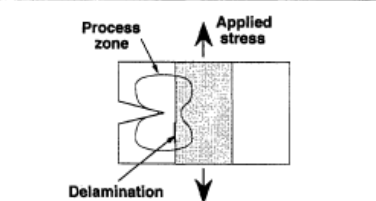
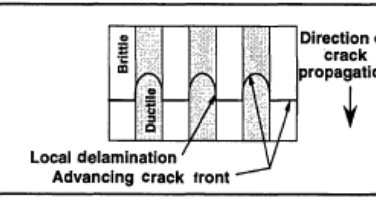
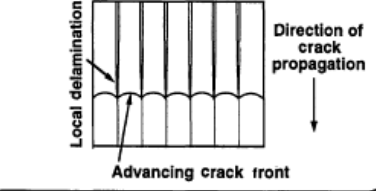
Mechanism (Testing orientation)	Volume fraction dependence	R-curve behaviour possible	
<b>Crack deflection</b> (Crack arrester)	No	...	
<b>Crack blunting</b> (Crack arrester)	No	...	
<b>Crack bridging</b> (Crack arrester)	Yes	Yes	
<b>Stress redistribution</b> (Crack arrester, crack divider)	...	Yes	
<b>Crack front convolution</b> (Crack divider)	Yes	Yes	
<b>Local plane stress deformation</b> (Crack divider)	...	Yes	

Figure 2.11 - Extrinsic toughening mechanisms for laminated metal composites [36].

Six major extrinsic toughening mechanisms exist that are dependent on orientation [36]. One is crack deflection, which can be seen in crack-arrester samples. This mechanism occurs when layers delaminate ahead of an advancing crack, or when a crack reaches an interface. Crack deflections (up to 90°) can reduce the local stress intensity by leading the

crack away from the planes of maximum stress. Crack deflection is independent of the volume fraction of the metallic phase.

Crack Blunting (crack arrester orientation) occurs when a crack encounters a ruptured region and is deflected and blunted. A significant amount of energy is required for a crack to re-nucleate, which equates to an increase in toughness. Crack blunting is independent of the volume fraction of the metallic phase.

Crack Bridging (crack arrester and divider orientations) occurs when unbroken ductile layers span the wake of a crack so that further crack growth requires stretching of the bridging ligaments. Crack bridging increases toughness of a laminate material as a function of the ductility of the bridging ligaments, and can result in resistance curve (R-curve) behavior. Crack bridging depends on the volume fraction of the ductile metallic phase. Figure 2.12 [39] shows crack bridging in two orientations.

Stress Redistribution (crack arrester and divider orientations) occurs when delamination ahead of the crack-tip serves to reduce and redistribute the local stress. This mechanism can be more effective than slip in stress reduction and can result in R-curve behavior.

Crack Front Convolution (crack divider orientation) occurs in layered composites composed of materials with dissimilar ductilities. When the crack front propagates from a layer of low ductility to a layer of higher ductility, it becomes highly convoluted and can result in interfacial delamination. Overall crack front growth is retarded by the plastic tearing required for crack growth in the more ductile layer. This mechanism can result in R-curve behavior, and is dependent on the volume fraction of the ductile metallic phase.

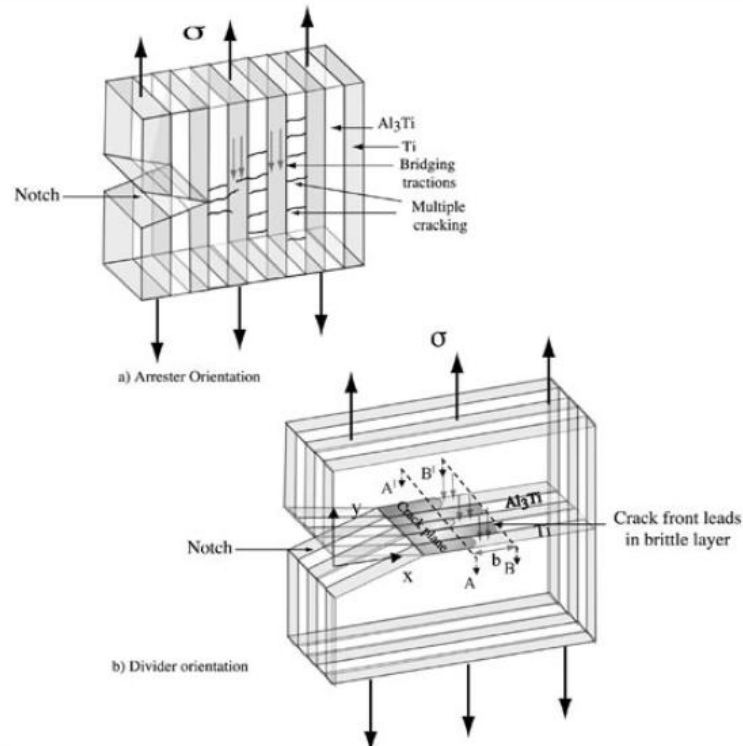


**Figure 2.12 - Schematic diagram illustrating crack bridging: (a) crack-arrestor orientation and (b) crack-divider orientation. Planes AA and BB indicate cross sections of the laminate composite near the crack tip. The arrows between the planes indicate bridging tractions over the length of  $b$  [39].**

An additional extrinsic toughening mechanism specific to laminate composites has been discussed [40, 41]. Results by Lugovy *et al.* [40] studying the apparent fracture toughness,  $K_{app}$ , of  $\text{Si}_3\text{N}_4$ -based laminates showed that a mismatch of coefficients of thermal expansion (CTE) between layers generates thermal residual stresses. They found that  $K_{app}$  increases in layers with a residual compressive stress while decreasing in layers with a residual tensile stress, as illustrated in Figure 2.13 [40]. Since the coefficients of thermal expansion of the constituent phases are usually quite dissimilar, cooling from the high processing temperatures to room temperature almost always generates high enough thermal stresses for onset of local viscoplastic deformation [41]. Additional inelastic deformation may

be generated by the application of mechanical pressure during fabrication. High residual stresses are therefore present in the as-fabricated state. Because compression serves as a crack shielding mechanism resulting in toughening of the laminate composite, CTE mismatch can be an effective way of providing improved flaw tolerance and surface damage resistance. However, the reverse is also true: a large difference in elastic moduli or thermal expansion coefficients can lead to plastic yielding, microcracking, interface decohesion and creep under uniform temperature change [42].

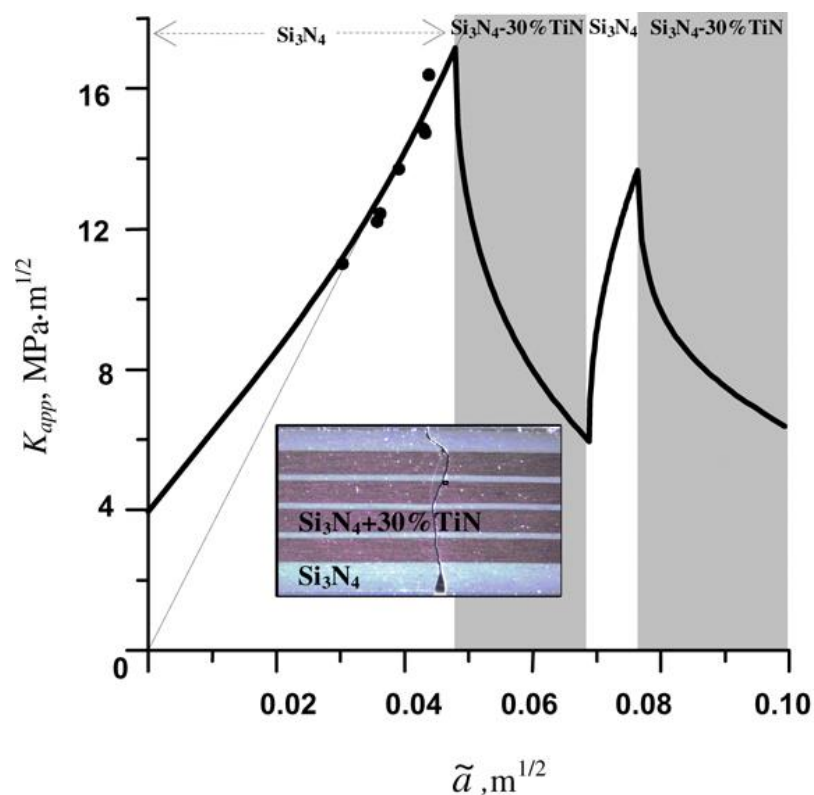
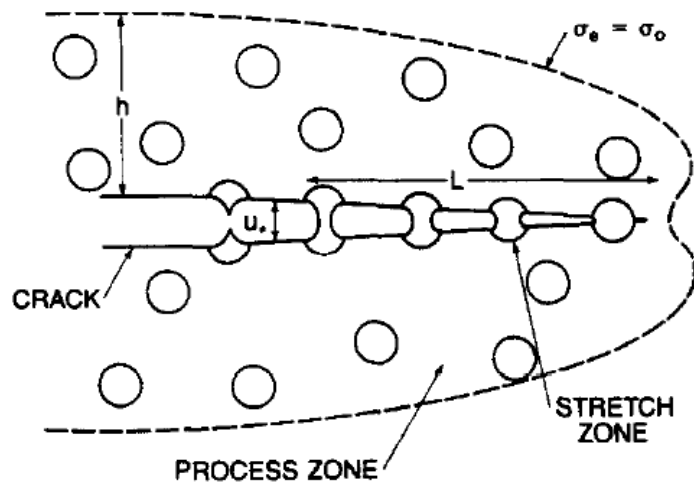


Figure 2.13 - The apparent fracture toughness as a function of the crack length parameter  $\tilde{a}$  in a laminate with an outer layer under residual compressive stress [40].



**Figure 2.14 - Crack bridging process caused by intercepted ductile particles and a process zone of plastically distorted ductile particles [37].**

### 2.3.2 Ductile/Brittle Reinforcement

The concept of ductile-phase toughening of brittle material uses the work of plastic stretching of a ductile component embedded in a brittle matrix to increase energy dissipation, thus leading to increased toughness [43]. These components can either be ductile particles, as shown in Figure 2.14 [37], or ductile layers, as in the case of the present research. In the case of ductile particles, the necking of dispersoids or precipitates during crack bridging requires a work-of-stretching that increases the overall toughness (also applies to fiber reinforcements). The function  $\sigma(u)$  relates the stress/crack opening,  $u$ , to the uniaxial plastic flow properties of the ductile material. It can be related to the enhanced toughness,  $\Delta G_C$ , by Equation 2.1, in which  $f$  is the area fraction of ductile material intercepted by the crack and  $u^*$  is the total crack opening when the ductile material fails [37]:

$$(2.1)$$

If one considers the intrinsic crack-initiation toughness of a ductile-brittle composite to be  $K_0$ , then the toughness of the composite is increased by an amount,  $\Delta K_C$ , during ductile phase crack bridging. Under small-scale bridging conditions (SSB), the bridging tractions act over a distance that is small relative to the crack length and in-plane specimen dimensions. The steady-state toughness,  $K_{SS}$ , can then be represented by Equation 2.2) [44]:

$$\text{_____} . \quad (2.2)$$

Equations 2.3a and 2.3b relate fracture toughness,  $K$ , and strain energy release rate,  $G$ , under conditions of plane stress and plane strain, respectively:

$$\text{---} , \quad (2.3a)$$

$$\text{---} . \quad (2.3b)$$

The increase in critical fracture energy due to ductile reinforcements,  $\Delta G_C$ , can be formulated in terms of the physical properties of the reinforcement and interface by relating it to a nondimensional work of rupture,  $\chi$  [45]:

$$\text{_____} . \quad (2.4)$$

Here,  $\sigma(u)$  is the stress-displacement function of the bridging tractions,  $u^*$  is the displacement at failure of the bridging ligament, and  $\sigma_0$  and  $r$  are the flow stress and characteristic dimension of the reinforcement, respectively. Then, using Equation 2.1, the steady-state magnitude of the change in critical strain energy release rate becomes:

$$, \quad (2.5)$$

where  $f$  is the volume fraction of reinforcement intercepted by the crack (as in Eq. 2.1).

Equation 2.2 then becomes:

$$\text{_____} . \quad (2.6)$$

### 2.3.3 Resistance Curve Behavior

The source of R-curve toughness in ductile-brittle laminates is primarily associated with the crack-tip shielding that results from ductile phase layer bridging in the wake of a crack. The traction distribution, crack length, and specimen geometry all affect the reduction in the near-tip stress intensity,  $K_b$ . Generalized solutions employ a weight function,  $h(a,x)$ , to calculate the stress intensity for any form of the traction function,  $\sigma(x)$ , a distance  $x$  behind the crack tip with bridging length  $L$ :

$$(2.7)$$

If the shielding contribution is superposed with the intrinsic toughness of the composite, the measured toughness,  $K_{c,app}$ , for a given loading condition can be predicted:

$$(2.8)$$

where  $K_o$ , as previously discussed, is the intrinsic (crack-initiation) toughness of the composite. To simplify Equation 2.7, it can be assumed that the traction  $\sigma(x)$  is a constant function that is: one, uniform over the bridging zone; two, equal to a characteristic flow parameter,  $\sigma_c$ . This parameter can be taken as the uniaxial yield or flow stress of the metal, the volume fraction of which is accounted for in the simplified form:

$$(2.9)$$



### 2.3.4 Laminate Failure

By their nature, laminate composites consist of several constituent materials—each with different properties—joined along many interfaces. The inherent mismatch in mechanical properties contributes to several types of local fracture events that nucleate at many sites distributed throughout a laminate due to their inability to form a major crack [41]. Thus, interfaces play a crucial role in the failure (and strengthening) of laminate composites; they may impede or promote damage development. The presence of material interfaces can constrain the extension of matrix cracks through crack bridging, but if exposed to high shear stresses separation can occur. This leads to the opening of interfacial cracks between the matrix and the reinforcing layers, as well as delamination between plies. Composite laminates are highly susceptible to delamination damage, due mainly to their lack of transverse reinforcement and interface weakness [46]. Interface debonding relaxes the stress concentration and spreads deformation during loading, which delays catastrophic failure.

There are two types of cracks during delamination under bending: breakthrough and interfacial [47]. When the driving force of a crack front surpasses the resistance force of the matrix, a breakthrough crack is generated, which propagates instantly for the length of one layer's thickness. In the simple case of a rectangular plate with a crack perpendicular to the applied load, by Griffith's theory the driving force is:

$$\frac{dG}{da} = \sigma^2 a, \quad (2.10)$$

where  $G$  is the strain energy release rate,  $\sigma$  is the applied stress,  $a$  is half the crack length, and  $E$  is the Young's modulus. If  $\sigma = \sigma_f$ , the critical bending strength of the layers, then  $G$  becomes  $G_c$ , the critical strain energy release rate. If  $G > G_c$  the crack will propagate.

The second type is an interfacial crack, which occurs only at an interface. When a breakthrough crack extends, the loading is high enough for the generation and rapid

propagation of an interfacial crack. During propagation, loading decreases as elastic energy is absorbed. As roller displacement increases, the driving force increases while staying in dynamic equilibrium with the resistance force. The interfacial crack grows until the load increases to the point where breakthrough cracks renucleate in the next layer. The extent of debonding is influenced by factors such as frictional sliding and the presence bridging ligaments along the de-bonded surface [44].

One study [48] tested single-edge notched bend samples of a bilayer Al-SiC laminate in four point bending (4PB). The research, which agreed with the findings of Shin and Guo [47], identified two specific types of interface responses: one, delamination after crack extension to the interface; two, interfacial delamination prior to crack extension. In a laminate with a strong interface, a propagating crack will ignore the interface, i.e. no delamination. The first mode is most common in laminates with intermediate interfacial strength, with both delamination and crack extension occurring almost simultaneously. Here, the peak load of the moment-displacement curve represents the load right before the extension of the primary crack. The second mode takes place primarily where interfaces are weak. In this case, the peak load corresponds to the load before delamination of the interface. As seen in Figure 2.15 [48], the delamination point in both cases is taken as the trough immediately following the peak. The load at the peak prior to the delamination moment represents the amount of force needed to drive the crack along the interface further, which depends on interfacial strength. In Figure 2.15b [48], the second peak represents the extension of the crack following delamination.

Rawers and Perry [49] performed tensile tests on metal-intermetallic composites to study their failure mechanisms, specifically crack initiation and propagation. Their results showed that cracking always initiated in the intermetallic layers, and then propagated according to the thickness and elasticity of the adjacent layers. If an intermetallic crack met a metal layer that allowed shear deformation, shear bands propagated from the crack tip through the metal and into the next intermetallic layer, creating stress concentration points at the metal-intermetallic interfaces. If an intermetallic crack met a metal layer that did not permit shear deformation, stress buildup led to crack distribution in the intermetallic layers. These observations support the concepts of ductile layer reinforcement of a brittle matrix.

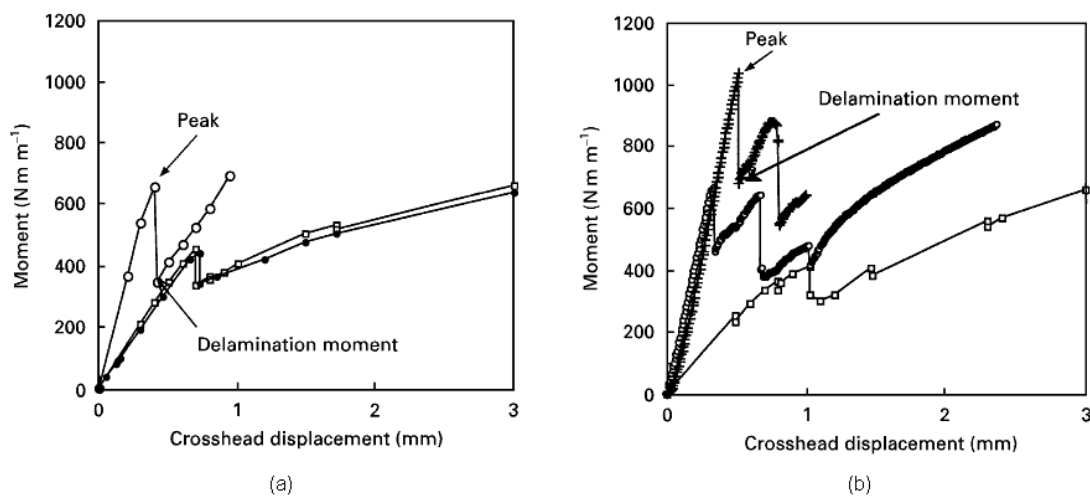


**Figure 2.15 – Moment-Displacement curves showing delamination (a) after and (b) before crack extension [48].**

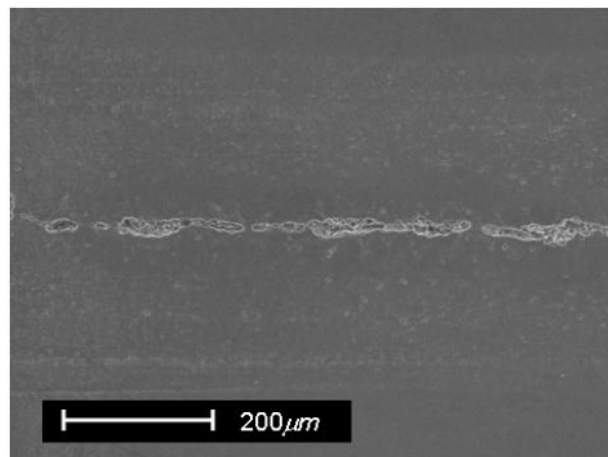
#### 2.4 Previous Research in Ti-Al<sub>3</sub>Ti MIL Composites

The focus of previous research in Ti-Al<sub>3</sub>Ti MIL composites [29, 30, 39, 42, 43, 50-52], has been on the mechanical properties of a laminate system in which all the original aluminum in the composites reacted to form Al<sub>3</sub>Ti, i.e. no residual aluminum layer exists in the synthesized laminate microstructure. In compression [30, 50, 51], tension [30, 50], bending/R-curve [30, 39, 43, 50], and ballistic [30] tests, one common trait observed was the failure mechanism of the composite microstructure. In all cases, failure initiated in the intermetallic layers (in agreement with findings by Rawers and Perry [49]), and in most cases samples failed by fracture at the intermetallic centerline. As previously discussed (see Section 2.2.2), the intermetallic centerline is a product of the synthesis method. When the reaction interface moving away from one Ti layer meets its reciprocal moving from the next layer, the oxides at each front come together to form the intermetallic centerline. In the aforementioned studies, the presence of oxides at the centerline was responsible in part for the weakness of the microstructure, and efforts to control the level of contamination were limited to pre-fabrication steps like foil cleaning. Manual cleaning of the foils produced positive results for Ti-3Al-2.5V and commercially pure Ti (Figure 2.16b [51]), which can be cold-rolled without much surface oxidization. However, higher strength grades of titanium like Ti-6Al-4V require hot-rolling and pickling, which results in a strongly adherent oxide layer that is difficult to remove.

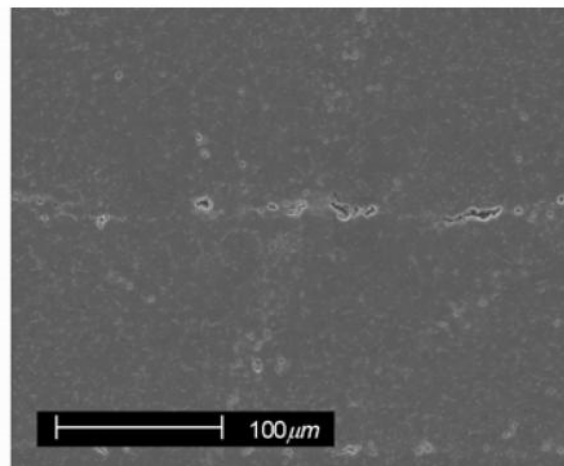
Because the type of Ti used has little effect on the reaction kinetics of Ti and Al [30], it can be assumed that the primary cause for differences in mechanical behavior among MIL composites is due to the Ti grade chosen. That said, it makes the most sense to create a Ti-Al MIL with the strongest titanium possible. However, it has been shown by SEM observation [51] that the Ti grade used to construct the composite does have a large effect on the quantity, size, and distribution of oxides in the intermetallic centerline. As seen in Figure 2.16 [51], the

centerline of an MIL specimen containing Ti-6Al-4V has more microvoids and  $\text{Al}_2\text{O}_3$  than a specimen produced similarly with commercially pure Ti. Currently, attempts are being made to circumvent this Achilles' heel of the MIL composite by allowing a reinforcing layer of Al to remain at the intermetallic centerline.

This chapter is currently being prepared for submission for publication of the material. The dissertation author was the primary investigator and author of this material.



(a)



(b)

**Figure 2.16 – SEM micrographs showing the aluminum oxides ( $\text{Al}_2\text{O}_3$ ) and microvoids in MIL composites constructed with (a) Ti-6Al-4V and (b) commercially pure Ti. [51]**

## Chapter 3

### Experimental Procedure

#### 3.1 Materials and Processing

##### 3.1.1 Materials Used

The foil materials used in the present research are Ti-3Al-2.5V and 1100 Al. Table 3.1 shows the chemical compositions of both metals, along with selected mechanical properties. In other studies where the laminate synthesis process remained constant for each specimen produced, combinations of foils of different thicknesses were used to tailor the final titanium content of the MIL composites, and to ensure that all the initial Al was consumed to form  $\text{Al}_3\text{Ti}$  [1, 29, 30, 39, 43, 50]. Because the goal of the present work is to study the effects of residual aluminum in the composite, foils of equal thicknesses were used. The initial Ti and Al foils were both 0.005” (0.127mm) thick.

**Table 3.1 - Chemical compositions and properties of components**

Material	Composition (%)	Density (g/cc)	Tensile Str (MPa)	Yield Str (MPa)	Elastic Mod (GPa)
Titanium Ti-3Al-2.5V	Ti: 94.4, Al: 2.95, V: 2.52 Fe: 0.05, O: 0.065, C,N,Y <0.01	4.48	750	560	91
Aluminum 1100	Al: 99, Cu: 0.05-0.2, Zn: 0.1, Si, Fe: 0.95, Mn and others: 0.05	2.71	110	105	70-80

### 3.1.2 Sample Preparation

Foil squares were cut from rolls of sheet Ti-3Al-2.5V and Al-1100: Ti samples were 4"x4", and Al samples were roughly 4"x4" (Al roll width was insufficient to cut exactly 4"x4" sheets without material waste). All foils were sanded with an abrasive (Scotchbrite) to remove oxide layers and surface contaminants. Following the abrasive, each foil was scrubbed with acetone to remove any residual contamination, and then again with methanol. They were stacked in alternating layers: 34 sheets of titanium with 33 sheets of aluminum (with titanium being the first and last sheet). With this stacking, the final MIL composite would contain 66 layers of Al<sub>3</sub>Ti, given that the intermetallic forms at every Ti-Al interface. Barring the differences at the edges due to the smaller size of the Al sheets, each stack had the same general dimensions: 4"x4" and roughly 3/8" tall (before processing). Once cleaned and assembled, the stacks were placed individually in the composite synthesis apparatus.

### 3.1.3 Synthesis Apparatus

Figure 3.1 shows a schematic diagram of the apparatus used to synthesize metal-intermetallic laminate composites in open air. One foil stack was placed in an Instron screw-driven load frame crosshead between two Ni-alloy (Haynes 230) platens measuring 17.8 x 17.8 cm. Each of the platens contained six heating elements that could be independently controlled, as well as a thermocouple that measured the temperature at the center of the platen. The external load and the temperature of each heating element were controlled by software written in LabVIEW. The entire platen-crosshead setup was covered with ceramic wool insulation and water-cooled.

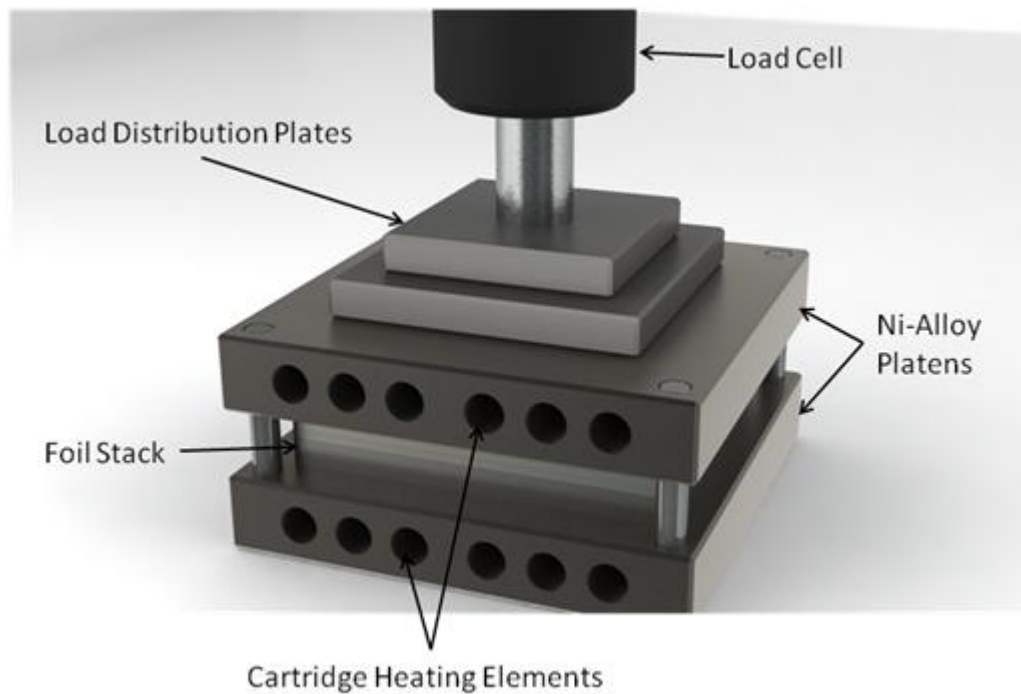


**Figure 3.1 – Rendering of the synthesis apparatus (not to scale).**

#### 3.1.4 Processing Method

The method utilized to synthesize MIL composites was the reactive foil sintering process described previously [29, 30]. Once the stack was in place in the load frame, a load of 10000 lbs was applied to ensure good contact between the foils. Because the surface area of the samples was variable through their thickness, the pressure applied was approximate. Without considering any variations in surface area, the pressure applied was roughly 625 psi (4.3 MPa). The temperature was set initially to 700°C for the first 12 minutes (this was done simply to increase the heating rate and shorten the ramp up period), then the sample was kept at 645°C for a length of time that depended on the desired total processing time. Table 3.2 details the temperature history of each specimen fabricated with this method. Following the heating cycle, each MIL plate was air-cooled to room temperature. The applied load remained constant throughout the entire process.



**Table 3.2 - Temperature profile for each sample (in °C)**

Time hours (min)	Specimen					
	MIL-48	MIL-42	MIL-16	MIL-11	MIL-3	MIL-1
0	700	700	700	700	700	700
0.2 (12)	645	645	645	645	645	645
0.25 (15)	645	647	645	645	645	645
0.3667 (22)	647	647	645	645	645	645
0.5 (30)		648	645	645	645	645
1 (60)			647	645	645	645
1.5 (90)			648	645	645	645
2 (120)				647	645	645
2.5 (150)					647	647
3 (180)					648	648
3.5 (210)						650

### 3.2 Characterization and Microscopy

Prior to mechanical testing, a sample from each of the plates produced was observed under a scanning electron microscope (SEM) with secondary and backscattering electron imaging modes. Samples were ground to 4000 grit and diamond polished to 0.05µm beforehand. Pictures were taken of the microstructure of each composite in order to determine the volume fraction of each component. Layer thickness measurements were made at several different places in each specimen, averaged, and inserted into the equation:

$$f_a = \frac{t_a n_a}{t_a n_a + t_b n_b + t_c n_c}, \quad (3.1)$$

where  $t$  is the layer thickness and  $n$  is the number of layers of a component in the specimen. Scanning electron microscopy was performed on a Philips XL 20 SEM capable of energy-dispersive X-ray spectroscopy (EDS) (Oxford Instruments). EDS spectra were quantified using a Link/ISIS multi-channel analyzer. An Olympus GX51 optical microscope and Image-Pro Plus analysis software were used in conjunction with SEM images to more thoroughly

characterize sample fracture surfaces. Hand-held photographs were taken using an Olympus Stylus 1010 digital camera.

### 3.3 Mechanical Testing

#### 3.3.1 Quasi-Static Compression Testing

Rectangular compression samples were cut from each MIL composite plate using a Struers Accutom 5 high-speed cut-off wheel. Dimensions ranged from 5 to 8 mm on each side. Three of these samples were made for each of two loading orientations for all six specimens (total of 36 samples). Prior to mechanical testing, one sample from each of the twelve groups was ground and polished to  $0.05\mu\text{m}$  for post-testing SEM imaging.

Compression tests were performed at room temperature in an Instron 8501 servo-hydraulic load frame, pictured in Figure 3.2. The strain rate was  $0.001 /\text{s}$  for both the parallel and perpendicular orientations. A self-aligning head was used to account for imperfections in sample geometry. Displacement data from the deflectometer and load data from the load cell were recorded and used to plot load-displacement and stress-strain curves. Of the three samples tested for each case (parallel and perpendicular orientations), one was allowed to proceed to failure, while the other two were stopped at different points in the plastic deformation region to analyze damage evolution (though many of the more brittle samples failed without being stopped). The 0.2% slope offset rule was used to determine the yield stress of samples for each condition, and for those samples that showed no plasticity before failure, the ultimate stress was taken as the yield stress. After testing, one failed sample from each group was cold-mounted, ground and polished (to final polish), and imaged to analyze sub-surface failure characteristics.

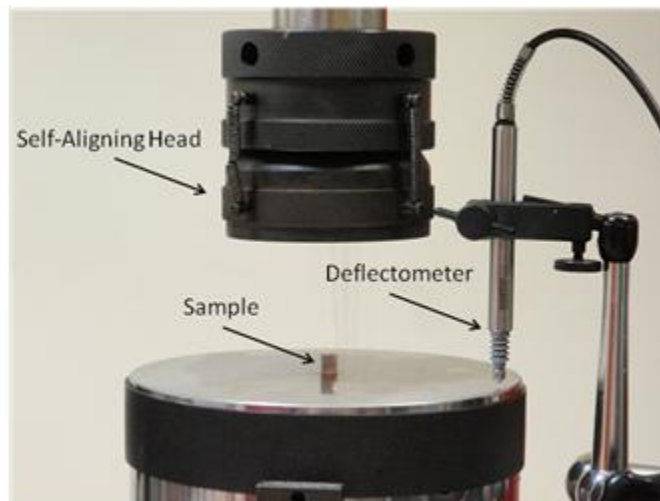


**Figure 3.2 – Apparatus used in quasi-static compression testing.**

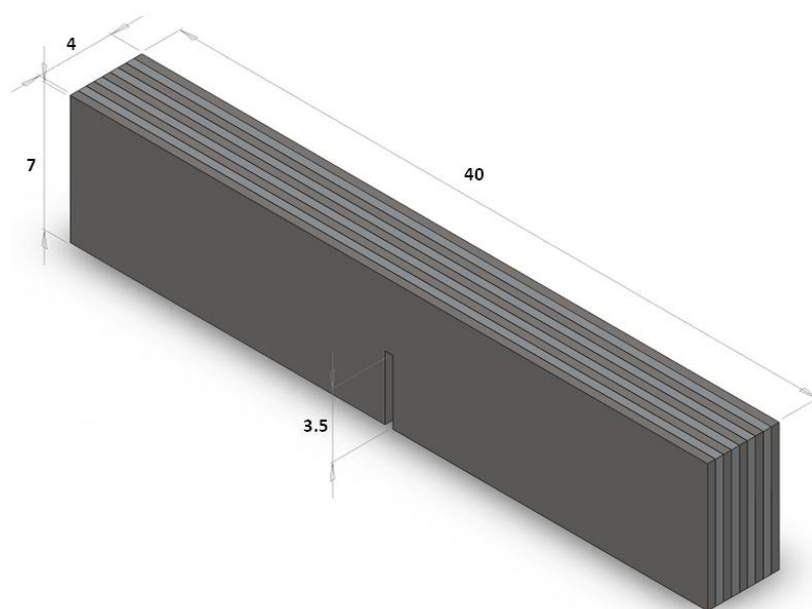


**Figure 3.3 – Schematic diagram of the typical dimensions of samples used in 4PB tests. Dimensions in millimeters.**

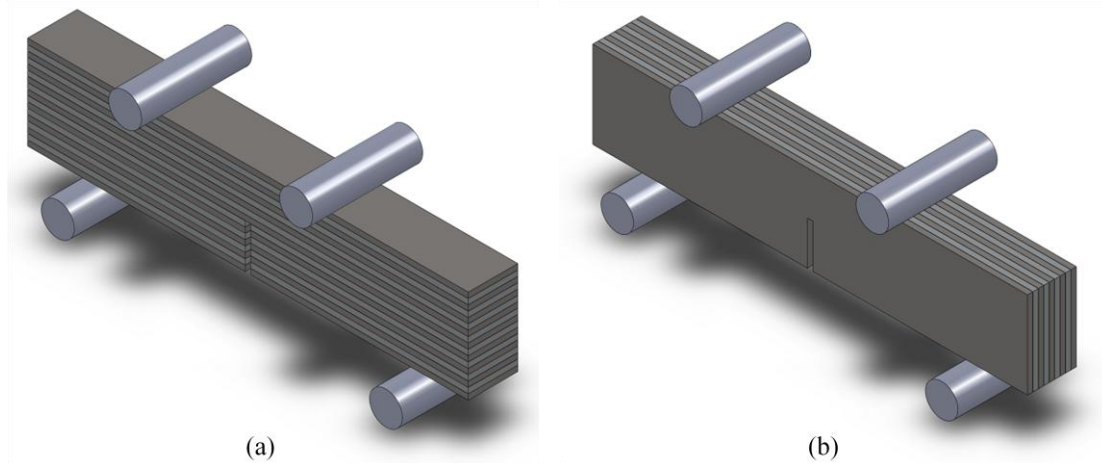


**Figure 3.4 –Schematic diagrams of SE(B) in (a) crack-arrester and (b) crack-divider orientations**

### 3.3.2 Quasi-Static Four Point Bend Testing

Single edge notched bend (SE(B)) beams were prepared for four-point bend (4PB) testing to determine the fracture toughness of the MIL composites. The dimensions of the samples varied on a small scale, but each was cut in accordance with ASTM standard E-399-90 [53], shown in Figure 3.3. The average length, width, and height were 40, 4, and 7 mm, respectively. Average notch depth was 3.5 mm, such that  $0.45 < a/W < 0.52$  (“a” being the notch depth, and “W” the sample height). Ten bend beams were cut in each loading orientation (Figure 3.4) for each MIL specimen (total of 120 samples, 60 of which were used for quasi-static tests). Two samples from each specimen in the perpendicular orientation were ground and polished prior to mechanical testing. Tests were carried out under displacement control at a rate of 0.5mm/min.

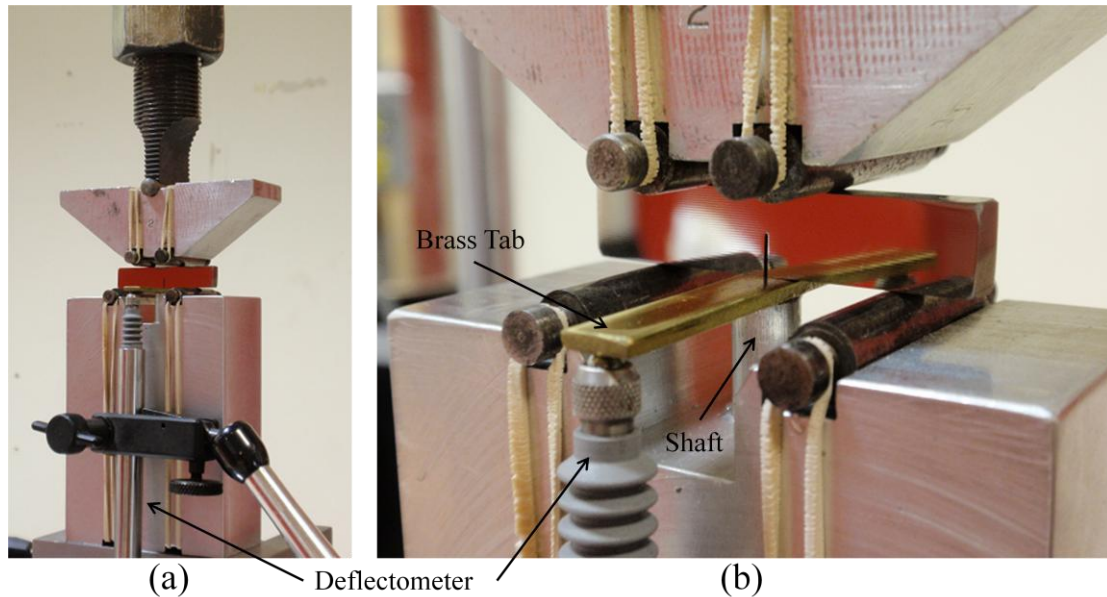


**Figure 3.5 – Novel apparatus designed to test small samples in quasi-static 4PB: (a) overall setup in the load frame; (b) close-up of the bending area. As the crack opens, the sample pushes down on the shaft and tab, which is recorded by the deflectometer.**

To avoid scaling effects [30], the bend bars used for quasi-static and high strain-rate (dynamic) testing were made the same size. Because the size of the bend bar was limited by the size of the dynamic testing apparatus, alterations had to be made to the quasi-static setup to accommodate a small sample. A novel apparatus was fabricated to test samples of this size, as shown in Figure 3.5a. Due to size and positioning constraints, a double-cantilever clip-in crack opening displacement (COD) gauge could not be placed under the sample. A bottom support was designed with a hole under the sample notch, into which a spring and shaft were inserted (Figure 3.5b). The spring was necessary to keep the brass tab (the top end of the shaft) in constant contact with the sample. As the crack opened it pushed down the tab, which in turn depressed a deflectometer (shown). The hole and shaft were lubricated with grease to eliminate noise. Pin span dimensions were 13mm and 26mm.

Fracture toughness values,  $K_{IC}$ , were calculated for four-point bend loading using:

$$\text{---} \quad \text{---} \quad (3.2)$$

where  $L$  is half of the difference of the external and internal spans ( $L = 0.0065$  in these tests),  $P$  is the load,  $B$  is the specimen thickness,  $W$  is the specimen height,  $a$  is the notch length, and  $f(a/W)$  is the function:

$$f(a/W) = \frac{3W^2 - 4a^2}{6W^2} \quad (3.3)$$

To determine an accurate value of fracture toughness, the critical load,  $P$ , corresponding to the fracture onset point must be accurately detected by the apparatus. In three-point bend (3PB) fracture tests, crack initiation is determined using the 5% slope offset of the load-COD curve in accordance with ASTM E399 procedures. ASTM C1421 procedures for ceramics [53] are commonly used to measure the fracture toughness of brittle materials, in which case calculating the toughness requires the peak load be determined from load response as a function of time. Rather than calculating crack length with a compliance technique, a unique COD (described above) was used to detect crack initiation in terms of the ASTM E399 method.

The load  $P$  was taken from the load-strain curve of each sample. In the crack divider orientation, the 5% slope offset method was used to find the critical load as per ASTM E399. In the arrester orientation, the peak load immediately preceding the first delamination moment was used, as discussed previously [48]. The crack lengths,  $a$ , of bend samples with layers oriented perpendicularly to the applied load were measured by SEM prior to mechanical testing. Crack-divider samples were broken apart by hand after testing to image the fracture surface end-on (Figure 3.6a, b). For accuracy, five measurements were taken of the depth of the notch—three of which are shown in Figure 3.6c—and averaged for every crack-divider sample. A scanning electron microscope was used for these measurements. All sample dimension, crack depth, and load data was input into a Microsoft Excel spreadsheet to calculate  $K_{IC}$  for each sample. Curves were then plotted of  $K_{IC}$  versus residual aluminum content for each loading orientation.

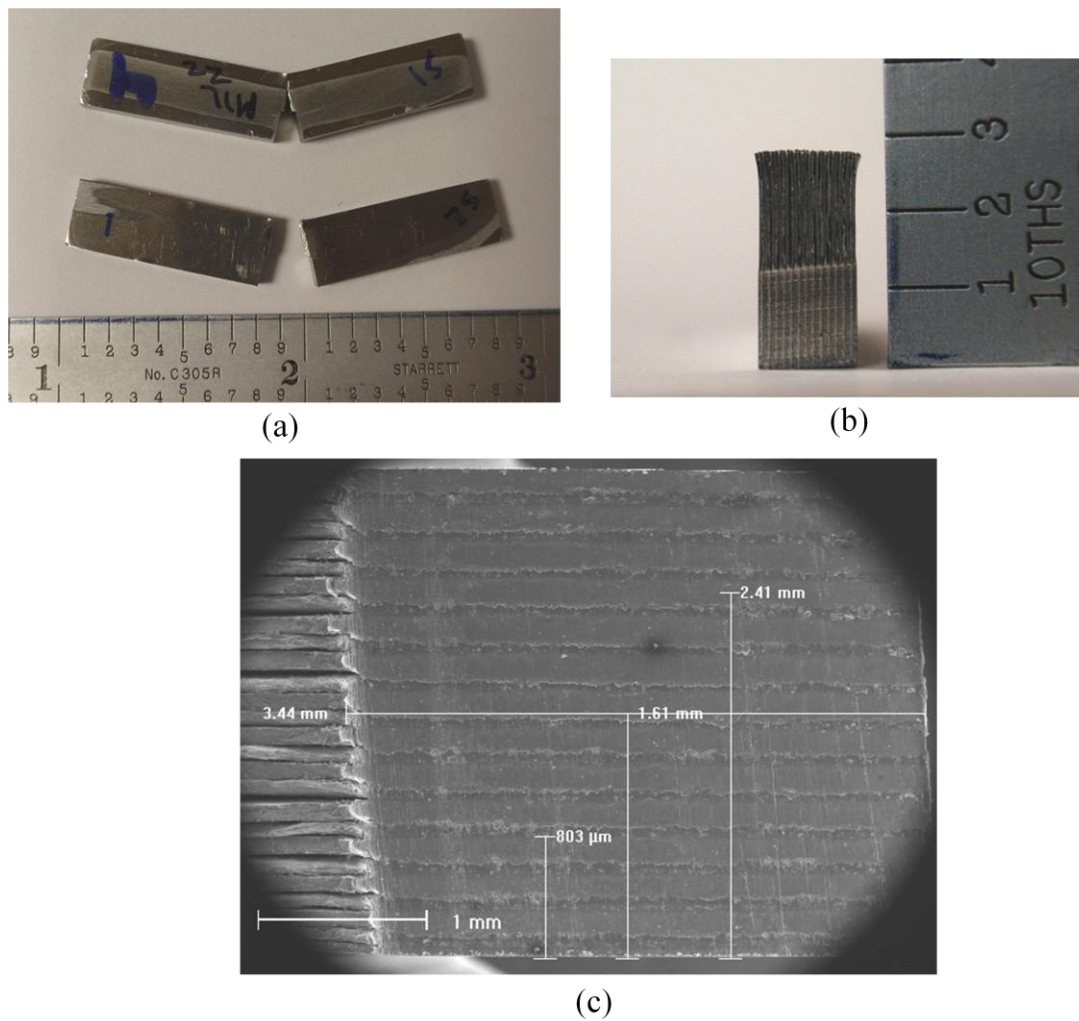


**Figure 3.6 – Photographs of (a) broken and unbroken crack-divider samples and (b) the end-on view of the fracture surface. (c) SEM image of the notch depth measurement of a crack-divider sample.**

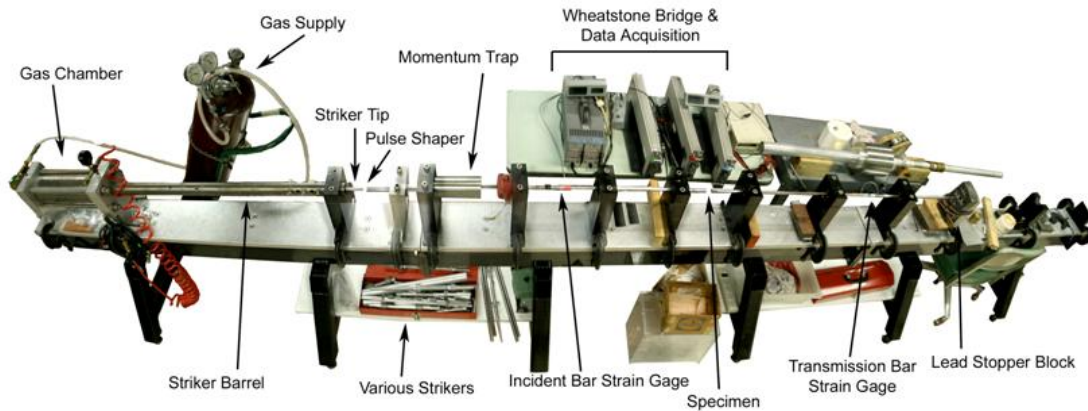


**Figure 3.7 – Split-Hopkinson Pressure Bar with pulse shaper and momentum trap used for high strain-rate compression and bend testing [55].**

### 3.3.3 High Strain-Rate Compression Testing

The samples prepared for high strain-rate (dynamic) compression were generally smaller than those used for quasi-static testing, with rough dimensions: 4x4x4 mm ( $\pm 1$  mm in every dimension). Four samples were tested in both orientations (layers perpendicular and layers parallel to the applied load) for all six MIL specimens, unless more were needed for data analysis purposes. Dynamic compression tests were performed on a modified split-Hopkinson Pressure Bar (SHPB) (Kolsky, 1949) to achieve strain rates of  $\sim 1000$  /s. A two-bar split-Hopkinson apparatus was chosen because existing ASTM techniques, such as Idoz and Charpy impacts tests, are on the whole poorly instrumented, whereas SHPB is well-instrumented and experimentally validated [55-60].

On the extreme left of Figure 3.7 [55], which is a panoramic photograph of the experimental setup, is the gas gun that propels the striker bar into the “incident bar.” The resulting compressive stress pulse travels through the incident bar to the sample, at which point part of the incident wave ( $\epsilon_I$ ) is transmitted through the sample into the “transmission bar” as the stress wave  $\epsilon_T$ , and a portion of the wave is reflected back ( $\epsilon_R$ ) toward the striker and the momentum trap. The pulse is measured by two strain gauges—one on the incident bar



and one on the transmission bar—as a function of time, which is used to calculate stress and strain. Data acquisition was performed at  $10^7$  Hz.

One-dimensional stress wave theory was used to calculate stress  $\sigma(t)$ , strain  $\varepsilon(t)$ , and strain-rate  $\dot{\varepsilon}(t)$ :

$$\sigma(t) = E \varepsilon(t) + E \varepsilon_R(t) \frac{L}{C_0}, \quad (3.4)$$

where  $\varepsilon_R(t)$  is the strain of the reflected tensile wave in the incident bar directly proportional to the strain rate [30]. Additionally,  $C_0$  is the speed of sound in the bars,  $L$  is the length of the sample, and  $E$  is the elastic modulus of the bar. The strain is found by integrating 3.4. Stress in the sample is calculated with the equation:

$$\sigma(t) = E \frac{A_0}{A} \varepsilon_T(t), \quad (3.5)$$

where  $A_0$  and  $A$  are the cross-sectional areas of the bar and the sample, respectively, and  $\varepsilon_T(t)$  is the compressive strain of the in the transmission bar.

A 12 inch striker bar with a 0.5 inch diameter was used, and strain-rates up to 1500/s were achieved. The SHPB incorporated a pulse shaper [56, 57] to achieve nearly constant strain rates and to obtain a reliable stress-strain response in the MIL composites. Aluminum was used as the pulse shaper material.

### 3.3.4 High Strain-Rate Four Point Bend Testing

High strain-rate 4PB tests were performed on a modified split-Hopkinson Pressure Bar. The samples used for this testing were of the same dimensions as those used in quasi-static testing. Figure 3.8 [59] is a diagram of the four point bending setup used in SHPB testing (same loading pin geometry as quasi-static tests). Figure 3.8a shows that the incident bar used was hollow, which was done to improve the quality of the strain gage signal. Several

procedures were used in dynamic 4PB testing. Where appropriate, tests were recorded using a Phantom V12 digital high-speed camera (Vision Research Inc., USA).

For the crack divider orientation, samples were polished (4000 grit) and dynamically loaded in 4PB. A high speed camera (shown in Figure 3.8b) was triggered by a photo gate positioned in the path of the striker bar, and recorded the entire deformation process. Using the recording (which was low resolution but high frame-rate ~400,000 fps), the elapsed time from the trigger to crack initiation was determined by visual inspection, which was then used in conjunction with loading data from the SHPB to determine the true elapsed time from deformation onset to crack initiation. The trigger signal from the striker bar was sent to the camera and the Hopkinson bar data acquisition system. With the Hopkinson bar LabVIEW control program, the time from the trigger to the beginning of the incident pulse (recorded at the center of the incident bar) was determined and added to the time it took for the strain wave to travel half the length of the incident bar. That sum was subtracted from the crack onset time taken from the camera relative to the trigger, and the difference was taken as the final crack onset time relative to deformation onset (not the trigger). With the crack-onset time the critical load was found from the load-time curve, and  $K_{IC}$  values were then calculated with the same Excel spreadsheet that was used in quasi-static 4PB testing (Section 3.3.2). This method [55, 58, 59] was used because the 5% offset rule (ASTM E399) only applies in low strain-rate regimes. This method was verified using strain gages.

Determining the critical load of perpendicularly-oriented 4PB samples did not require a high speed camera. The method for determination of  $K_{IC}$  was the same as in quasi-static 4PB; the critical load was assumed to be the peak load immediately preceding the first delamination moment taken from the load-time curve (from the SHPB). The viability of this method was determined by fitting several samples with a crack propagation (CP) gage (Hottinger Baldwin Messtechnik, Model 1-RDS-22) just to the side of the notch as shown in

Figure 3.9a. The CP gage contains 50 resistive wires ( $44 \Omega$ ) connected in parallel, and changes in voltage due to wire breaking were detected by a  $\frac{1}{4}$  bridge circuit (shown schematically in Figure 3.9b [39]). The elapsed time from deformation onset to the first voltage change in the gage signal was shown to correlate to the first peak of the load-time curve. The critical load was then used to find  $K_{IC}$  using Equations 3.2 and 3.3. To monitor the deformation process, two samples from each specimen were ground and polished (to final polish) and recorded by the high-speed camera at high resolution and reduced frame rate ( $\sim 54000$  fps).

This chapter is currently being prepared for submission for publication of the material.

The dissertation author was the primary investigator and author of this material.

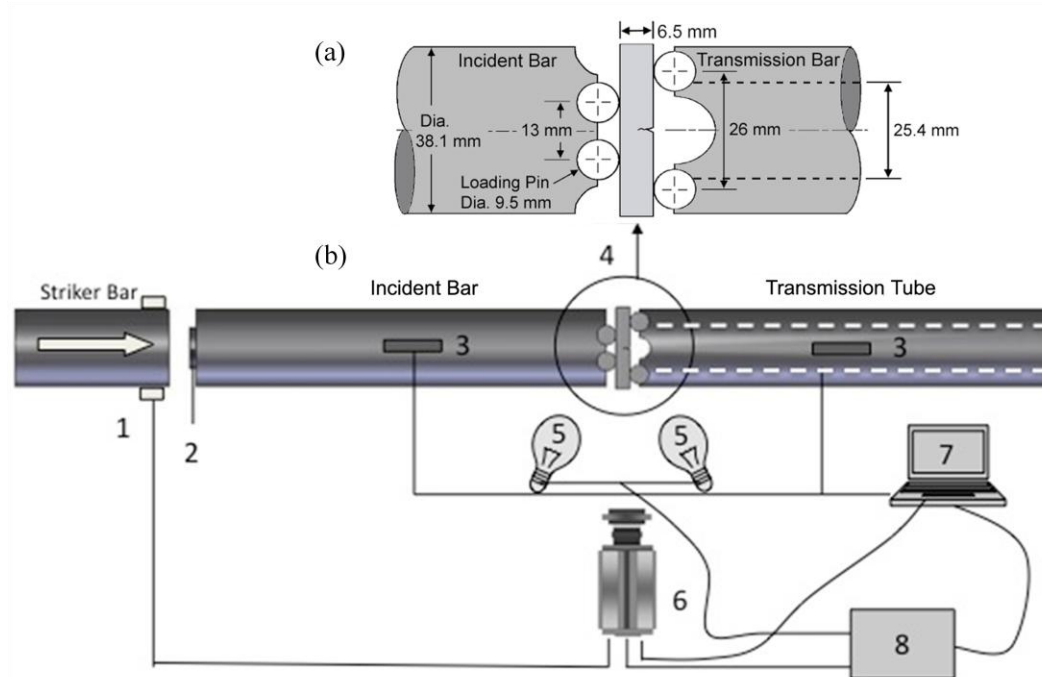
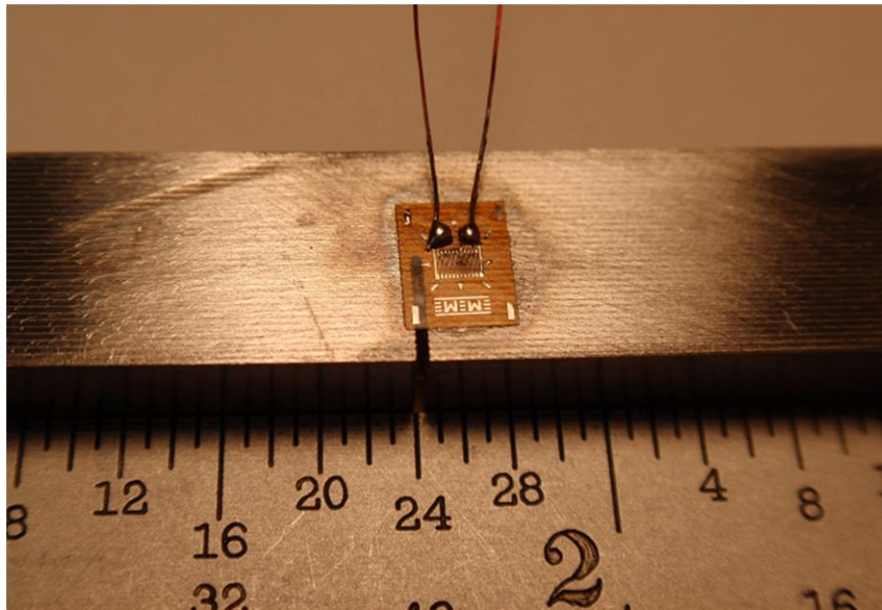
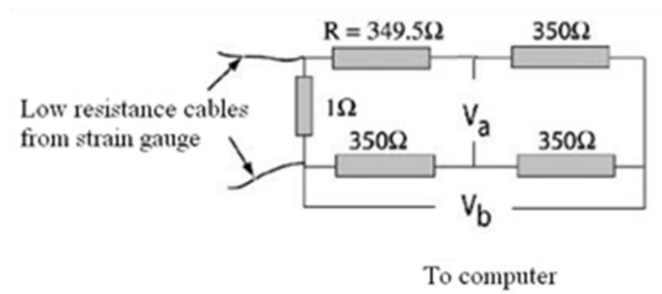


**Figure 3.8 – (a) Schematic of the sample mounting setup. (b) SHPB setup for dynamic fracture toughness experiments: (1) photo gate trigger, (2) pulse shaper, (3) strain gage, (4) SE(B) specimen, (5) lighting for (6) high speed camera, (7) data acquisition, (8) power supply [59].**



(a)



(b)

Figure 3.9 – (a) Photograph showing strain gage placement. (b) Schematic of the strain-gage amplifier [39].

## Chapter 4

### Results and Discussion

#### 4.1 MIL Composite Physical Properties

##### 4.1.1 Composites Produced

By carefully controlling the fabrication process, metal-intermetallic laminate composites with varying residual aluminum volume fractions have been prepared for mechanical testing. Table 4.1 shows the processing times, final layer thicknesses, and volume fractions of each specimen prepared, as well as the designations used. Specimens are referred to by their residual aluminum content (in volume percent). Figures 4.1a and 4.1b are graphical representations of the data presented in Table 4.1. Figure 4.1a indicates that as reaction time increases, the Al layer thickness decreases to the single-digit micron range, and Figure 4.1b shows that the intermetallic phase quickly takes over as the dominating constituent in the composite. Even though the intermetallic layer thickness is less than that of titanium in MIL-1, the volume fraction is twice as large because there are twice as many  $\text{Al}_3\text{Ti}$  layers as Ti layers.

**Table 4.1 – Specimens produced: designation and microstructure.**

Designation	Processing Time hours (min)	Layer Thickness ( $\mu\text{m}$ )			Volume Fraction		
		Ti	Al	$\text{Al}_3\text{Ti}$	Ti	Al	$\text{Al}_3\text{Ti}$
MIL-48	0.367 (22)	122.2	120.2	1.986	0.503	0.481	0.016
MIL-42	0.5 (30)	116.6	102.8	11.12	0.490	0.419	0.091
MIL-16	1.5 (90)	97.58	38.46	53.26	0.409	0.157	0.434
MIL-11	2 (120)	84.8	25.6	61.2	0.371	0.109	0.520
MIL-3	3 (180)	78.4	6.4	73.42	0.345	0.027	0.627
MIL-1	3.5 (210)	83.22	2.1	76.12	0.357	0.009	0.634

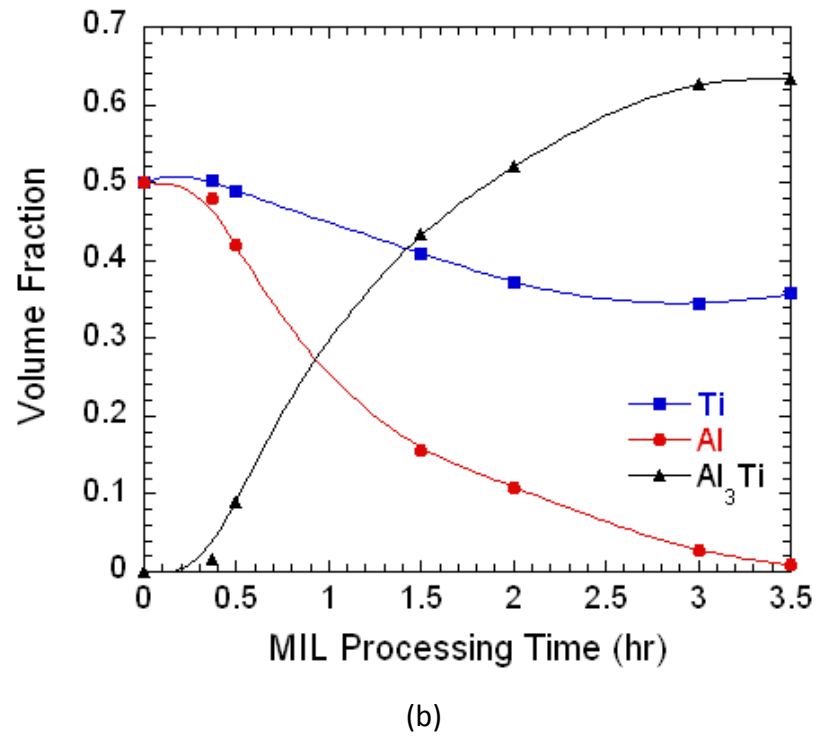
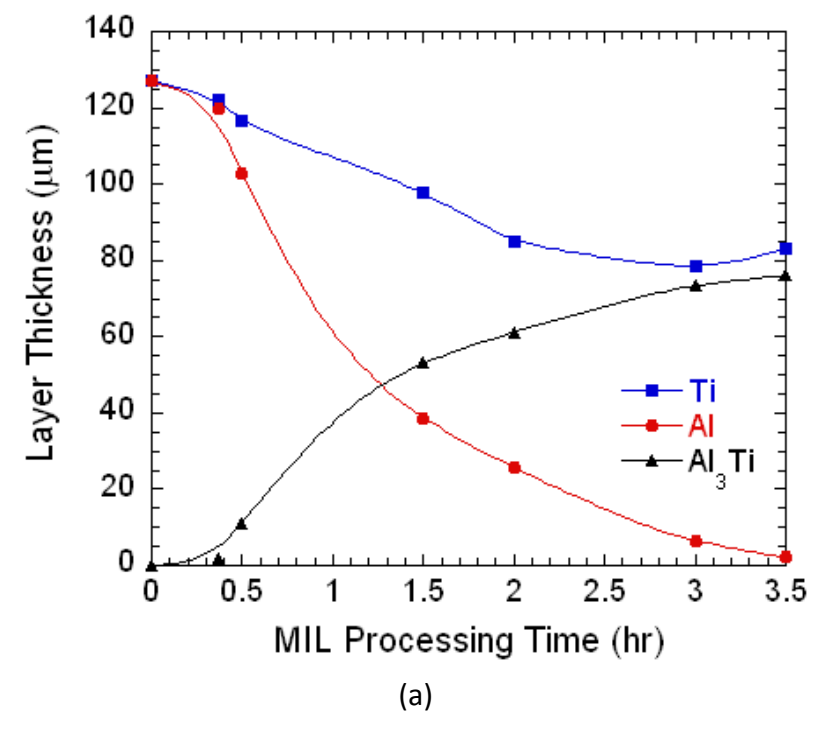


Figure 4.1 – The effect of processing time on (a) layer thickness and (b) volume fraction.

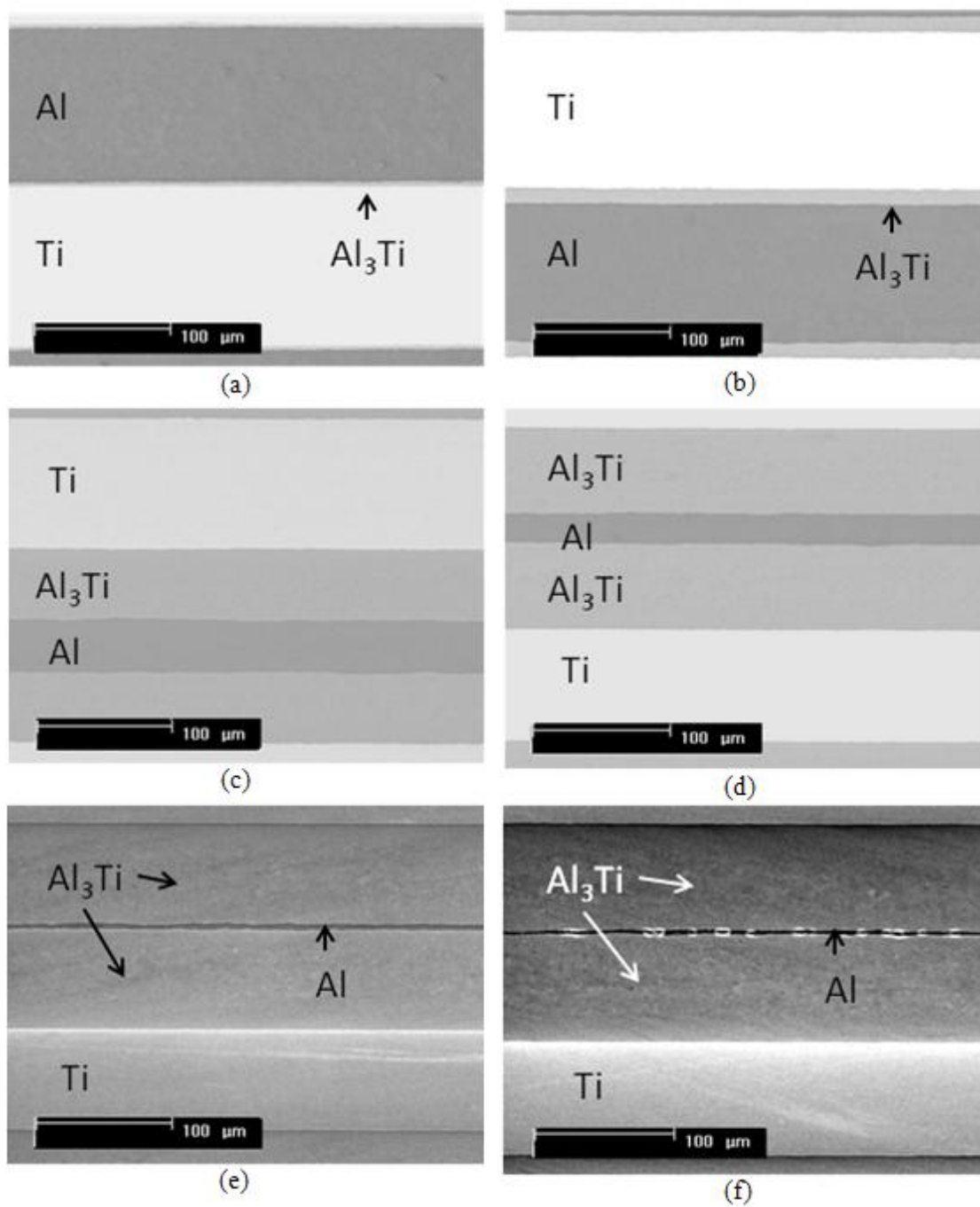


Figure 4.2 – MIL composite specimens produced via reactive foil sintering. SEM micrographs taken of specimens (a) MIL-48, (b) MIL-42, (c) MIL-16, (d) MIL-11, (e) MIL-3, and (f) MIL-1.

Representative SEM micrographs of each specimen produced can be seen in Figure 4.2. Figure 4.2a shows the thin layer of  $\text{Al}_3\text{Ti}$  forming at the Ti-Al interfaces after 22 minutes of reaction time, which becomes more visible in MIL-42 (Figure 4.2b). Figures 4.2c and 4.2d show the significantly larger  $\text{Al}_3\text{Ti}$  regions of MIL-16 and MIL-11, followed by the reduction of the Al layer to the hairline sliver seen in MIL-3 and MIL-1 specimens (Figures 4.2e and 4.2f, respectively). Comparing their microstructures to micrographs of composites produced by other methods, one sees the benefits of the process used in the present research. The MIL composites shown in Figure 4.2 have much sharper layer boundaries than those created by the SHS reaction in vacuum (see Figure 2.4). Also, these specimens do not show the stratification of other [unwanted] intermetallic phases as found in samples produced by pulsed-current hot pressing (see Figure 2.7). The micrographs in Figure 4.2 closely resemble the composites produced by Harach and Vecchio (see Figure 2.9), confirming the success of the sintering process.

#### 4.1.2 Phases Present

The intermetallic centerline—the thin stripe visible between intermetallic layers in Figure 4.2f (indicated by arrow)—is not pure aluminum; it is composed of oxides, impurities, voids, and diffused titanium that was pushed toward the centerline during the reaction process. This was verified by EDS analysis of the intermetallic centerlines of MIL-11, MIL-3 and MIL-1 specimens (see Tables 4.2 – 4.4). Table 4.2 shows the chemical composition of the residual aluminum layer in MIL-11 at the points indicated in Figure 4.3. At positions 2 and 5, which are in close proximity to the  $\text{Al}_3\text{Ti}$  interface, the aluminum contains oxides and no diffused titanium. Positions 3 and 4—on either side of the centerline of the aluminum layer—show a composition that is still pure Al with no contaminants.



**Table 4.2 – Composition of the residual aluminum layer of MIL-11 determined by EDS.**

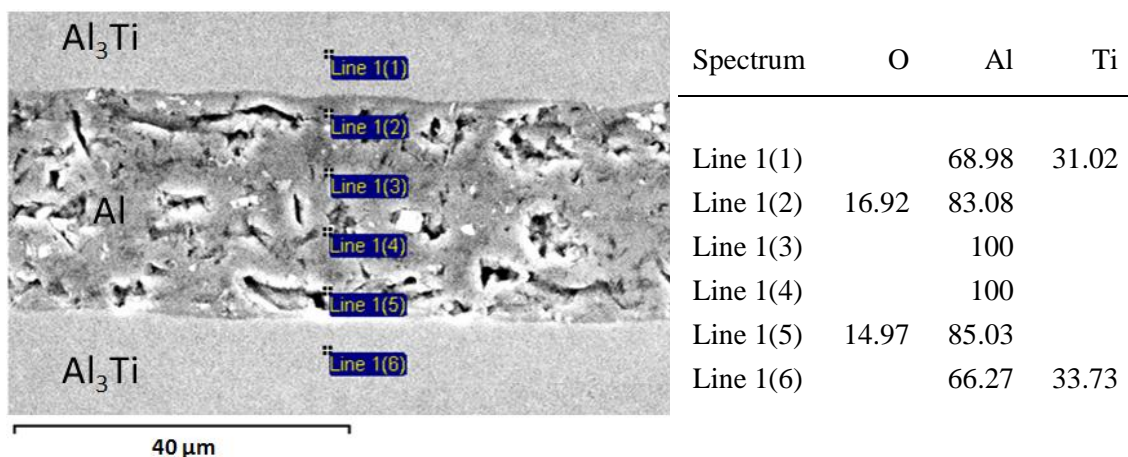


**Figure 4.3 – SEM micrograph of the Al layer of specimen MIL-11 showing the points used in EDS analysis.**

EDS analysis of specimens MIL-3 and MIL-1 shows a significant presence of oxygen and diffused titanium within the residual aluminum layer. Oxygen and titanium content is similar among the three specimens, and shows a pattern of increasing oxygen and decreasing Ti with increasing proximity to the Al centerline. From Table 4.3, there is very little pure Al remaining in MIL-3, though the EDS analysis was performed at only two points within the layer. Analysis of MIL-1 on the other hand (see Table 4.4) did show a small region of uncontaminated Al, so it cannot be assumed that pure Al no longer exists in the intermetallic centerline in MIL-3 and MIL-1.

Void growth and crack propagation in the aluminum layers were observed in the two [untested] specimens with the lowest residual aluminum content, indicated by arrows in Figure 4.6. Figures 4.4 and 4.5 also show anomalous Al deformation. One likely cause for this is a mismatch of thermal expansion coefficients and elastic moduli between the three components of the laminate composite, though the contribution of Al is negligible compared to Ti and  $\text{Al}_3\text{Ti}$ . During the cooling stage of the synthesis process, each layer cools and contracts at a different rate, which creates stresses at each material interface. In general, this residual stress

is determined by the elastic constants, relative concentrations, and the thermal expansion coefficients (CTE) of the matrix and reinforcement materials. Depending on the magnitude of these residual stresses, expansion and contraction can lead to either reversible elastic deformation of the matrix or irreversible plastic yielding, microcracking, creep, and interface decohesion [42]. When the MIL composite cools down,  $\text{Al}_3\text{Ti}$  (CTE:  $13 \times 10^{-6} / ^\circ\text{C}$ ) shrinks more than Ti-3Al-2.5V (CTE:  $9.61 \times 10^{-6} / ^\circ\text{C}$ ) because of its higher CTE. In addition to the difference in thermal expansion coefficients, the gap between elastic moduli is also large ( $E_{\text{Ti}} = 116 \text{ GPa}$ ,  $E_{\text{Al}_3\text{Ti}} = 215 \text{ GPa}$ ). The resulting mismatch of strain puts the titanium layer under compression and  $\text{Al}_3\text{Ti}$  layer under tension [52]. Due to the comparable thicknesses of the Ti and  $\text{Al}_3\text{Ti}$  layers and the high bond strength at those interfaces (metallurgical in nature), residual stress is concentrated in the thin, ductile, contaminate-heavy aluminum layer. The presence of oxides and impurities facilitates interface decohesion and cracking by reducing interlayer bond strength and increasing the number of crack nucleation sites.

**Table 4.3 – Composition of the residual aluminum layer of MIL-3 determined by EDS.**

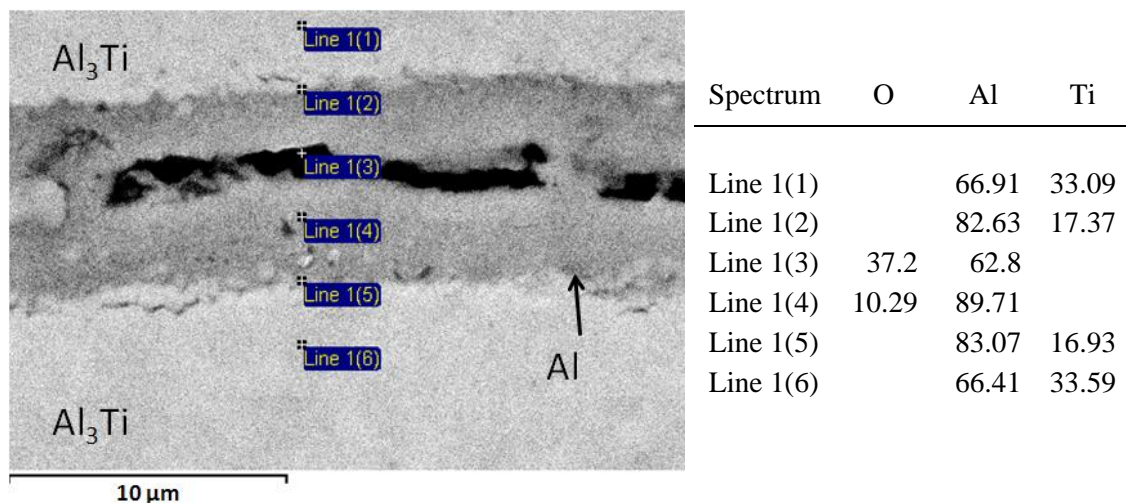


**Figure 4.4 – SEM micrograph of a broken portion of the Al layer of specimen MIL-3 showing the points used in EDS analysis.**

**Table 4.4 – Composition of the residual aluminum layer of MIL-1 determined by EDS.**

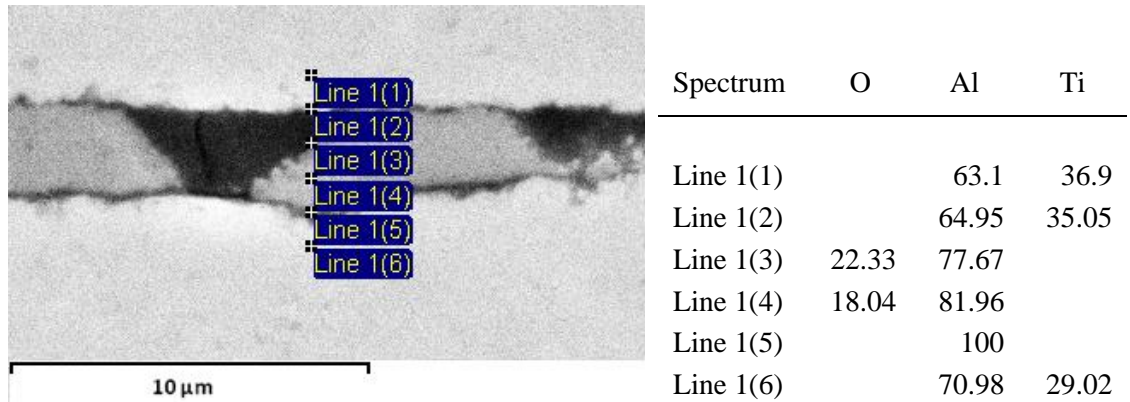


**Figure 4.5 – SEM micrograph of a broken and segmented portion of the Al layer of specimen MIL-1 showing the points used in EDS analysis.**

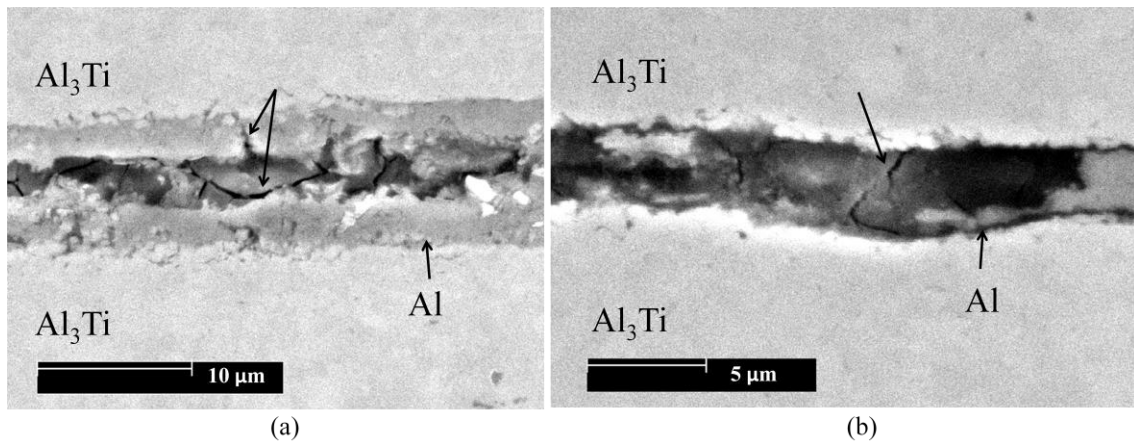


**Figure 4.6 – SEM micrographs of crack propagation and creep caused by residual thermal stresses in (a) MIL-3 and (b) MIL-1.**

## 4.2 Mechanical Properties

### 4.2.1 Quasi-Static Compression Testing

Compression tests were performed on small rectangular samples at strain rates of 0.001 /s. Both extreme layer orientations were tested for each specimen. A brief summary of the results is presented in Table 4.5. Graphical representation of the data is presented in Figure 4.7, showing the relationship between residual aluminum volume fraction and yield stress in the parallel and perpendicular orientations. In the perpendicular loading orientation, compressive strength increases steadily as Al content decreases. This is due to the growing volume fraction of  $\text{Al}_3\text{Ti}$  in the composite microstructure (see Figure 4.1b), which is much stronger than titanium and aluminum. The compressive strength of samples tested in the parallel orientation showed a similar trend, but the curve reaches a maximum when the volume fraction of Al reaches 0.109 (a reaction time of 2 hours). This maximum may represent the ideal volume fraction of residual aluminum in the composite. After the 11%Al mark, the return on compressive stress with increasing  $\text{Al}_3\text{Ti}$  volume fraction begins to diminish, along with the beneficial effects of the residual Al layer. The perpendicular curve also shows an irregularity at 11%Al, though in that case compressive strength begins to increase more rapidly. Combining performance results from both orientations in quasi-static compression, it can be seen that an optimal residual Al volume fraction may exist between 0.109 and 0.027.

Table 4.5 – Summary of yield stresses observed in dynamic compression testing.

Specimen	Al Volume Fraction	Yield Stress (MPa)	
		Parallel	Perpendicular
MIL-48	0.481	337.4	404.47
MIL-42	0.419	483.9	450.6
MIL-16	0.157	841.47	665.93
MIL-11	0.109	999.2	715.8
MIL-3	0.027	938.3	996.4
MIL-1	0.009	908.9	1047.9

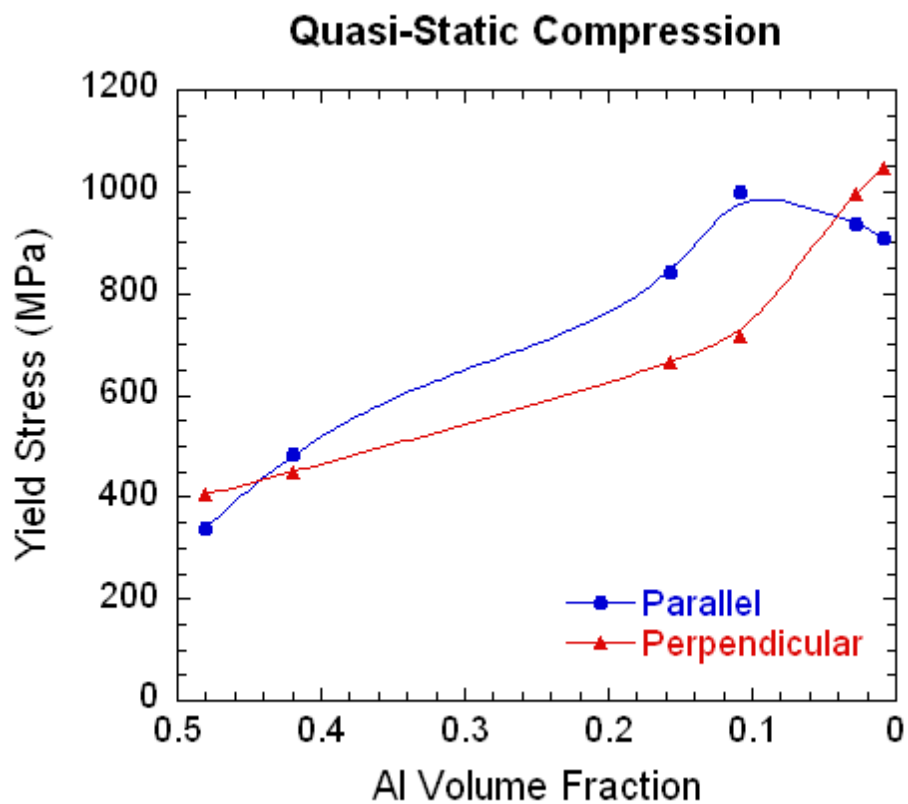
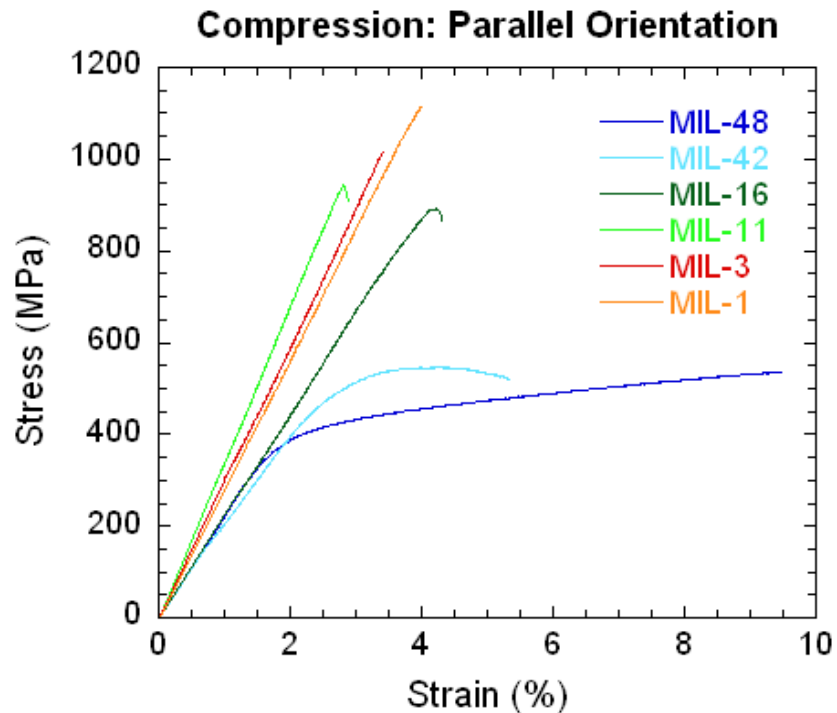


Figure 4.7 – Affect of residual aluminum volume fraction on compressive stress in parallel and perpendicular loading orientations.

#### 4.2.1.1 Layers Parallel to the Applied Load

Figure 4.8 is a compilation of representative stress-strain curves from each specimen with layers oriented parallel to the loading direction. In this orientation, there is almost no plastic behavior before failure, except in the MIL-48 and MIL-42 specimens, which have low intermetallic content and therefore higher toughness.



**Figure 4.8 – Representative stress-strain curves of each specimen tested under quasi-static compression at 0.001/s with layers oriented parallel to the applied load.**

MIL-48 was processed for 22 minutes, yielding final Ti and Al volume percents of 50.3 and 48.1 (respectively), with the intermetallic phase taking up the remainder. The average yield stress for these samples was 337.4 MPa, the lowest of the six specimens produced. Microstructural damage in these samples was minimal; failure was affected primarily by Ti and Al layer buckling near the sides and load face of the sample, as seen in Figure 4.9. Visible also are small regions of delamination, which were confined to these zones of plastic deformation. No shear fracture was observed in samples of this orientation.

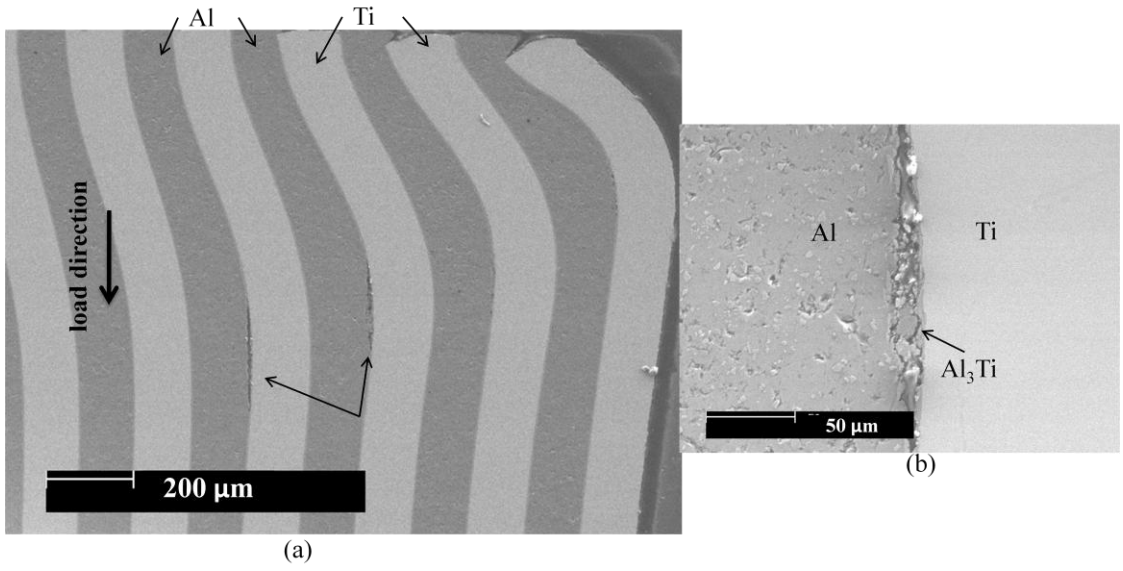


Figure 4.9 – SEM micrograph of MIL-48 sample (cold-mounted and polished after quasi-static compression) showing (a) buckling and (b) minor delamination cracking near the load face.

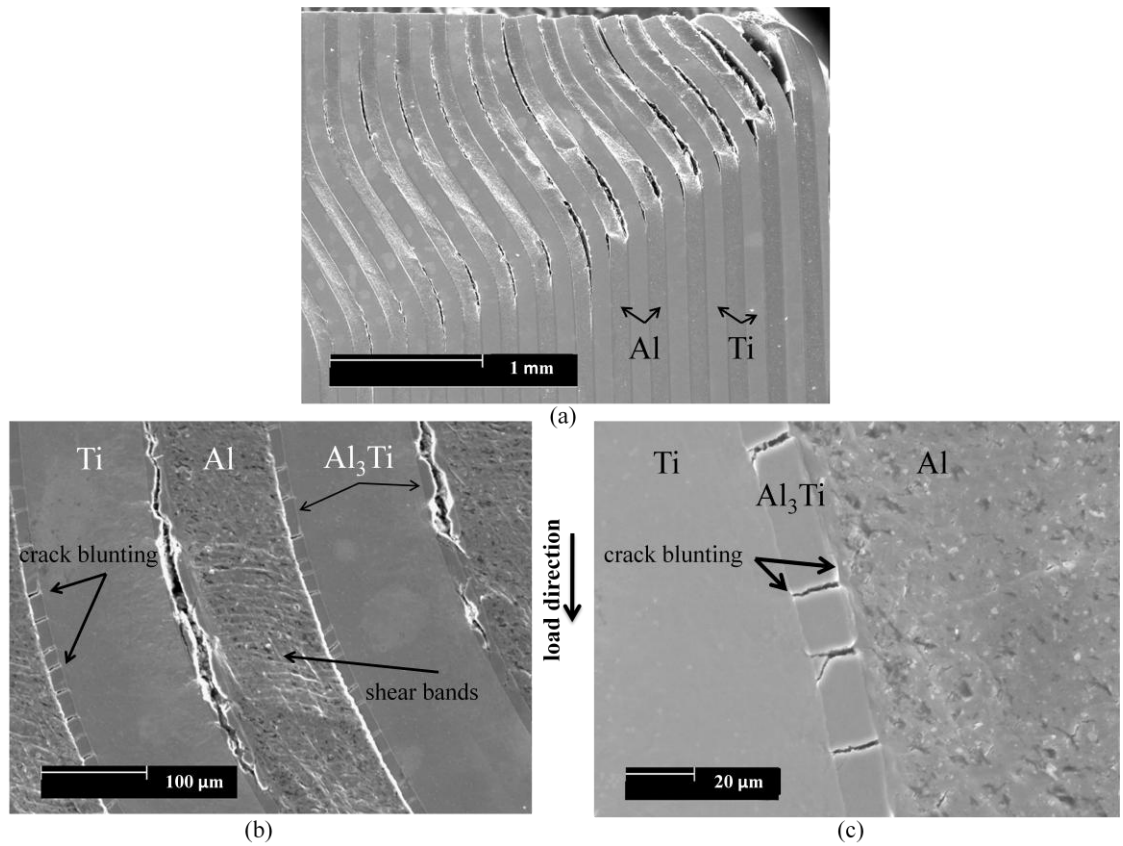


Figure 4.10 – SEM micrograph of MIL-42 sample under quasi-static compression (0.001/s) in parallel loading showing Al<sub>3</sub>Ti centerline cracking, shear band formation, and transverse cracking at regions of (a) large and (b) small deformation.

MIL-42 was processed for 30 minutes, yielding final Ti and Al contents of 49% and 42% (respectively), with the intermetallic phase at 9%. Parallel sample strength was increased from 337.4 to 483.9 MPa (43% increase) by the additional  $\text{Al}_3\text{Ti}$  content. It can also be attributed to an increase in bond strength at the Ti- $\text{Al}_3\text{Ti}$  and Al- $\text{Al}_3\text{Ti}$  interfaces (longer reaction time than MIL-48). Figure 4.10a is an SEM micrograph of a geometry-induced failure (load surfaces were not parallel) that shows shear deformation of the Al layers and intermetallic cracking and ply separation. Stress relief transverse cracking and centerline fracture of the thin  $\text{Al}_3\text{Ti}$  layer can also be seen (Figure 4.10b). Intermetallic cracks propagated through the Al layers by shear band formation (in this extreme case), renucleated in the adjacent intermetallic layers, and were blunted in the Ti layers. Figure 4.10c is a magnified SEM image of a region away from the failure zone showing crack tip blunting in the Ti and Al layers. The increased interfacial bond strength was the primary contributor to composite strength for this specimen, and the intermetallic layers were still thin enough to prevent catastrophic failure by brittle fracture. No shear fracture was observed in this loading orientation for MIL-42.

MIL-16 was processed for 1.5 hours, yielding a composite in which the intermetallic phase was on an equal footing with titanium (see Table 4.1 and Figure 4.1). As seen in Table 4.2, this change in microstructure led to a 74% increase in the average yield stress in the parallel loading orientation. The failure characteristics of these samples differed from those observed in MIL-48 and MIL-42 composites. Failure in this composite when loaded parallel to the layers was mainly by delamination at Ti- $\text{Al}_3\text{Ti}$  interfaces and Ti layer buckling (see Figure 4.11a, b), with crack bridging by the Ti and Al layers (see Figure 4.11c). Figure 4.11b is an SEM micrograph of a fracture surface showing brittle fracture of the intermetallic layers and ductile fracture of the Al layer. Also visible is a centerline crack in the intermetallic, and delamination from the bordering Ti layer on the extreme left. Parallel samples of this



specimen exhibited almost no plastic behavior prior to failure (see Figure 4.8). At this residual aluminum volume fraction, shear fracture emerged as a failure mode.

Generally there are two types of shear fracture in this loading orientation: one, “a-type” shear fracture propagating at a nearly  $45^\circ$  angle that cuts through one layer at a time, as shown in Figure 4.12a (and Figure 4.15a); two, “b-type” shear fracture that propagates at a  $45^\circ$  angle relative to the loading plane through all the layers at once, as shown in Figure 4.12b [51]. The type of shear fracture experienced by MIL-16 specimens was consistently b-type (without sample separation). Vecchio *et al.* [51] postulated that this type of fracture is related to good interfacial strength. Their results showed that additional shear deformation increased compressive strength in their MIL composites, which is corroborated by the present findings.

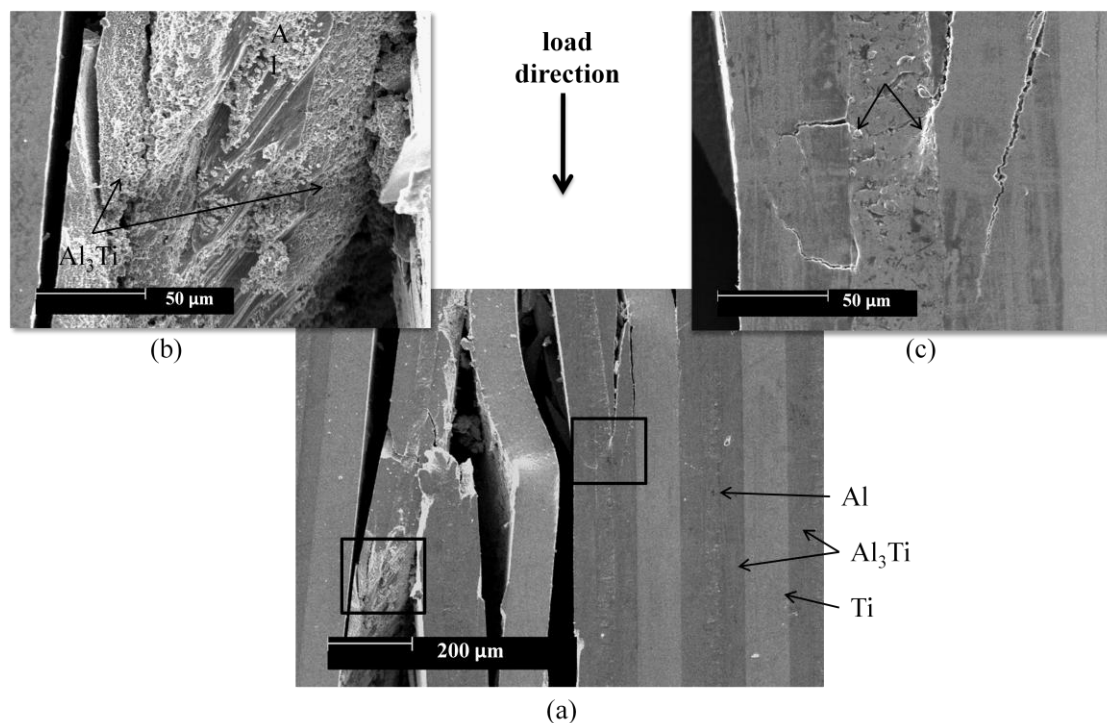


**Figure 4.11 – Fracture of MIL-16 under quasi-static compression (0.001/s) with layers oriented parallel the applied load: (a) cracked Al-Al<sub>3</sub>Ti layers and intact Ti layers, (b) magnification of fracture surface, (c) crack bridging by Al layer and shear band formation (arrows).**

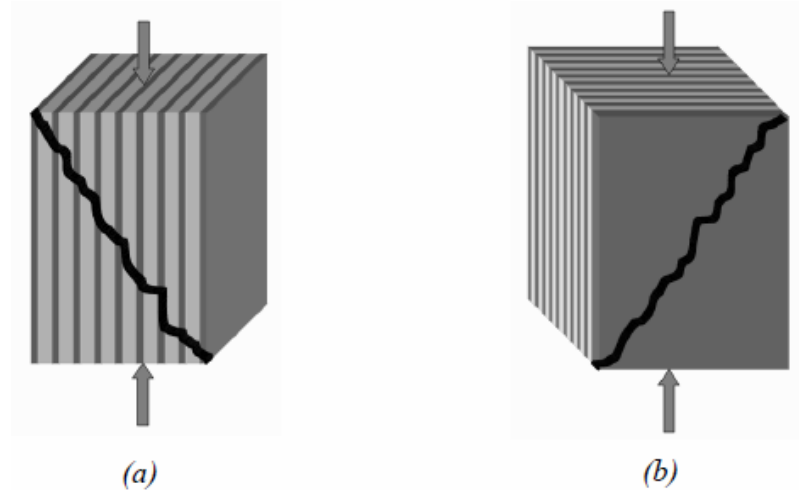


**Figure 4.12 – Diagram of two modes of shear failure common to MIL composites loaded parallel to the layers: (a) bisecting shear fracture propagating from interface to interface (a-type); (b) shear fracture that cuts diagonally across all layers of the composite simultaneously (b-type) [51].**

MIL-11 was processed for 2 hours, yielding a composite with a microstructure in which  $\text{Al}_3\text{Ti}$  had taken over as the dominant component. The volume fraction of  $\text{Al}_3\text{Ti}$  was 52%, compared to Ti and Al at 37.1% and 10.9%, respectively. Samples with this composition boasted an average compressive yield stress of nearly 1 GPa under parallel loading. This yield stress represents the maximum value observed among parallel samples, and the second highest value among all samples tested in quasi-static compression. Analysis of the failure mechanisms illustrated in Figure 4.13 shows a departure from previously prevalent mechanisms. Prior to MIL-11, samples that failed by delamination did so cleanly, as in Figure 4.11 where a high-energy fracture propagated to a Ti- $\text{Al}_3\text{Ti}$  interface and separated the layers. However, as seen in Figures 4.13a and 4.13b, a major crack propagating downward in the  $\text{Al}_3\text{Ti}$  layer ignored the Al interface almost entirely, resulting in zone shielding by microcracking and plastic deformation of the aluminum. There were many other instances in MIL-11 samples where separation occurred without clean delamination: Figure 4.13c is a failure mode not observed in samples of any other Al volume fraction, in which a portion of the Al layer was torn off at several points along a delaminated interface.

Comparing Figures 4.13b and 4.13c to Figure 4.3, it is clear that the portion of the Al layer that was cracked and torn shows roughly 16% oxygen content (from Table 4.2). Figure 4.13d is an SEM micrograph of a failed sample that was cold mounted and polished (to final polish) that shows intermetallic layer centerline fracture and crack propagation through an aluminum layer. B-type shear fracture was observed in all three samples (without sample separation). A novel fracture mechanism and higher  $\text{Al}_3\text{Ti}$  content substantially increased the strength of MIL-11 in loading parallel to the layers, but also lessened the toughness of the specimen (see Figure 4.8).

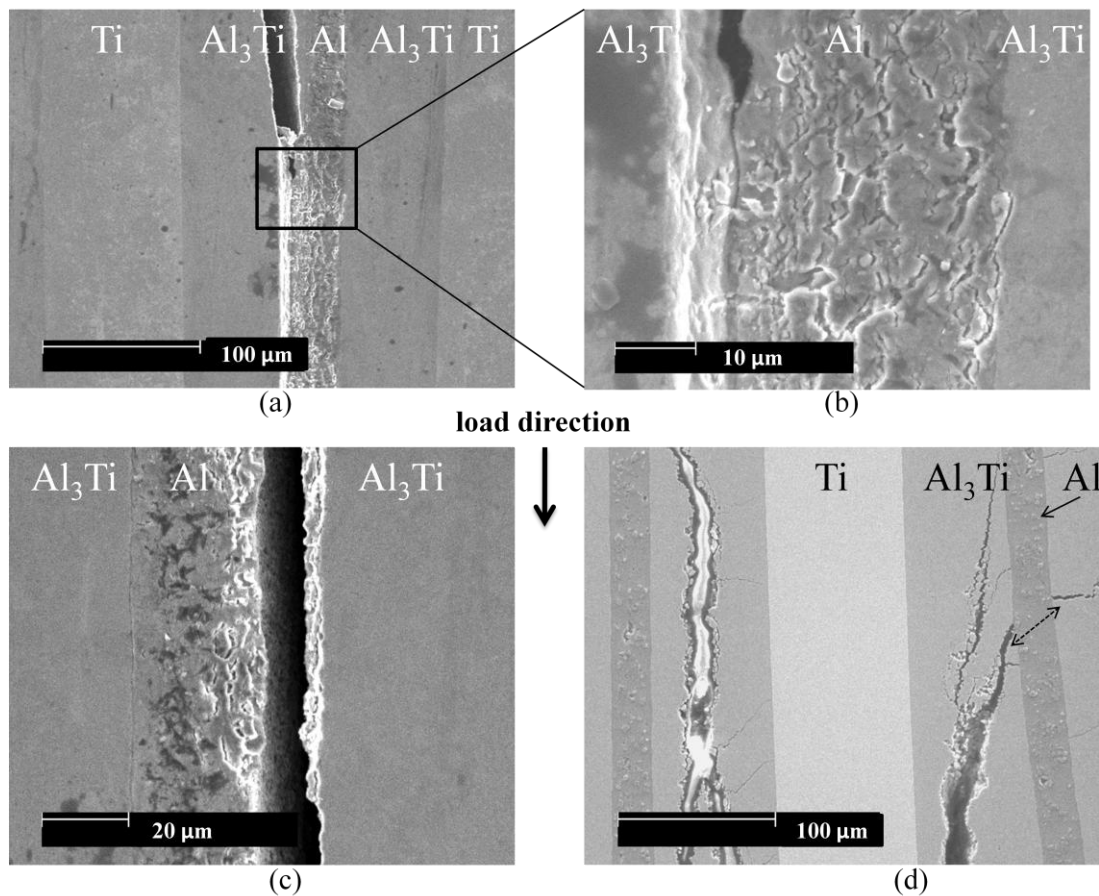


**Figure 4.13 – Fracture of MIL-11 under quasi-static compression (0.001/s) with layers oriented parallel to the applied load. SEM micrographs showing: (a) crack blunting in Al layer; (b) magnification of microcracking and plastic deformation; (c) fracture without clean delamination; (d)  $\text{Al}_3\text{Ti}$  centerline fracture and crack propagation through the Al layer.**

MIL-3 was processed for 3 hours, yielding a composite with a microstructure in which aluminum had a volume percent of only 2.7%. This substantial reduction in Al content led to a marked decrease in compressive yield stress when loaded in the parallel orientation. Samples showed distinctly brittle behavior, and yield and failure occurred almost simultaneously. The average yield stress among parallel samples was 938 MPa. In this orientation, catastrophic failure was by Ti layer buckling, through-thickness interface delamination, and a-type shear fracture. Figure 4.14a shows delamination of an MIL-3 sample (cold-mounted and polished after testing) in which a layer of ductile Ti remained bonded to an  $\text{Al}_3\text{Ti}$  bilayer (which comprises two  $\text{Al}_3\text{Ti}$  layers with a residual aluminum centerline). Cracking in the bilayer ignored the residual Al layer.

A new failure mechanism appeared in samples of this specimen: transverse shear cracking in the intermetallic bilayers (Figures 4.14b,c,d). The inclined crack moved from intermetallic bilayer to intermetallic bilayer (Figure 4.13b), with no through-thickness deformation of the Ti layers. Minor plastic deformation caused by stress concentrations at the crack tips terminating in Ti layers was observed, but the main cracking propagated by a leap-frogging pattern of blunting and renucleation. When the main crack reached a new  $\text{Al}_3\text{Ti}$  bilayer, a transverse crack opened that either split the Al centerline (Figure 4.13d) or traveled along it for a short distance (Figure 4.13c). Al layer necking can be seen in the case where the crack opened without traveling. As the crack expanded to the left and right in the bilayer, a closing traction exerted by the reinforcing Ti layers on either side caused the main crack to bifurcate into smaller cracks, all of which eventually terminated at the Ti interface. The introduction of this fracture mechanism corresponds to the drop in compressive strength seen in samples with Al content below 11%.

MIL-1 was processed for 3.5 hours and showed another sharp decrease in yield strength to 909 MPa. Much like MIL-3, samples showed almost no ductility prior to failure,

and also showed the same transverse cracking in the intermetallic bilayers. Catastrophic failure was mixed-mode, and varied slightly among the three samples tested. One sample showed a-type shear fracture (without sample separation) and buckling, as shown in the SEM micrograph in Figure 4.15a and 4.15b. The sample shown in Figure 4.15c failed by interfacial delamination (with sample separation), and the third sample showed b-type fracture (without separation) and interfacial delamination (with separation). Figure 4.15c and 4.15d show transverse intermetallic cracking similar to what was seen in MIL-3. The continued decrease in yield strength is further indication that MIL-11 has an ideal microstructure for compression in parallel loading.

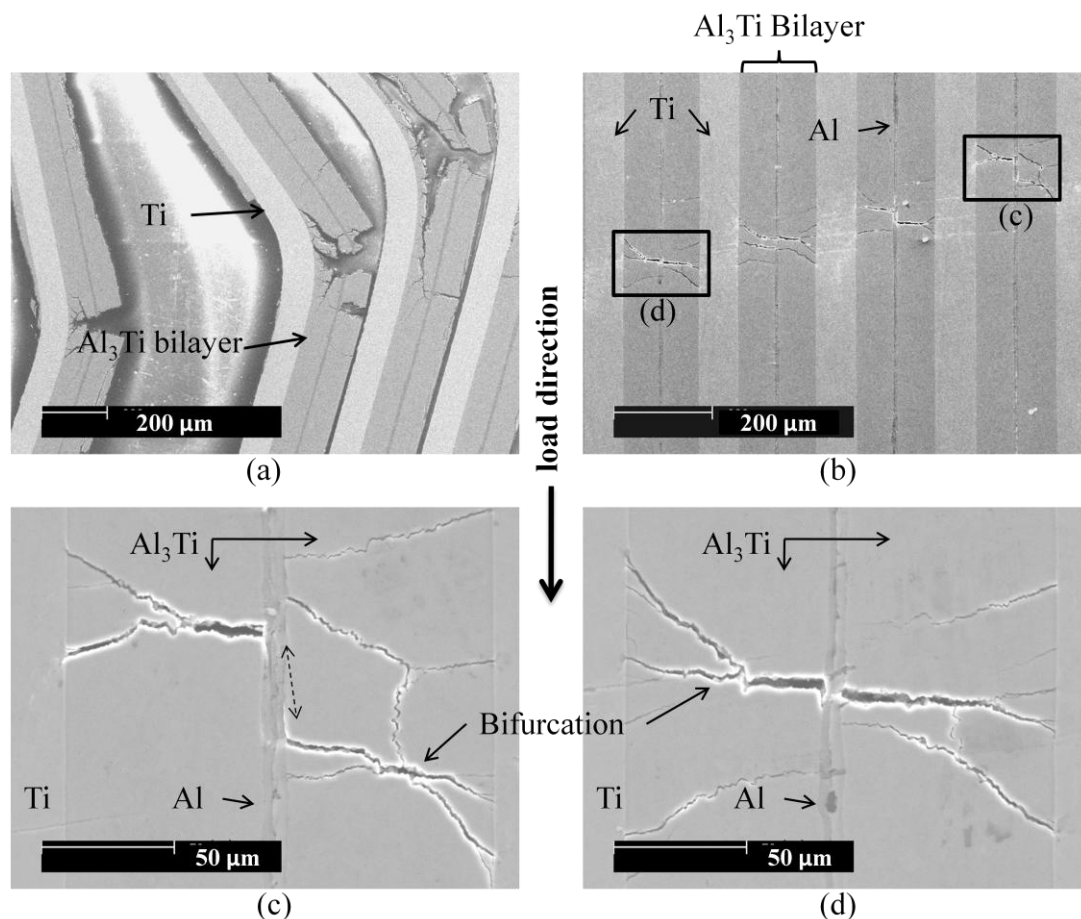


**Figure 4.14 – Fracture of MIL-3 under quasi-static compression (0.001/s) with layers oriented parallel to the applied load. SEM micrographs showing: (a) ductile Ti buckling and brittle Al<sub>3</sub>Ti fracture ignoring the residual Al, (b) transverse cracking in Al<sub>3</sub>Ti, (c) and (d) unique crack opening in intermetallic bilayers.**

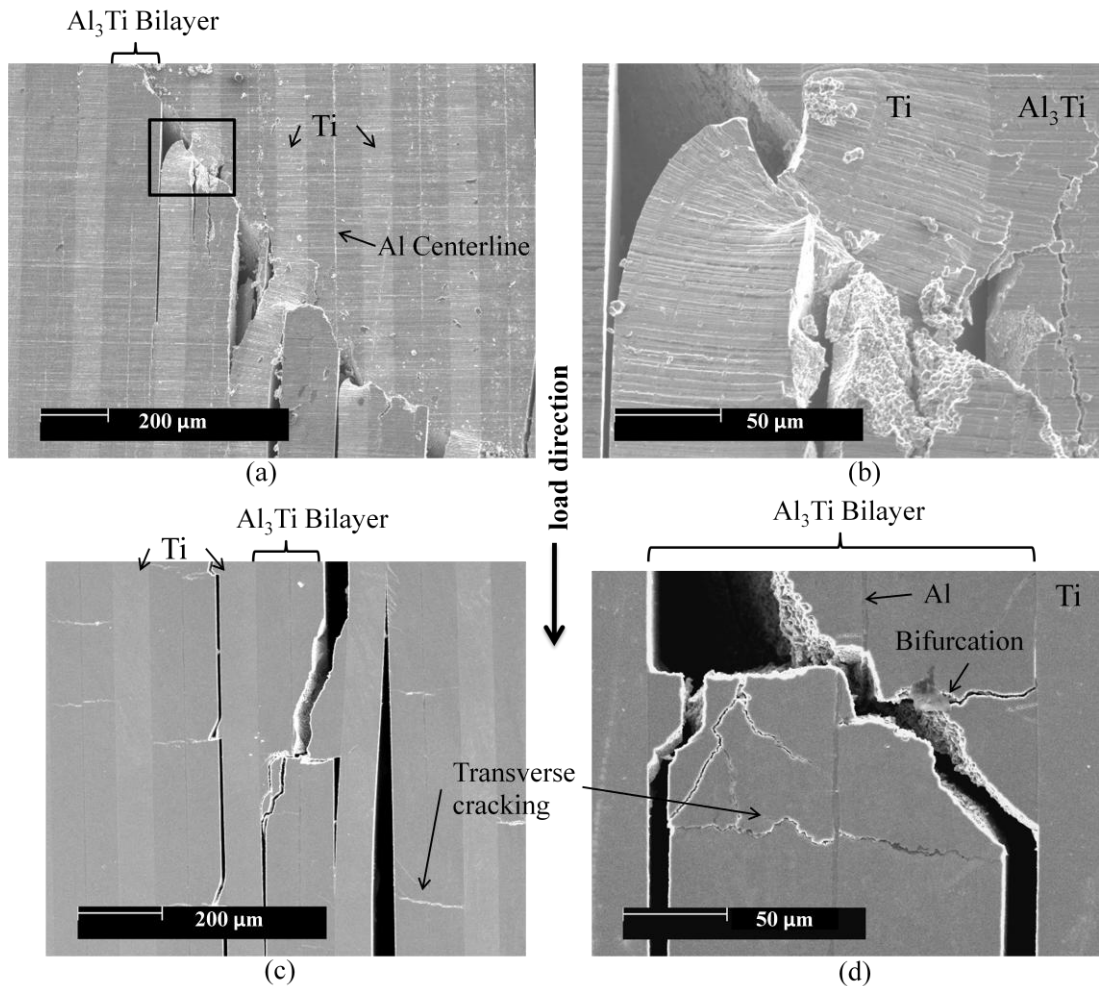


**Figure 4.15 – SEM micrograph of MIL-1 showing: (a) and (b) a-type shear fracture with and without Ti layer failure (unpolished sample); (c) and (d) transverse cracking and Al<sub>3</sub>Ti bilayer delamination from Ti layers (sample polished prior to testing).**

#### 4.2.1.2 Layers Perpendicular to the Applied Load

Figure 4.16 is a compilation of representative stress-strain curves from each MIL composite with layers oriented perpendicular to the loading direction. Samples from every specimen showed some degree of plastic behavior after yield, though toughness decreased with Al volume fraction. In this orientation, specimen yield stress increased steadily from MIL-48 to MIL-11, and then more steeply as the Al layer thinned in favor of  $Al_3Ti$  formation (see Figure 4.7). Behavior was more uniform among similar specimens compared to performance in parallel loading (see Figure 4.8); stress-strain curves show grouping by like residual Al content.

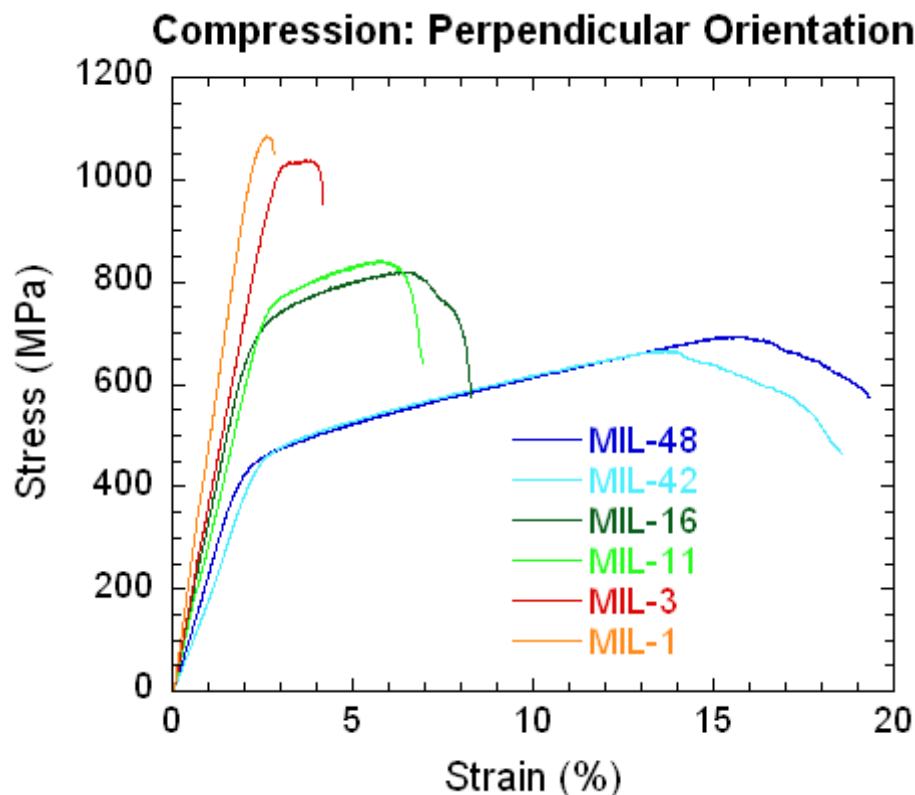


**Figure 4.16 – Representative stress-strain curves of each specimen tested under quasi-static compression at 0.001/s with layers oriented perpendicular to the applied load.**

MIL-48 samples loaded in the perpendicular orientation had an average yield stress of 404.5 MPa. Samples did not fail by shear fracture, but by macroscopic plastic deformation and small scale delamination (Figure 4.17). No cracking or shear fracture was observed in samples of this composite. MIL-48 showed higher compressive strength in this orientation than it did when loaded parallel to its layers.

MIL-42 behaved very similarly to MIL-48, showing the low strength and high toughness characteristic of a still primarily Ti-Al composite. Deformation was primarily plastic, but with the added failure mechanisms of intermetallic layer cracking and shear fracture. An arrested a-type shear fracture can be seen in the SEM micrograph in Figure 4.18, in which the crack cut cleanly through each layer without significant interface-induced deflection. Plastic necking of the Al layers is evident, as is ductile fracture of the Ti layers. When loading was stopped between yield and failure, the microstructure of MIL-42 showed small scale delamination similar to MIL-48, in addition to vertical cracks (Figure 4.18d). The slightly elevated intermetallic content in MIL-42 had little effect on its yield strength, showing an increase of only 46 MPa and a small reduction in energy absorbance prior to failure.

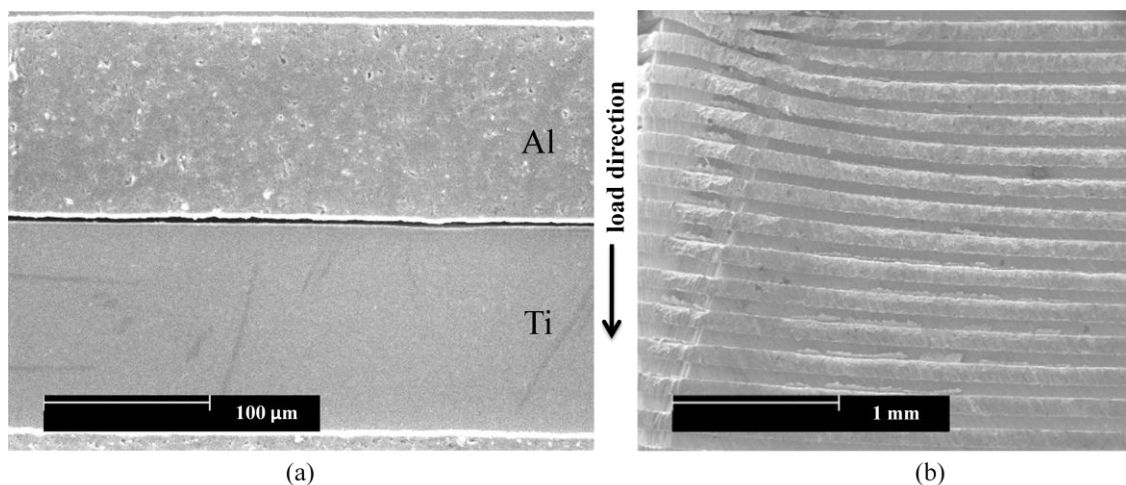


**Figure 4.17 – SEM micrographs of MIL-48 and (a) stopped before the failure strain showing small scale delamination, and (b) macroscopic deformation and Al expulsion of a failed sample.**



MIL-16 samples exhibited greatly increased yield strength, the average being 665.9 MPa. Due to the greater  $\text{Al}_3\text{Ti}$  layer thickness, failure was dominated by cracking,  $\text{Al}_3\text{Ti}$  segmentation, and Ti layer shearing (Figure 4.19a). The amount of residual aluminum in the microstructure was able to prevent the a-type shear from fracturing the sample completely. Figure 4.19b shows the torturous path created for crack propagation through Ti- $\text{Al}_3\text{Ti}$  and Al- $\text{Al}_3\text{Ti}$  interfaces. An early stage of intermetallic segmentation is shown in Figures 4.19c, which is an SEM micrograph of a sample that was stopped prior to catastrophic failure. Shear band formation can be seen where vertical  $\text{Al}_3\text{Ti}$  cracks were blunted at the Ti- $\text{Al}_3\text{Ti}$  interface. There was no indication of renucleation through the Ti layers in the pre-failure sample, which resulted in the observed stress-relief crack distribution.

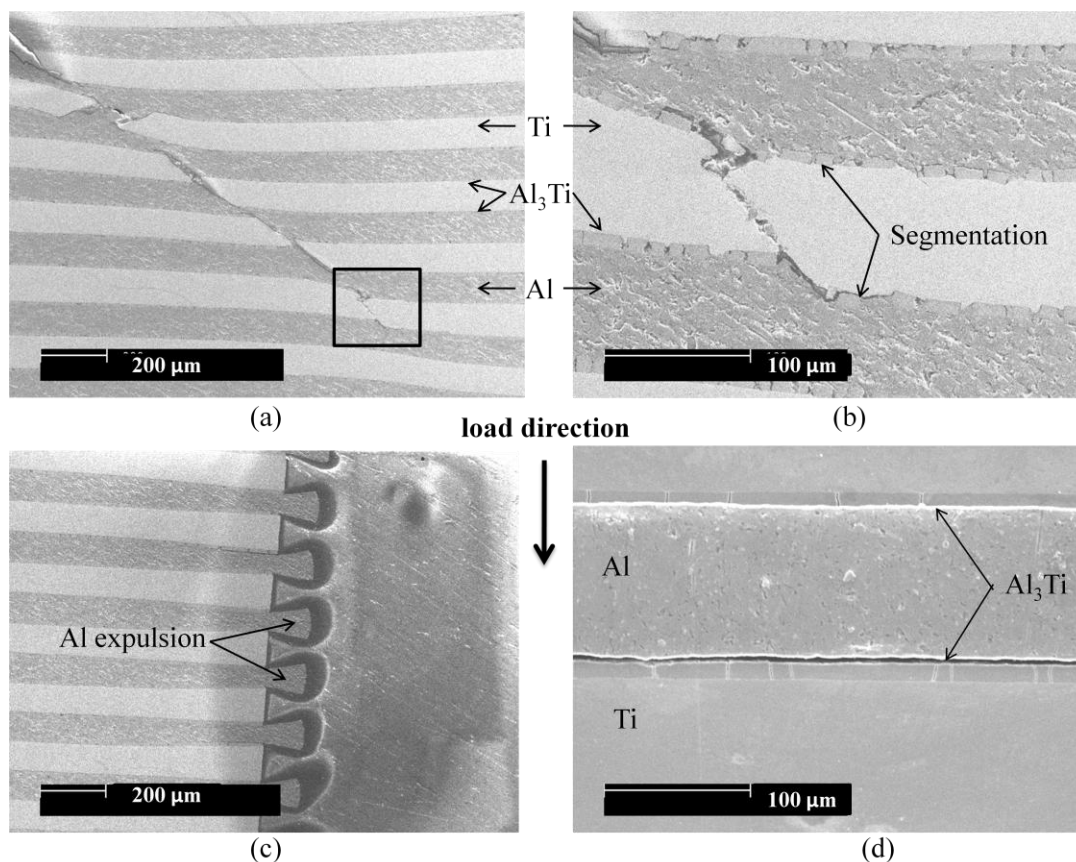


**Figure 4.18 – SEM micrograph of MIL-42 showing: (a) arrested a-type shear fracture, (b) intermetallic cracking and segmentation, (c) aluminum expulsion, and (d) stress relief cracking and delamination (pre-fail).**

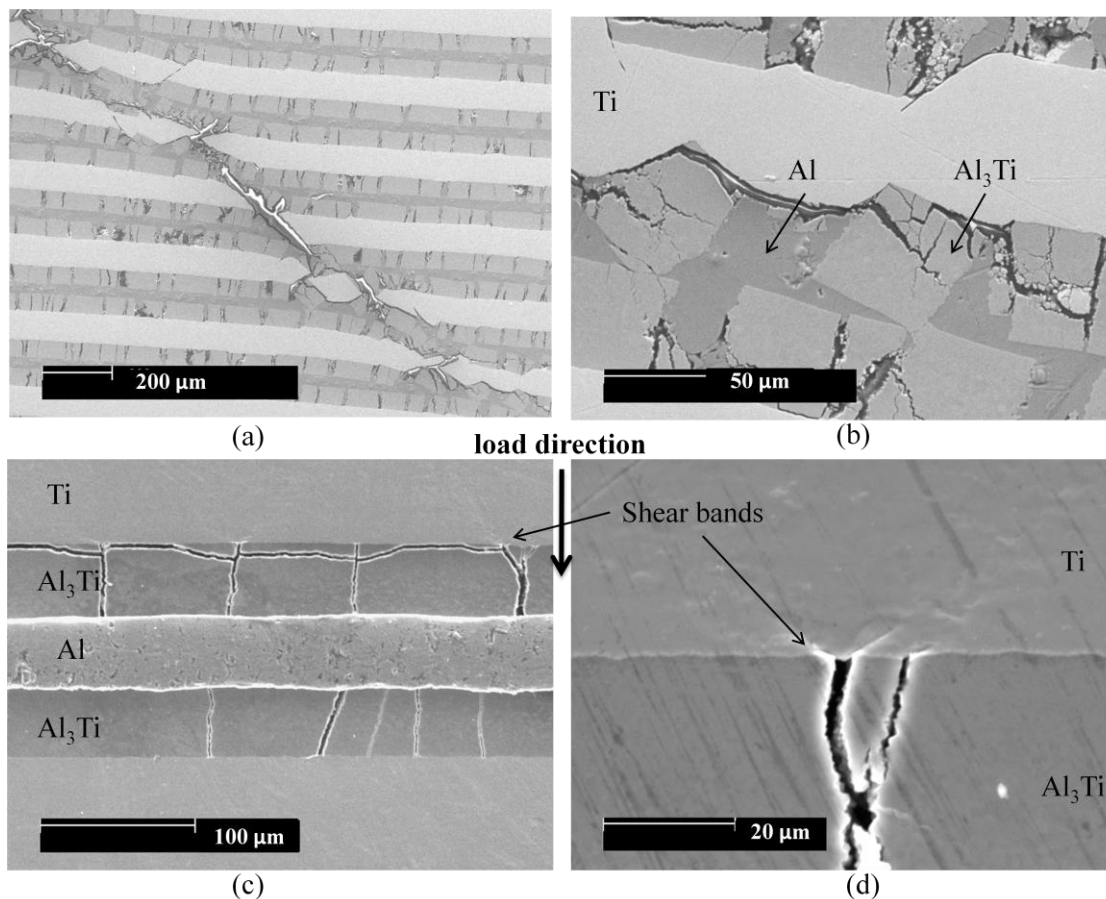


**Figure 4.19 – SEM micrograph of MIL-16 showing: (a) a-type shear fracture; (b) intermetallic segmentation, Ti deformation, ductile Al reinforcement; (c) and (d) shear band formation in a sample stopped between yield and failure strain.**

MIL-11 samples had an average yield stress of 715.8 MPa, and exhibited a stress-strain response very similar to MIL-16 (see Figure 4.16). However, the sample that failed catastrophically did so by a-type shear fracture (Figure 4.20a) that propagated through the entire sample (without arresting as in MIL-16 and MIL-42). The layers of residual aluminum were still sufficiently thick to maintain the amount of microstructural crack tip blunting present in MIL-16. Figures 4.20a and 4.20b are SEM micrographs of typical intermetallic

crack patterns after and before failure, respectively. Notice that prior to the ultimate stress, there is an horizontal offset between vertical intermetallic cracks caused by the ductile layer of aluminum. Even after the sample reached its ultimate stress the aluminum layer acted as a barrier to collinear crack re-nucleation. It can be seen that MIL-11 possesses a microstructure with an  $\text{Al}_3\text{Ti}$  volume fraction high enough to provide ample compressive strength, and to prevent failure by mechanisms seen in MIL-3 and MIL-1.

With an average yield stress of 996.4 MPa, MIL-3 showed a significant increase in strength over MIL-11, similar to the difference in strength between MIL-42 and MIL-16 (see Figure 4.7). In tests performed below the specimen's ultimate strength, MIL-3 samples began to exhibit "bilayer" behavior: failure behavior characteristic of one  $\text{Al}_3\text{Ti}$  layer with a residual Al centerline instead of two distinct  $\text{Al}_3\text{Ti}$  layers separated by an Al layer. This behavior was also observed in tests where MIL-3 was loaded parallel to the layers (see Figure 4.14a). Transverse cracks propagating in  $\text{Al}_3\text{Ti}$  layers showed increased interaction with the Al centerline, as shown in Figure 4.20d where a crack passed through the residual aluminum. This level of interaction was not seen in specimens with lower residual Al content, especially in samples not loaded to failure. The extensive deformation made possible by the reduced thickness of the Al layer permitted almost uninhibited crack re-nucleation (within intermetallic bilayers, not between them). Figure 4.20c shows the microstructural damage surrounding a shear fracture zone in a failed MIL-3 sample. There are similarities to MIL-11 failure, but on average damage was more severe.

MIL-1 showed the highest average compressive strength of all the MIL composite specimens tested. The average yield stress was 1047.9 MPa. However, the samples showed distinctly brittle behavior after yield (see Figure 4.16). Table 4.1 shows that  $\text{Al}_3\text{Ti}$  content did not increase significantly from MIL-3, so the factor most likely responsible for the increase in strength and loss of toughness is the reduction of residual Al. The failed sample shown in

Figure 4.21a and 4.21b exhibited much less microstructural cracking than samples from previous specimens, with catastrophic failure primarily manifested by a single, through-sample, step-wise shear fracture. Figure 4.21b is an enlargement of the fracture surface shown in 4.21a, illustrating the perfect 45° shear of the Ti layer, and the vertical, brittle fracture of the intermetallic bilayer. Comparing the microstructures of samples stopped before failure in Figures 4.20d and 4.21c, it is evident that the residual Al layer provided far less ductile reinforcement than in specimens with higher Al content; the meandering transverse crack propagated right through the Al layer into the next intermetallic layer.

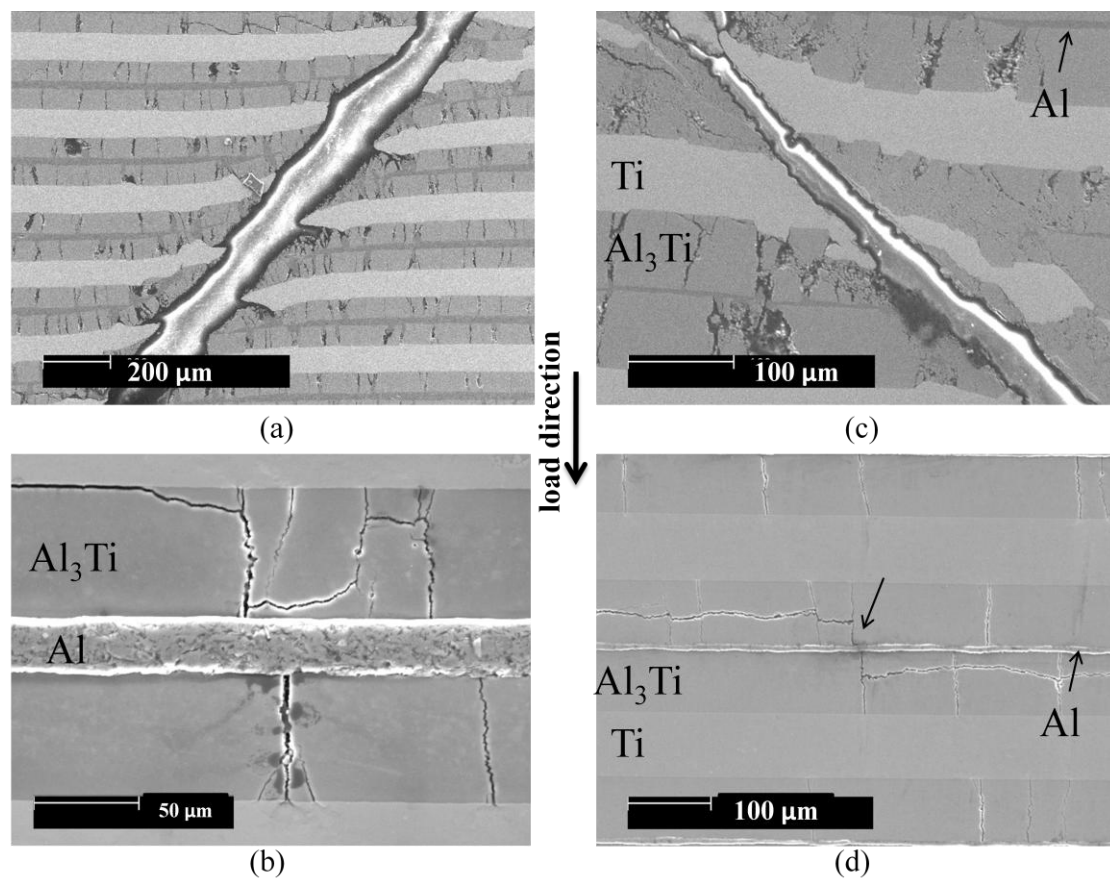
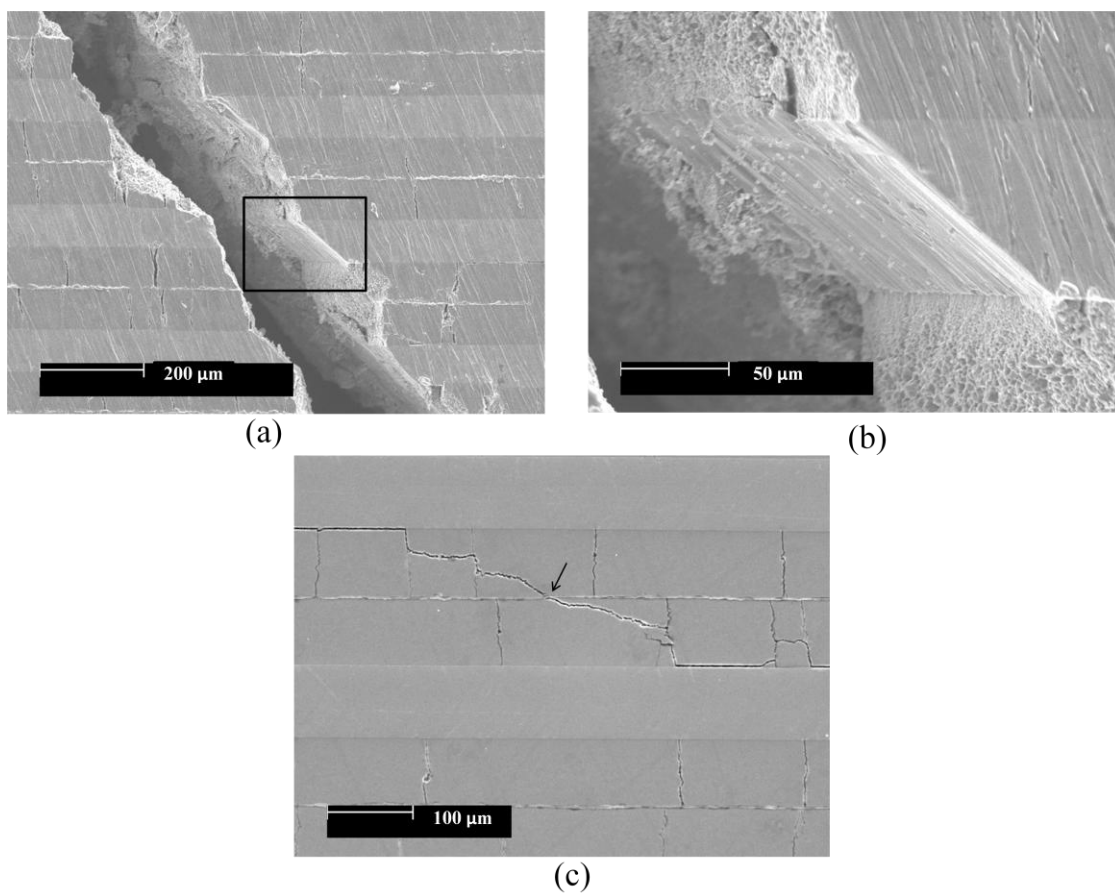


Figure 4.20 – SEM micrographs comparing catastrophic failure and cracking before failure in (a), (b) MIL-11 and (c), (d) MIL-3.



**Figure 4.21 – SEM micrographs of MIL-1: (a) and (b) catastrophic failure by a-type shear fracture; (c)  $\text{Al}_3\text{Ti}$  crack ignored residual Al centerline in a sample stopped before failure.**

#### 4.2.2 Quasi-Static Four Point Bend Testing

Four point bend (4PB) tests were performed on small rectangular beams (see Figures 3.3 and 3.4) at strain rates of  $10^{-3}$ /s. Both extreme layer orientations were tested for each specimen. A brief summary of the results is presented in Table 4.6. Graphical representation of the data is presented in Figure 4.22, showing the relationship between residual Al content and fracture toughness in the parallel and perpendicular orientations. Both loading orientations show low fracture toughness at 48%Al, which is most likely due to poor interlaminar bonding resulting from the short processing time (22 minutes). In general, materials with high ductility have higher fracture toughness, so MIL-48 should have shown significantly better performance, considering its microstructure is primarily Ti and Al. MIL-42, which was processed for 30 minutes and had an aluminum content of 41.9%, had the highest  $K_{IC}$  value of all six specimens in both orientations. Thus, 30 minutes must be sufficient to ensure good bond strength between layers. In the parallel loading orientation (crack divider), fracture toughness decreased steadily with decreasing Al volume fraction, indicating a reduction of ductile reinforcement as intermetallic content increased. In loading perpendicular to the layers (crack arrester), fracture toughness showed a similar decreasing trend, with irregularities most likely caused by changes in failure mechanisms. Comparing Figure 4.22 to the compression results (Figure 4.7), one sees further evidence that an ideal residual Al volume fraction may exist between 0.027 and 0.109.

Table 4.6 - Summary of fracture toughness values observed in quasi-static 4PB testing.

Specimen	Al Volume Fraction	$K_{IC}$ (MPa $\sqrt{m}$ )	
		Parallel	Perpendicular
MIL-48	0.481	20.86	14.16
MIL-42	0.419	31.65	20.14
MIL-16	0.157	28.19	10.76
MIL-11	0.109	26.83	12.09
MIL-3	0.027	24.91	12.99
MIL-1	0.009	24.47	8.88

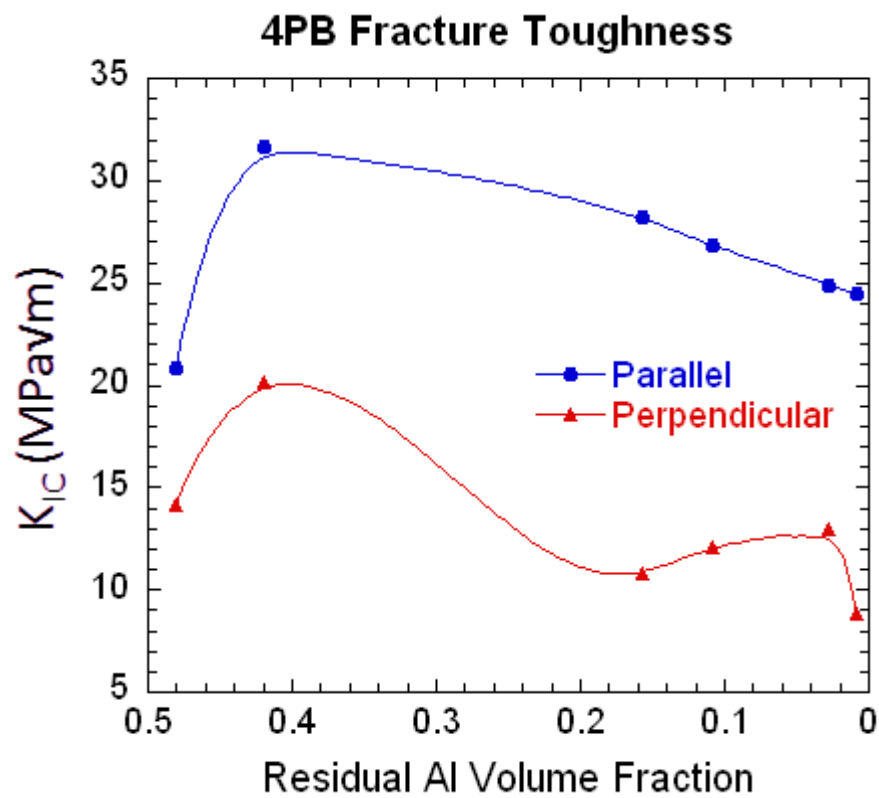
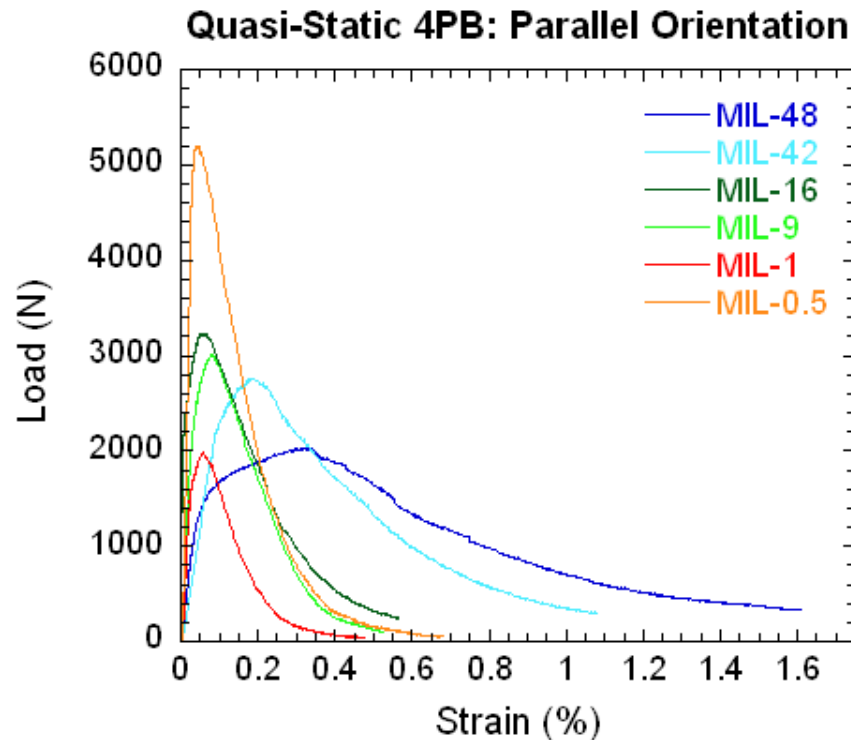


Figure 4.22 – Affect of residual aluminum volume fraction on fracture toughness in parallel and perpendicular loading orientations.



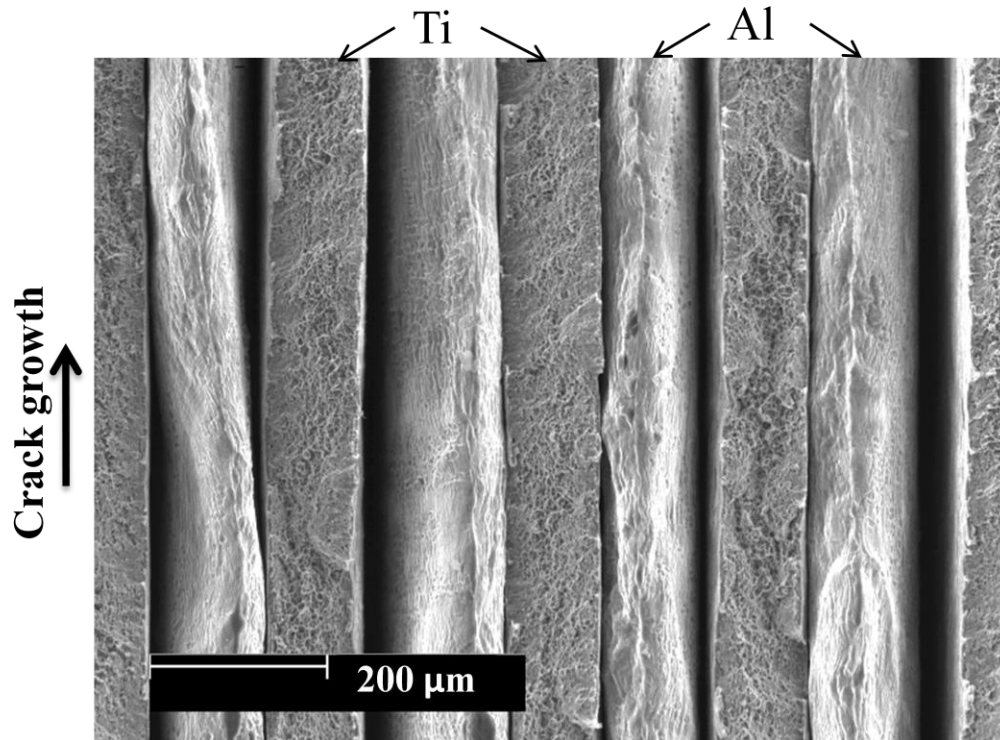
#### 4.2.2.1 Layers Parallel to the Applied Load

Figure 4.23 is a compilation of representative (maximum) load-strain curves from each specimen in the crack divider orientation. Though the load-strain curve is dependent on sample dimensions, a general decrease in crack opening displacement prior to failure (i.e. plastic deformation) can be seen.



**Figure 4.23 – Representative stress-strain curves of each specimen tested under quasi-static 4PB at 0.001/s with layers oriented parallel to the applied load.**

MIL-48, being only 1.6% brittle intermetallic phase, showed distinctly ductile behavior, and so should have had the highest fracture toughness. However, poor bonding between layers (seen in quasi-static compression tests as well) yielded a resistance to brittle fracture of only  $20.86 \text{ MPa}\sqrt{\text{m}}$ . Figure 4.24 shows flat, ductile fracture of the Ti layers, and tearing/necking of the Al layers. The dark gaps between layers are delaminated regions, which is a failure mechanism that occurred much less often in other specimens.



**Figure 4.24 – SEM micrograph of the fracture surface of MIL-48 in quasi-static bending showing ductile fracture, tearing, and delamination.**

MIL-42 had a fracture toughness of  $31.65\text{MPa}\sqrt{\text{m}}$ , indicating primarily ductile behavior. The failure mechanisms observed in MIL-48 can also be seen in Figure 4.25a, with the addition of intermetallic cracking. Figure 4.25b shows  $\text{Al}_3\text{Ti}$  centerline fracture and transverse cracking, as well as significant ductile tearing of the Al layers. In samples of this specimen, the  $\text{Al}_3\text{Ti}$  layer was sufficiently thin so that failure resulted in segmentation into small ( $\sim 100\mu\text{m}$ ) rectangular prisms (Figure 4.25c). During delamination, a majority of the  $\text{Al}_3\text{Ti}$  remained bonded to the Ti, with some segments torn off by the Al. No other specimen's failure mechanisms included the formation of these intermetallic fragments. Delamination was far less common in MIL-42 compared to MIL-48. This, in conjunction with the intermetallic fragmentation, proved that interlaminar bond strength increased greatly in MIL-42 (due to the longer processing time). The primary toughening mechanism in MIL-42 was crack tip

convolution, in which overall crack front growth was retarded by the plastic tearing required for crack growth in the more ductile layer (Al).

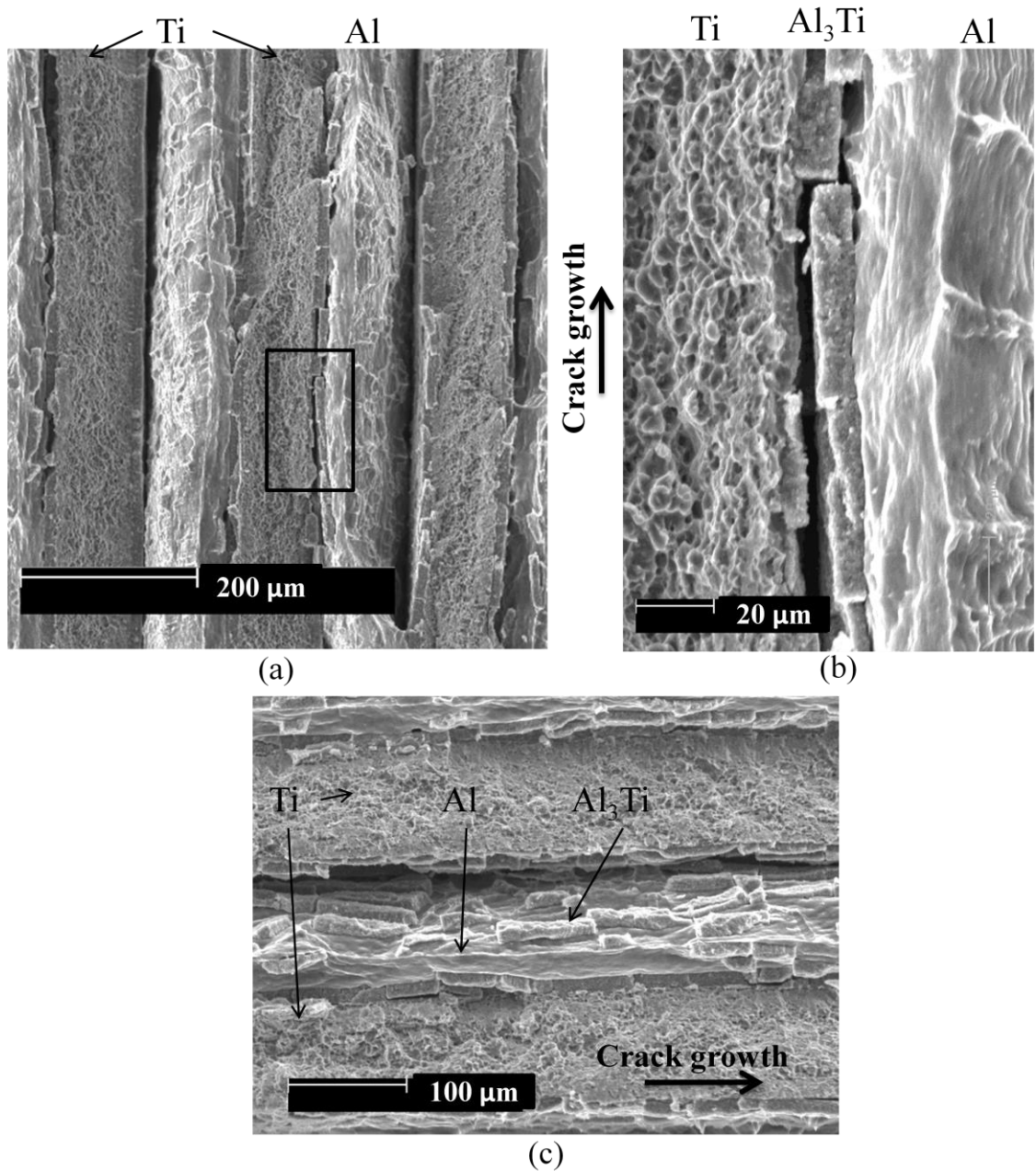


**Figure 4.25– SEM micrographs of the fracture surface of MIL-42 crack divider samples in quasi-static bending. (a) Ductile fracture of Ti layers, Al layer tearing, and Al<sub>3</sub>Ti layer cracking. (b) Detail of image (a) showing Al<sub>3</sub>Ti cracking. (c) Segmented Al<sub>3</sub>Ti fragments still bonded to Al layer after separation indicative of increased interlaminar bond strength.**

MIL-16 bend samples had an average fracture toughness of  $28.19 \text{ MPa}\sqrt{\text{m}}$ , which was not significantly lower than MIL-42 considering the sizeable drop in Al volume fraction; the largest contributing factors to fracture toughness in this orientation were increased  $\text{Al}_3\text{Ti}$  content and the remaining ductile aluminum reinforcement. The fracture surface of MIL-16 crack divider samples (Figure 4.26a) was characterized by rough, uneven brittle fracture of the intermetallic layers, microvoid coalescence and slant fracture in the Ti layers, and necking/tearing of the Al layers (Figure 4.26b). Slant fracture of the Ti layer may have been due to the formation of non-coplanar cracks in adjacent  $\text{Al}_3\text{Ti}$  layers [43] and could have contributed to the high fracture toughness observed. The Al layer provided enough ductile reinforcement to prevent the flat fracture of the  $\text{Al}_3\text{Ti}$  layers seen in specimens with less Al content. There was also significantly less failure by clean delamination; a majority of the interfacial damage was cracking and separation of the intermetallic phase from the Ti layers, leaving some  $\text{Al}_3\text{Ti}$  still bonded to the Ti.  $\text{Al}_3\text{Ti}$  centerline fracture was present but intermittent, as cracking was interrupted or diverted at intervals by transverse cracks.

MIL-11 showed fracture mechanisms common to both MIL-16 and MIL-3. Flat cleavage fracture of the  $\text{Al}_3\text{Ti}$  layers was more prevalent as a failure mechanism than the uneven fracture seen in MIL-16 (comparing Figures 4.26a and 4.27a). This is indicative of increasing brittleness, and explains the decrease in fracture toughness from  $28.19$  to  $26.83 \text{ MPa}\sqrt{\text{m}}$ . Figures 4.27b and 4.27c show  $\text{Al}_3\text{Ti}$  centerline fracture and microcracking along the  $\text{Al}_3\text{Ti}$ -Ti interfaces. In MIL-11, the residual Al layer was still thick enough to fail by ductile tearing (Figure 4.27c), contributing a small degree of toughening by crack tip convolution.

MIL-3 samples had an average fracture toughness of  $24.91 \text{ MPa}\sqrt{\text{m}}$ , continuing the trend of decreasing resistance to brittle fracture with increasing intermetallic phase content. Figures 4.27d-f show that even at  $6.4\mu\text{m}$  thick, the residual aluminum layer served as an adequate boundary to crack propagation between intermetallic layers. At that thickness it was

also able to prevent  $\text{Al}_3\text{Ti}$ -Al delamination fracture—large scale cracking took place predominantly at the  $\text{Al}_3\text{Ti}$ -Ti interfaces.

MIL-1 samples had an average fracture toughness of  $24.47 \text{ MPa}\sqrt{\text{m}}$ , which was slightly lower than MIL-3. Fracture in these samples showed much more  $\text{Al}_3\text{Ti}$ -Al interface cracking and delamination, indicating that the Al centerline reached a thickness and oxide content that no longer adequately reinforced the  $\text{Al}_3\text{Ti}$  bilayers. This failure mechanism ( $\text{Al}_3\text{Ti}$  bilayer centerline fracture, as seen in Figure 4.28b) was observed in other research [42, 52] to be a leading factor in the reduction of composite strength and fracture toughness. It is clear that the amount of residual aluminum in MIL-1 was insufficient to prevent this mechanism, so an optimal Al volume fraction would be greater than 1%. This corroborated the results from quasi-static compression tests. Figure 4.28a shows an increased percentage of  $\text{Al}_3\text{Ti}$  flat cleavage and bilayer centerline fracture, in addition to  $\text{Al}_3\text{Ti}$  monolayer centerline fracture (Figure 4.28c).

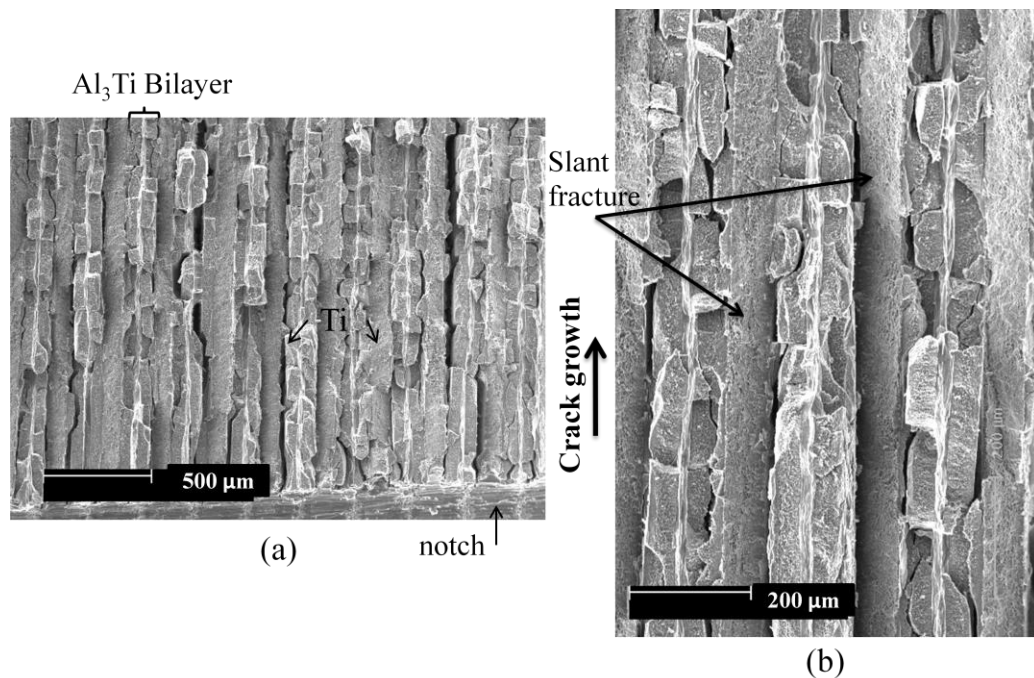


**Figure 4.26 – SEM micrographs of the fracture surfaces of MIL-16 in the crack divider orientation after quasi-static 4PB testing showing stair step  $\text{Al}_3\text{Ti}$  fracture and slanted Ti fracture.**

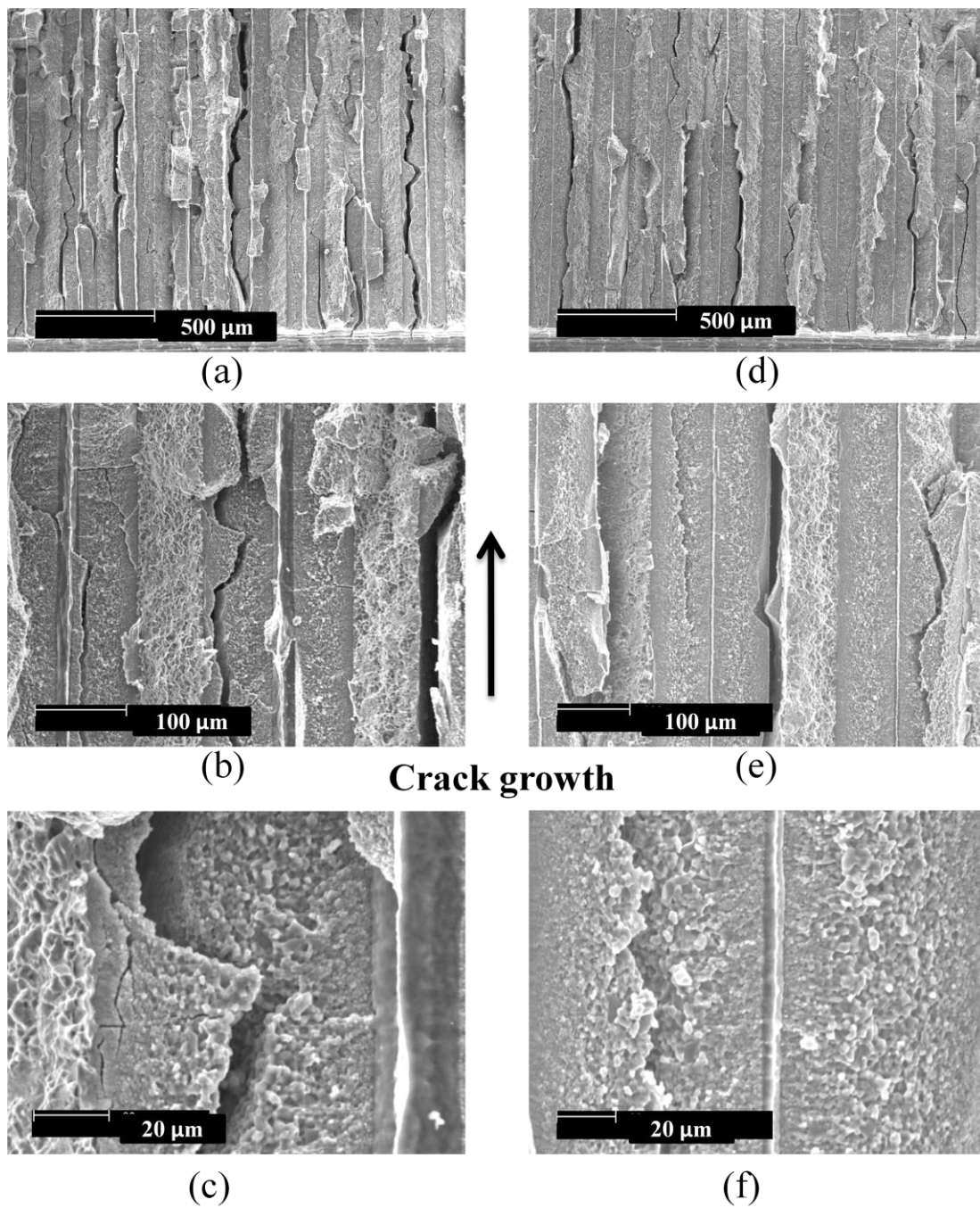


Figure 4.27 – SEM micrographs of the fracture surfaces of (a)-(c) MIL-11 and (d)-(f) MIL-3 in the crack divider orientation after quasi-static 4PB testing.

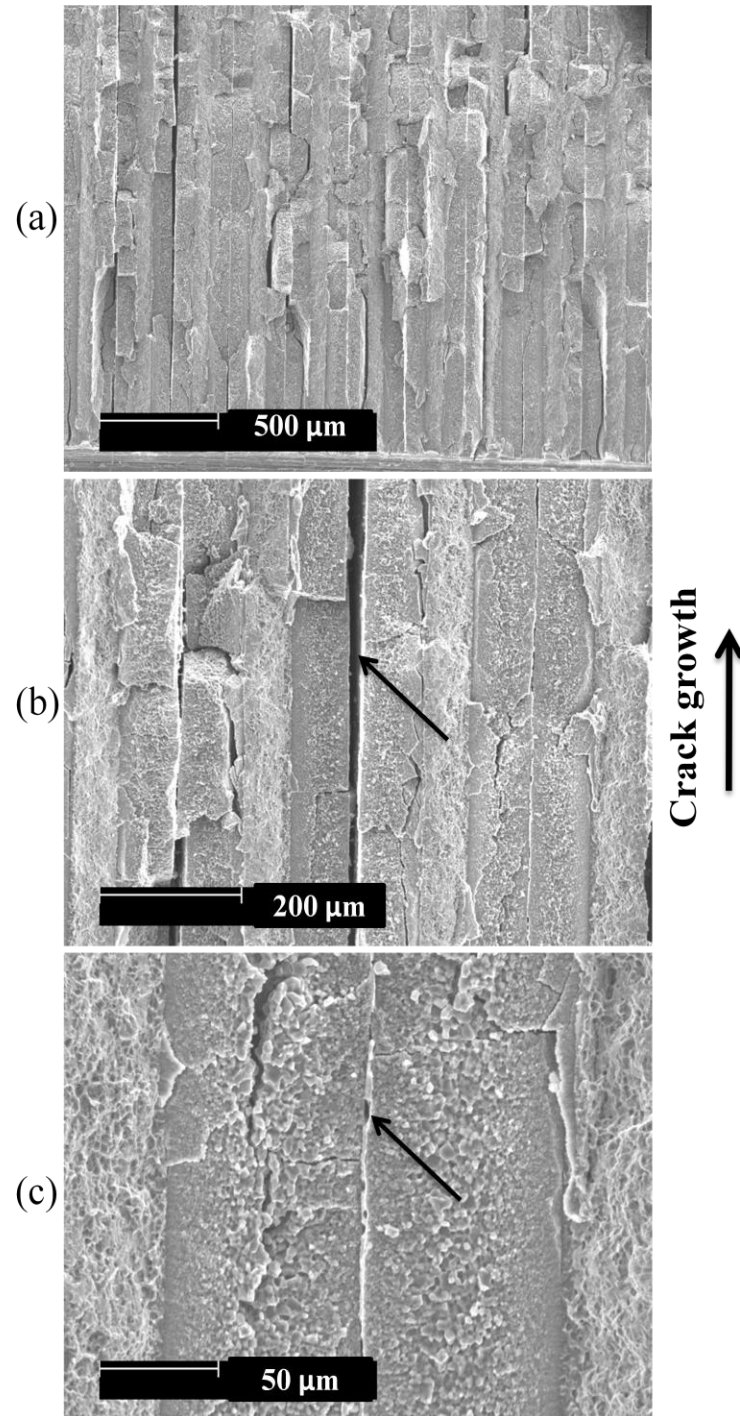


Figure 4.28 – SEM micrographs of the fracture MIL-1 in the crack divider orientation after quasi-static 4PB testing: (a) overview of fracture surface showing a higher percentage of  $\text{Al}_3\text{Ti}$  flat cleavage fracture; (b) magnified image showing  $\text{Al}_3\text{Ti}$  delamination from residual Al; (c) magnified image showing intermetallic centerline fracture, transverse cracking, and centerline cracking/delamination.



#### 4.2.2.2 Layers Perpendicular to the Applied Load

In quasi-static loading perpendicular to the layers (crack-arrester orientation), a 4PB fracture toughness test is more a measure of interlaminar bond strength than resistance to brittle fracture. As seen in Figure 4.29, no fracture parallel to the applied load occurred in any sample. The only cracks that formed traveled perpendicularly along an interface on either side of the notch, and then grew from those crack tips. MIL-48 and MIL-42 had microstructures that were still primarily ductile and so experienced a larger degree of compressive deformation after crack opening, hence the damage seen in Figure 4.29. Figure 4.30 is a compilation of representative (maximum) load-deflection curves from each specimen in the crack divider orientation.



**Figure 4.29 – Photograph of an arrester samples from each specimen after testing in quasi-static 4PB. Notice the lack of fracture in the notch direction.**



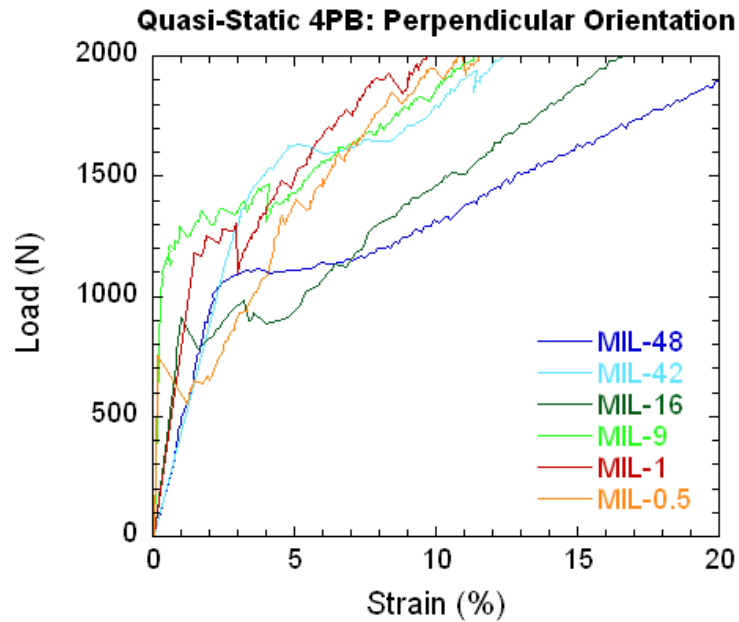


Figure 4.30 – Representative stress-strain curves of each specimen tested under quasi-static 4PB at 0.001/s with layers oriented perpendicular to the applied load.

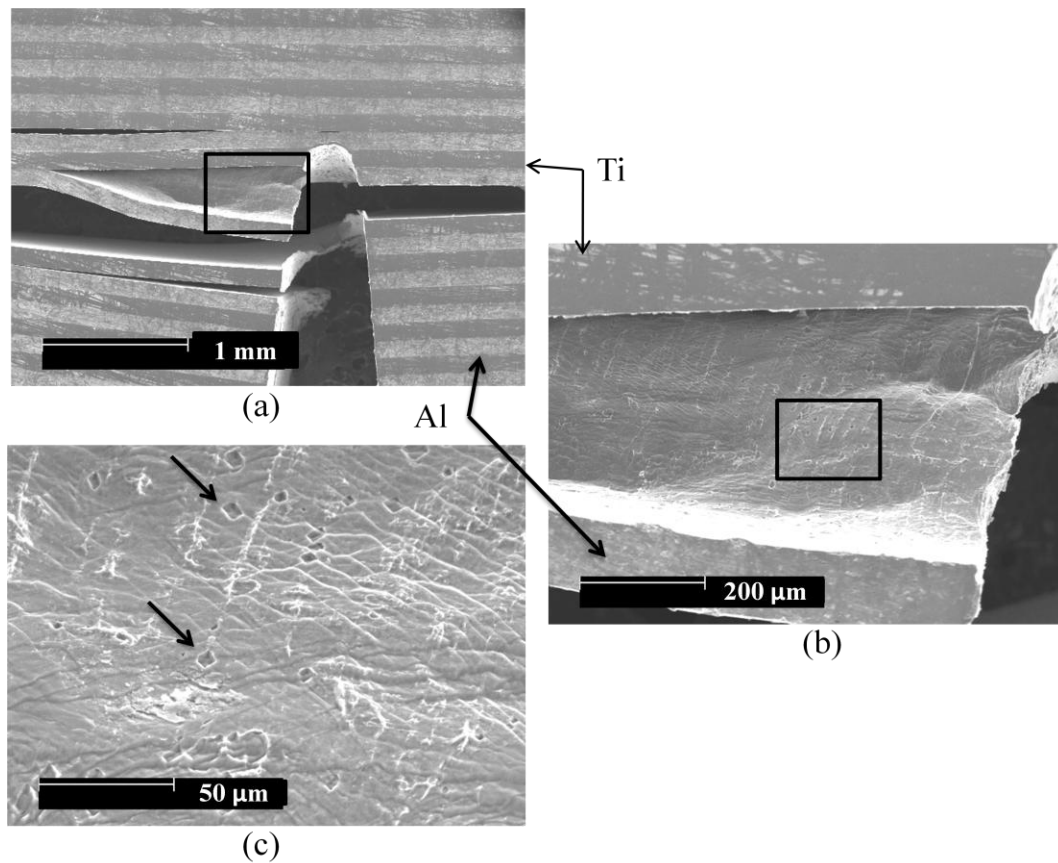
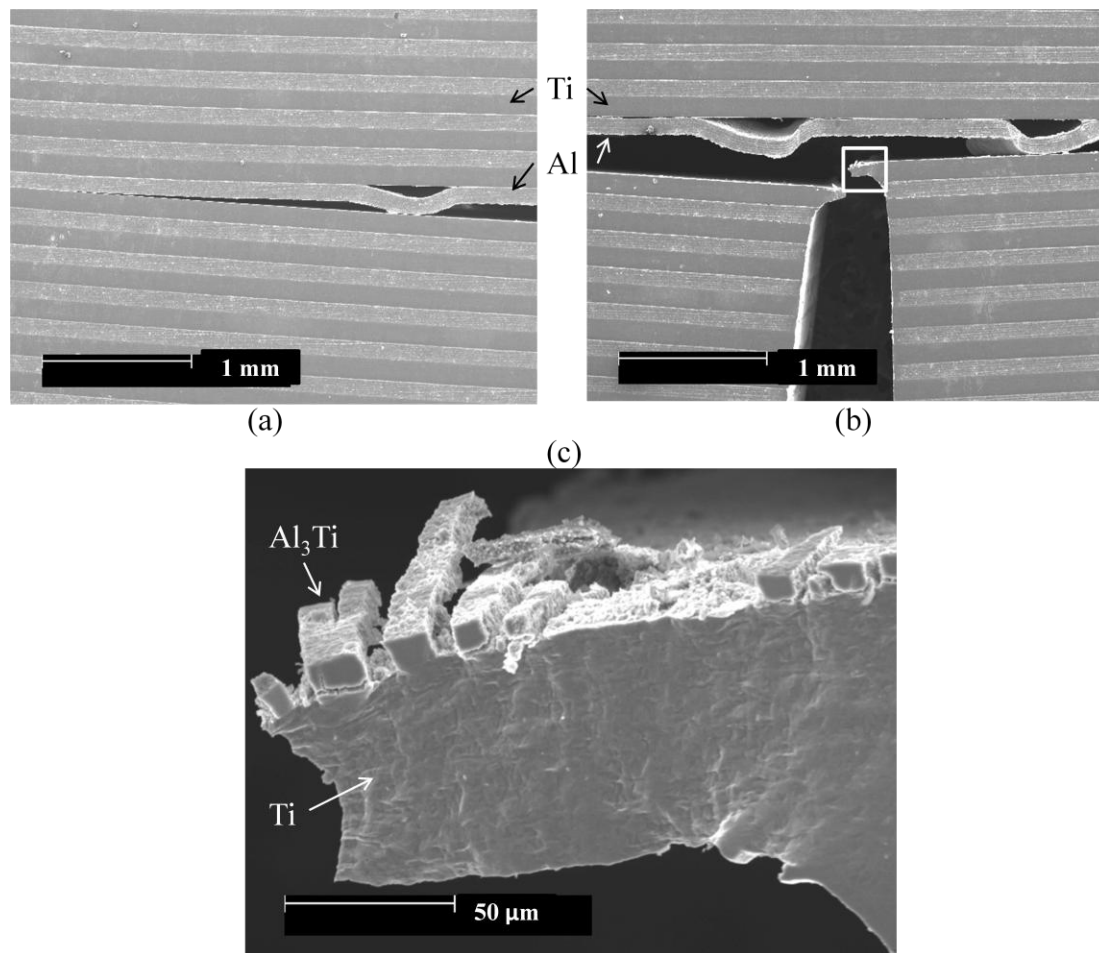


Figure 4.31 – SEM micrographs of MIL-48 arrester samples after quasi-static 4PB testing showing the surface texture of a delaminated layer of aluminum.



**Figure 4.32 – SEM micrographs of MIL-42 arrester samples after quasi-static 4PB testing showing: (a) ductile crack termination without significant microstructural damage; (b) Al delamination and plastic deformation, and (c) Ti necking and fracture at the notch nip.**

MIL-48 failed by delamination after significant crack opening displacement. With an average fracture toughness of only  $14.16 \text{MPa}\sqrt{\text{m}}$ , MIL-48 represented a local minimum toughness in both the arrester and divider orientations (see Figure 4.22) due to low interlaminar bond strength. The magnified image in Figure 4.31c shows the surface texture of a delaminated layer of aluminum. Arrows indicate points of adhesion that failed during loading, creating shear bands and the parallel striations more visible in 4.31b.

MIL-42 had an average fracture toughness  $K_{IC}$  of 20.14 MPa $\sqrt{m}$ . Figure 4.32b shows the Ti layer at the notch tip necking, tearing, and delaminating from the Al layer above it. Figure 4.32c is a magnified image, detailing the Ti layer necking and showing the same Al<sub>3</sub>Ti segmentation seen in other mechanical tests of MIL-42. The transverse delamination cracks from the notch tip arrested plastically without significant microstructural damage (Figure 4.32a).

MIL-16 showed a large decrease in average fracture toughness—10.76 MPa $\sqrt{m}$  compared to MIL-42 at 20.14MPa $\sqrt{m}$ . Samples of this specimen showed the first signs of significant microstructural damage above the notch (Figures 4.33a and 4.33b) and at the tips of the transverse delamination cracks (Figures 4.33c and 4.33d). What is seen more clearly by optical microscopy than by SEM is the formation of shear bands in the Ti layers. Cracking that initiated in an intermetallic layer created stress concentration points at the metal-intermetallic interfaces, which formed shear bands that propagated from the crack tip through the Ti (and Al as shown in Figure 4.33e) and into the next intermetallic layer. This lead to the formation of non-coplanar cracks formed in the adjacent intermetallic layers, which was also seen by Rawers *et. al.* [49] and Adharapurapu *et. al.* [43].

With a fracture toughness of 12.09 MPa $\sqrt{m}$ , MIL-11 samples showed slightly better performance than MIL-16, indicating the emergence of an advantageous failure mechanism. Comparing Figure 4.33c to Figure 4.34c, one sees that there was actually less vertical crack initiation in the Al<sub>3</sub>TI layers, and an increase in transverse Al<sub>3</sub>Ti cracking. The two are likely linked to the reduced thickness of the residual Al layer. Shear band formation can still be seen in Figure 4.34b and 4.34d, but it is much less exaggerated than in MIL-16 and MIL-3.

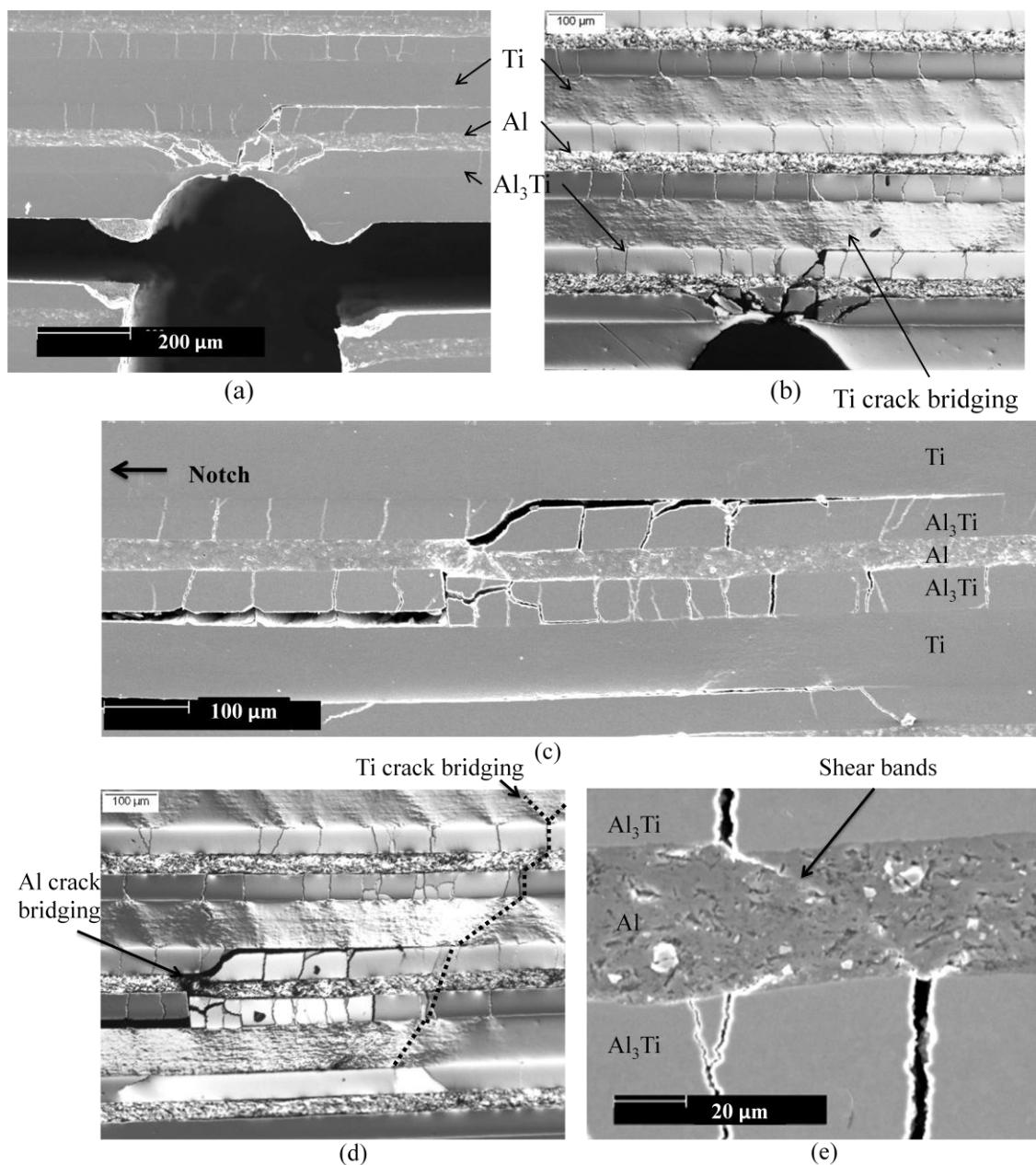


**Figure 4.33 – Failure of MIL-16 crack-arrester samples under quasi-static 4PB. (a) and (b) show vertical intermetallic cracking and shear band formation in the Ti layers. (c-e) show plastic deformation and Al and Ti crack tip bridging. (a, c, e) are SEM micrographs, and (b) and (d) were taken by an optical microscope.**

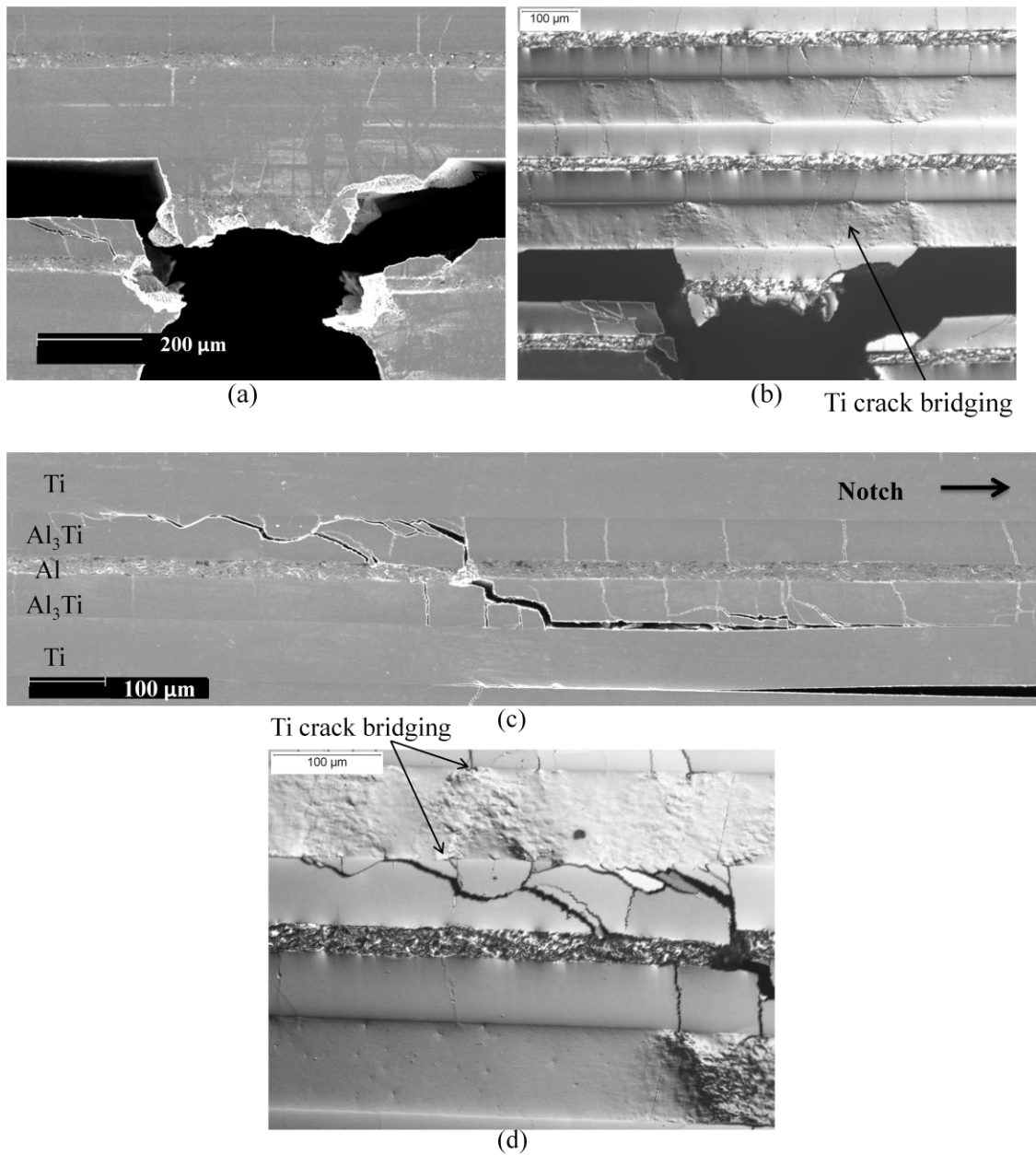


**Figure 4.34 – Failure of MIL-11 crack-arrester samples under quasi-static 4PB. (a) and (b) show vertical intermetallic cracking and shear band formation in the Ti layers. (c) and (d) show plastic deformation and Al and Ti crack bridging. (a) and (c) are SEM micrographs, and (b) and (d) were taken by an optical microscope.**

MIL-3 showed another increase in fracture toughness over MIL-16 and MIL-9. The flexural strength of MIL-3 ( $12.99\text{MPa}\sqrt{\text{m}}$ ) can be explained by the appearance of more extensive damage at the ends of the transverse delamination cracks (Figure 4.35a). With the propagation of an almost vertical crack, toughening mechanisms characteristic of a laminate structure (in the crack-arrester orientation) come into play: ductile ligament bridging and crack deflection. Figure 4.35b shows the torturous path of the  $\text{Al}_3\text{Ti}$  crack created by interactions with the ductile Ti layers, and to a lesser extent the Al layers. Figure 4.35c is a magnification of 4.35b showing ductile crack bridging via plastic deformation of the Ti layer. Also, the crack deflection (indicated in Figure 4.35b) caused by interface delamination contributed to the toughness of the sample. On a smaller scale, ductile ligament bridging by the Al centerline was also observed in vertical  $\text{Al}_3\text{Ti}$  cracks, indicating the residual Al was still beneficial at that volume fraction.

The average fracture toughness of MIL-1 was the lowest of all six specimens:  $8.88\text{MPa}\sqrt{\text{m}}$ . Figure 4.30 shows that MIL-1 reached its first peak load (the first delamination moment) at a very low strain. In stark contrast to MIL-3, which exhibited vertical fracture at the tip of the transverse delamination fracture, Figure 4.36 shows no major bridging cracks (see Figures 4.33c, 4.34c, and 4.35b). Instead, there was a significantly greater density of  $\text{Al}_3\text{Ti}$  cracks above the entire length of the transverse delamination crack (Figure 4.36a). Figure 4.36b shows a secondary delamination crack and transverse cracks in the intermetallic layers above the notch. Both inter- and intragranular cracking can be seen in Figure 4.36c, an SEM micrograph of a fractured intermetallic layer near the notch tip. MIL-1 showed the worst performance in both parallel and perpendicular 4PB tests, indicating that the residual Al at the intermetallic centerline was no longer adding to the fracture toughness of the composite. Figure 4.37 is a collection of optical micrographs showing the failure evolution MIL-16, MIL-11, MIL-3, and MIL-1 crack-arrester samples. As the residual aluminum centerline thinned

from MIL-16 to MIL-3, both microstructural damage and fracture toughness increased. MIL-1 shows an obvious break from that pattern, evidenced by its low fracture toughness.

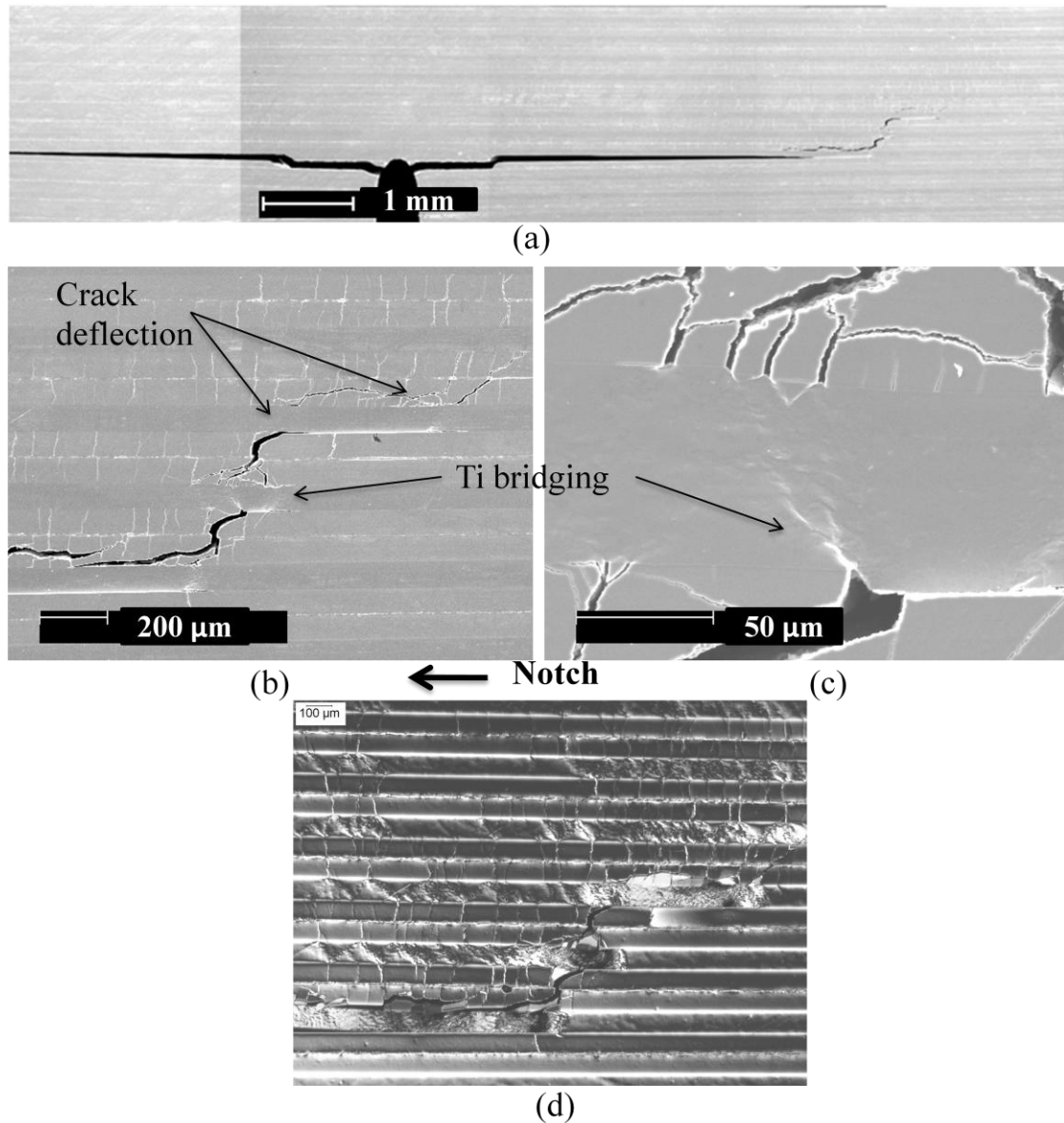


**Figure 4.35 – Failure of MIL-3 crack-arrester samples under quasi-static 4PB. (a) Stitched panorama of the transverse delamination that propagated from the crack tip and (b, c) cracking and arresting at the tip. (d) Optical micrograph of the region in (b) showing shear band deformation and crack bridging by Ti layers.**

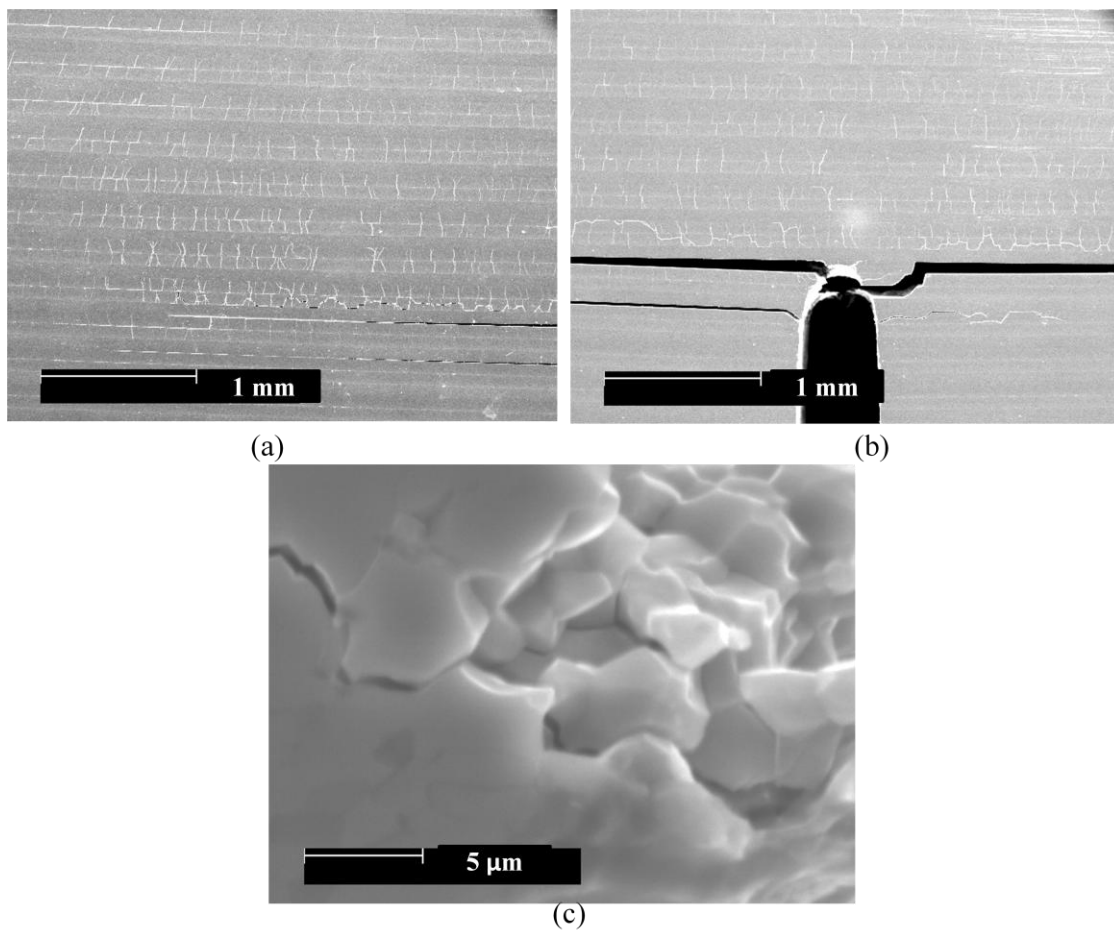


**Figure 4.36 – Failure of MIL-1 crack-arrester samples under quasi-static 4PB. SEM micrographs of: (a) significant  $\text{Al}_3\text{Ti}$  cracking without propagation of a single fracture; (b) delamination and fracture at the notch tip; (c) inter- and intragranular fracture of  $\text{Al}_3\text{Ti}$  grains near the crack tip.**



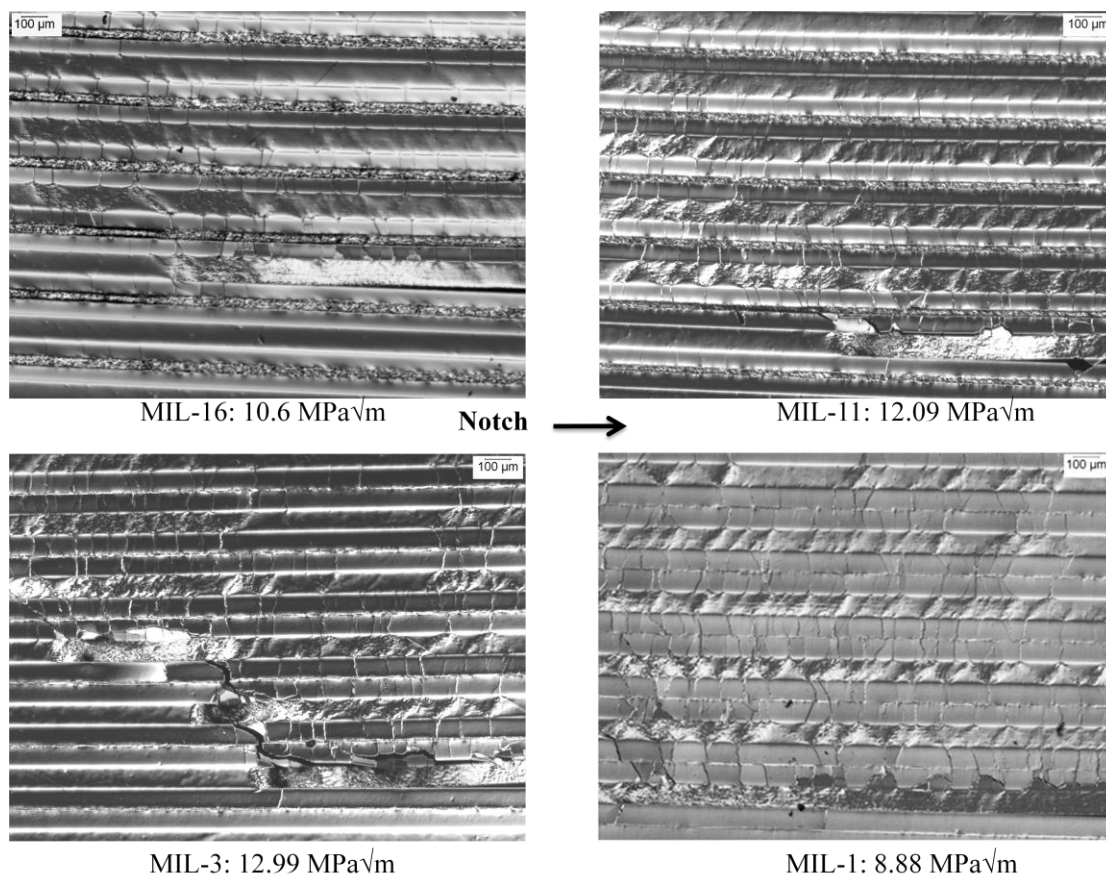


**Figure 4.37 – Optical micrographs showing the failure evolution of four crack-arrester samples after quasi-static 4PB. Notice the increasing microstructural damage from MIL-16 to MIL-3 as the residual Al content decreases.**

### 4.2.3 High Strain-Rate Compression Testing

High strain-rate compression tests were performed on small rectangular samples at strain rates of  $\sim 10^3/s$ . Both extreme layer orientations were tested for each specimen. A brief summary of the results is presented in Table 4.7. Graphical representation of the data is presented in Figure 4.7, showing the relationship between residual aluminum volume fraction and yield stress. Comparing Figure 4.38 to Figure 4.7, the trends observed in the parallel and perpendicular orientations are very similar to those of quasi-static compression testing. One of the differences is the across-the-board increase in yield stress, which is typical when comparing low and high strain-rate characteristics. However, the most immediately obvious difference is the abnormal performance of MIL-3. MIL-3 did not show anomalous behavior in any prior tests, and may be explained by a systematic error of the testing apparatus or a novel response of the specimen to dynamic loading. As a note, all dynamically loaded compression samples were cold-mounted and polished after testing.

**Table 4.7 - Summary of yield stresses observed in dynamic compression testing.**

Sample ID	Al Volume Fraction	Yield Stress (MPa)	
		Parallel	Perpendicular
MIL-48	0.481	497.3	586.7
MIL-42	0.419	664.9	631.8
MIL-16	0.157	776.6	893.3
MIL-11	0.109	1085.9	953.1
MIL-3	0.027	598.6	711.2
MIL-1	0.009	957.6	1053.0

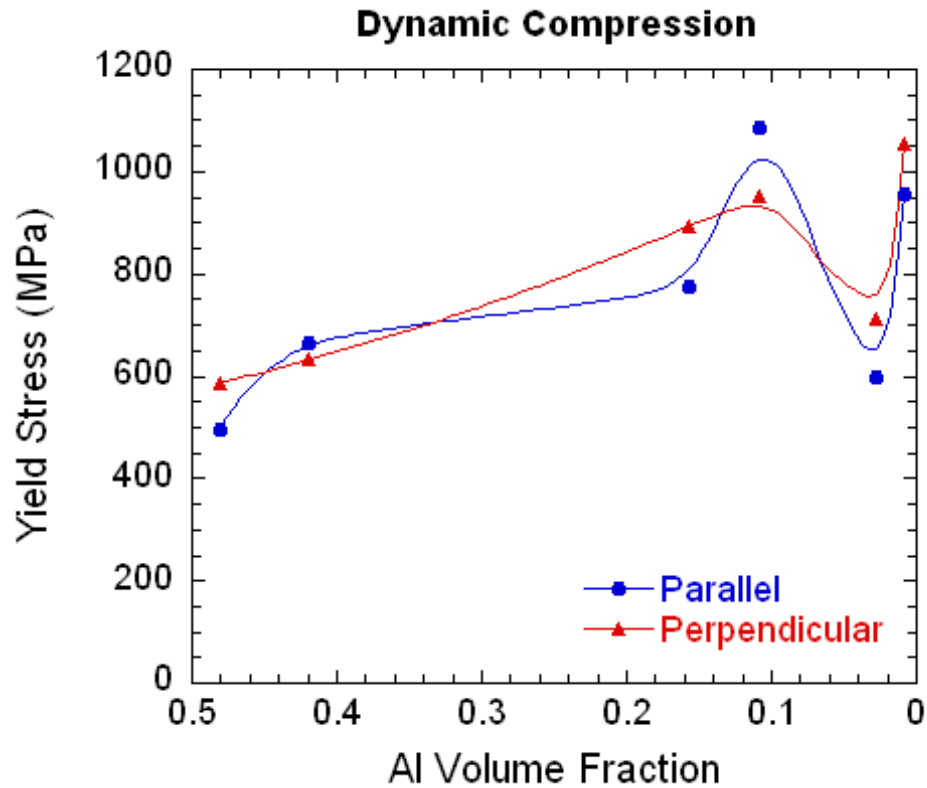


**Figure 4.38 – Affect of residual aluminum volume fraction on compressive yield stress in dynamic testing of parallel and perpendicular loading orientations. Compare to Figure 4.7**

#### 4.2.3.1 Layers Parallel to the Applied Load

When loaded parallel to their layers, results showed many similarities with quasi-static compression tests. Comparing Figure 4.39 to Figure 4.8, MIL-48 and MIL-42 behaved very similarly, except MIL-16 and MIL-11 showed a degree of plasticity prior to failure closer to that of MIL-3 and MIL-1. Otherwise, the failure strain range in both tests was almost the same.

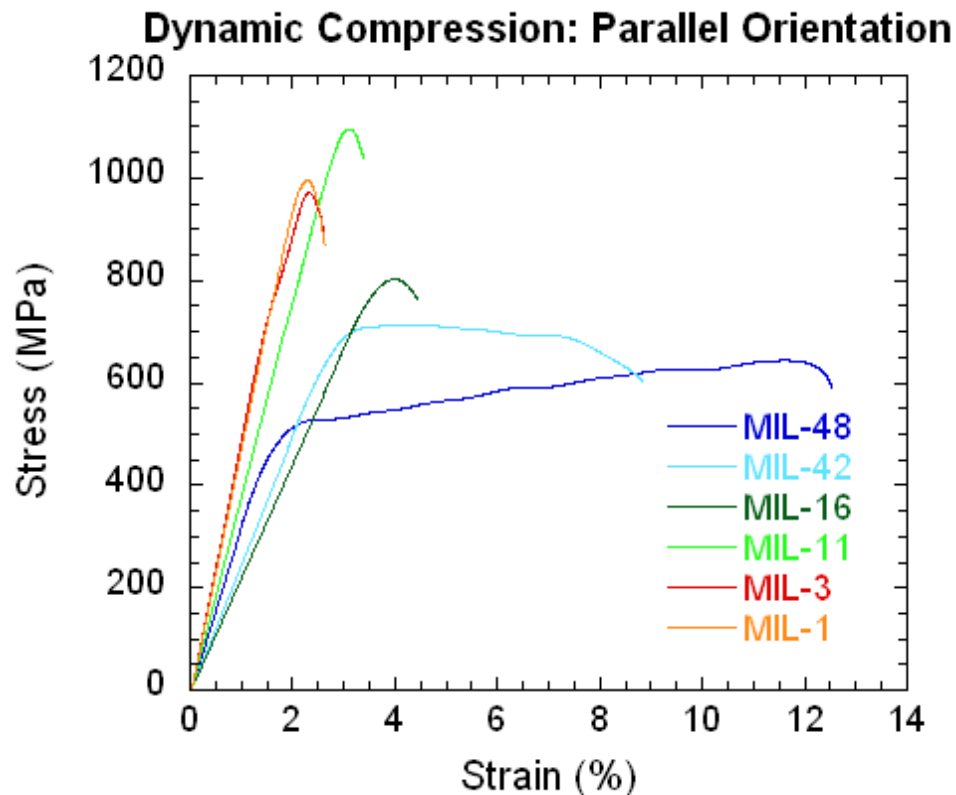


**Figure 4.39 – Representative stress-strain curves of each specimen tested under dynamic compression at 1000/s with layers oriented parallel to the applied load.**

MIL-48 had an average yield stress of 497.3 MPa, which was noticeably higher than its yield strength in quasi-static loading. Failure was marked by buckling and large scale delamination, as shown in Figure 4.40. In the SEM micrograph shown, the light layers are Ti and the dark layers are Al.  $Al_3Ti$  played no role in the failure of this specimen, nor was there any evidence of shear fracture or crack initiation. As seen in Figure 4.39, MIL-48 experienced a significant degree of plasticity prior to failure.

MIL-42 exhibited very similar plastic deformation prior to failure, but the  $Al_3Ti$  layers played a much more important role. All the delamination in the sample shown in Figure 4.41 occurred via intermetallic centerline fracture. The average yield stress of MIL-42 samples

was 664.9 MPa, which was almost exactly the increase over MIL-48 seen in quasi-static testing despite the differences in failure mechanisms.

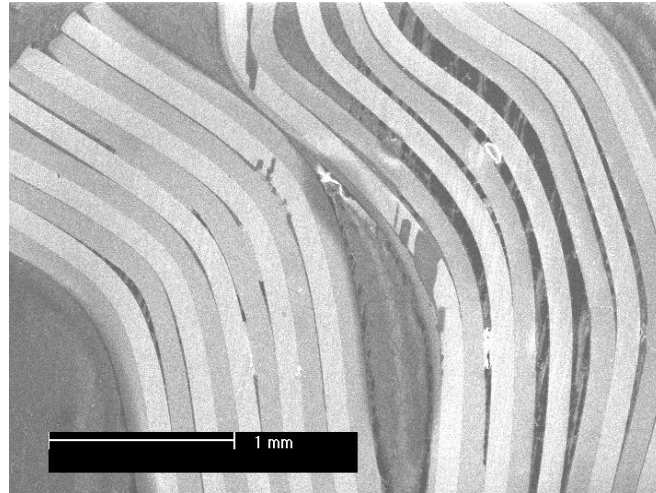


**Figure 4.40 – SEM micrograph of MIL-48 cold-mounted and polished after dynamic compression showing large scale delamination and buckling without shear fracture.**

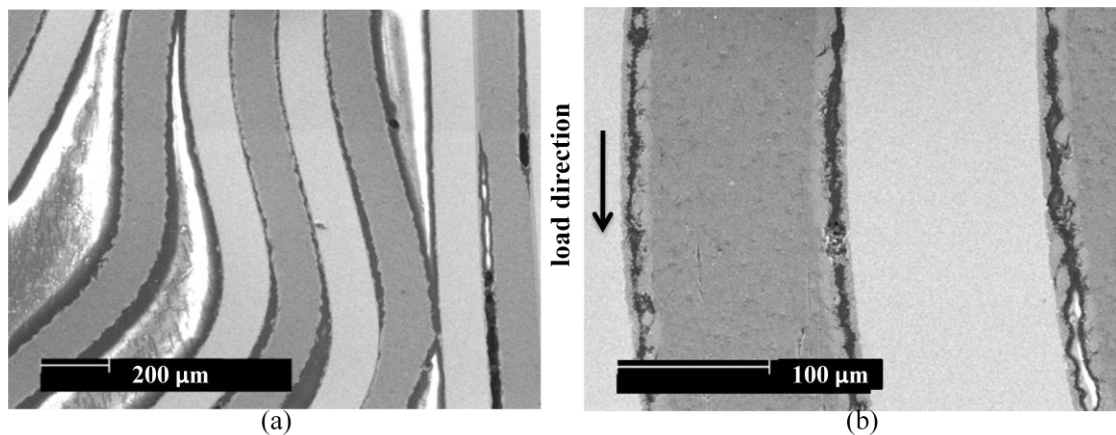


**Figure 4.41 – SEM micrographs of MIL-42 cold-mounted and polished after dynamic compression showing (a) large scale delamination, buckling, and (b)  $Al_3Ti$  centerline fracture. Light layers are Ti, dark layers are Al.**

MIL-16 did not show the same marked increase in yield strength over MIL-42 that it did in quasi-static compression. In fact, MIL-16 samples performed better in quasi-static tests, where the average yield stress was 841.5MPa compared to 776.6MPa in dynamic. Figures 4.42a and 4.42b show that the reinforcing Al layers kept their neighboring intermetallic layers intact, and delamination fracture occurred only at the Ti-Al<sub>3</sub>Ti interfaces. This bilayer behavior also appeared in quasi-static compression of MIL-16, as seen when comparing Figure 4.42 and Figure 4.11. Intermetallic bilayers failed by transverse cracking and shear fracture.

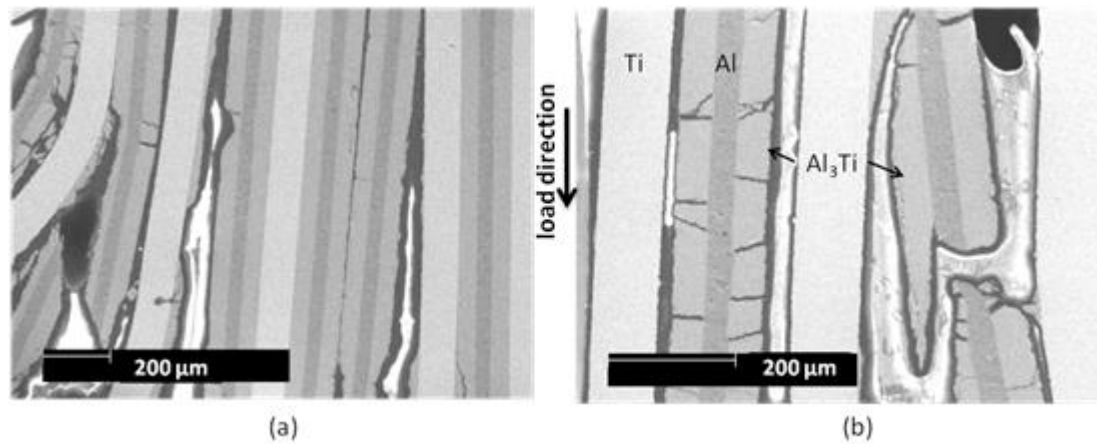


**Figure 4.42 – SEM micrographs of MIL-16 cold-mounted and polished after dynamic compression showing (a) delamination cracking, buckling, and (b) Al<sub>3</sub>Ti centerline fracture.**

MIL-11 had the highest average yield stress in both quasi-static and dynamic tested, positively reinforcing the assumption that there is an ideal residual Al volume fraction near 11%. The average yield stress was 1085.9 MPa, compared to 999.2 MPa at low strain-rate. Failure was characterized by large scale fracture of intermetallic layers between buckled layers of Ti (Figures 4.43a and 4.43b). However, unlike in MIL-16 samples, no Al-Al<sub>3</sub>Ti delamination occurred in regions of massive deformation. Figure 4.43c shows delamination fracture at Ti-Al<sub>3</sub>Ti interfaces and Al<sub>3</sub>Ti single-layer centerline fracture.

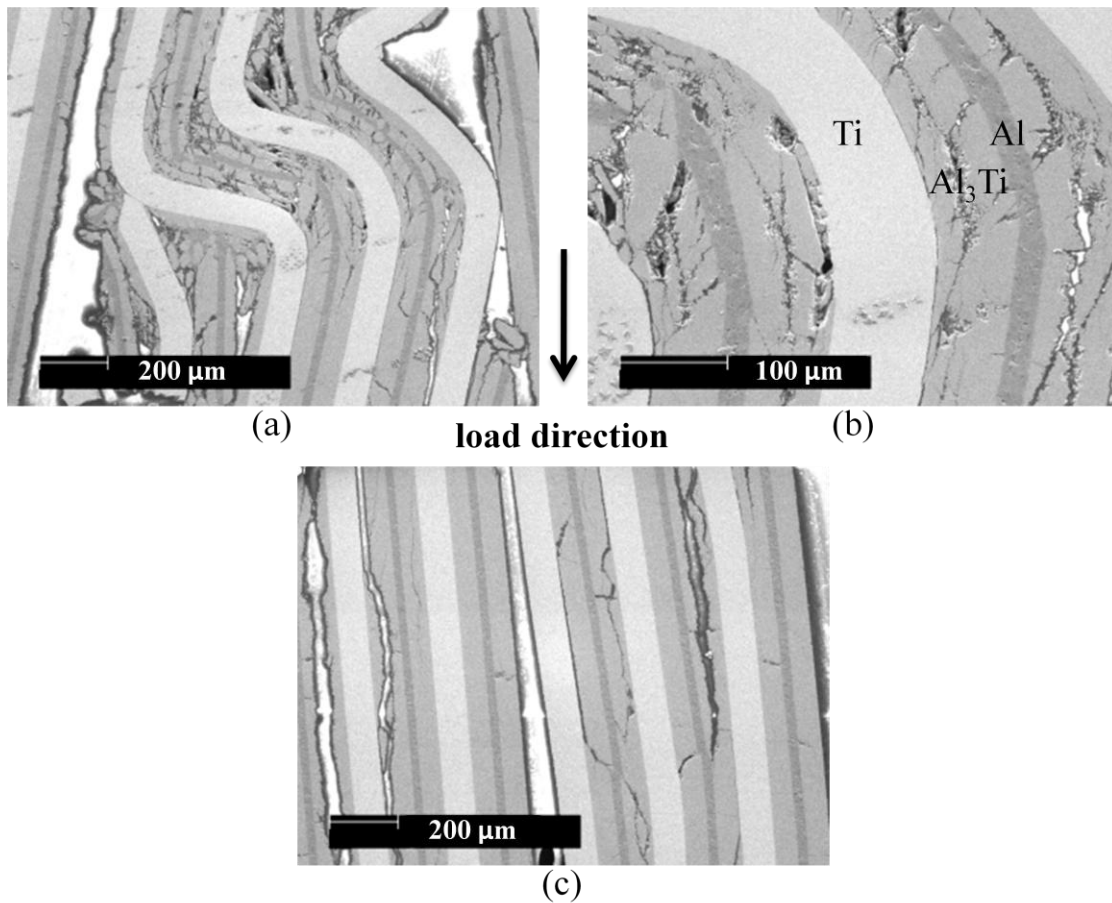


Figure 4.43 – SEM micrographs of MIL-11 cold-mounted and polished after dynamic compression showing (a, b) intermetallic layer reinforcement by plastic deformation of Ti layers, and (c) Al<sub>3</sub>Ti centerline fracture.

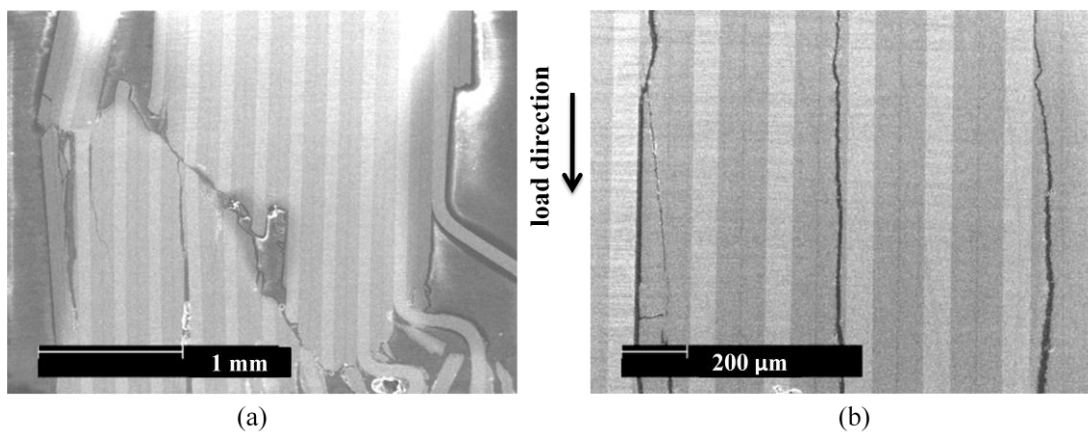
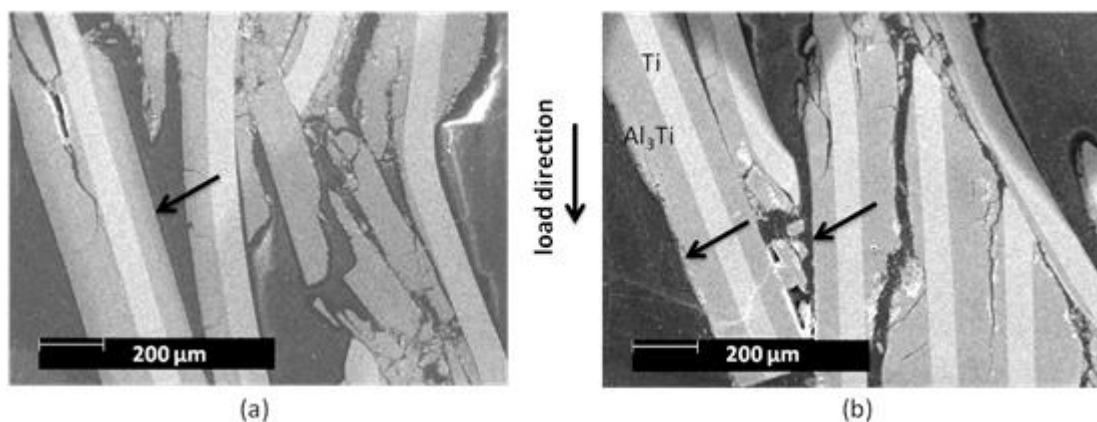


Figure 4.44 – SEM micrographs of MIL-3 cold-mounted and polished after dynamic compression showing (a) shear fracture, buckling, and (b) Al<sub>3</sub>Ti centerline fracture.

MIL-3 represented an anomalous, singular divergence from the trend that had agreed with quasi-static test results for all the previous specimens. Two averages emerged within the data for MIL-3: 598.6 and 963.9 MPa. Even though twice as many samples were tested compared to other specimens, the data still pointed to the lower value (6 samples showed the low yield stress and 3 showed the high one). The reason for the two distinct averages lies in the failure mechanisms of MIL-3. All the samples that yielded near 600 MPa failed by delamination and  $\text{Al}_3\text{Ti}$  single-layer centerline fracture only, as in Figure 4.45b. Yield stresses near 1 GPa were seen in samples that had the added failure mechanism of a-type shear fracture, as in Figure 4.45a.

MIL-1 samples were all very nearly obliterated. The average yield stress was 957.6 MPa for MIL-1, which showed the only case in dynamic compression testing of failure by delamination fracture at the intermetallic centerline. Fracture at the [bilayer] centerline was also observed in quasi-static compression tests of MIL-1 (though to a far lesser degree), but did not significantly decrease the strength of the sample.



**Figure 4.45 – (a) and (b) are SEM micrographs of MIL-1 cold-mounted and polished after dynamic compression showing failure by delamination at the intermetallic centerline (arrows).**



#### 4.2.3.2 Layers Perpendicular to the Applied Load

Figure 4.46 is a compilation of representative stress-strain curves from each MIL specimen with layers oriented perpendicular to the loading direction. Samples from every specimen showed some degree of plastic behavior after yield, while toughness decreased with Al volume fraction. In this orientation, specimen yield stress increased almost linearly from MIL-48 to MIL-1. MIL-3 was the only outlier, showing a reduced yield stress not in keeping with the trend. Behavior was more uniform among similar specimens compared to performance in parallel loading (see Figure 4.8); stress-strain curves show a certain degree of grouping by residual Al content.

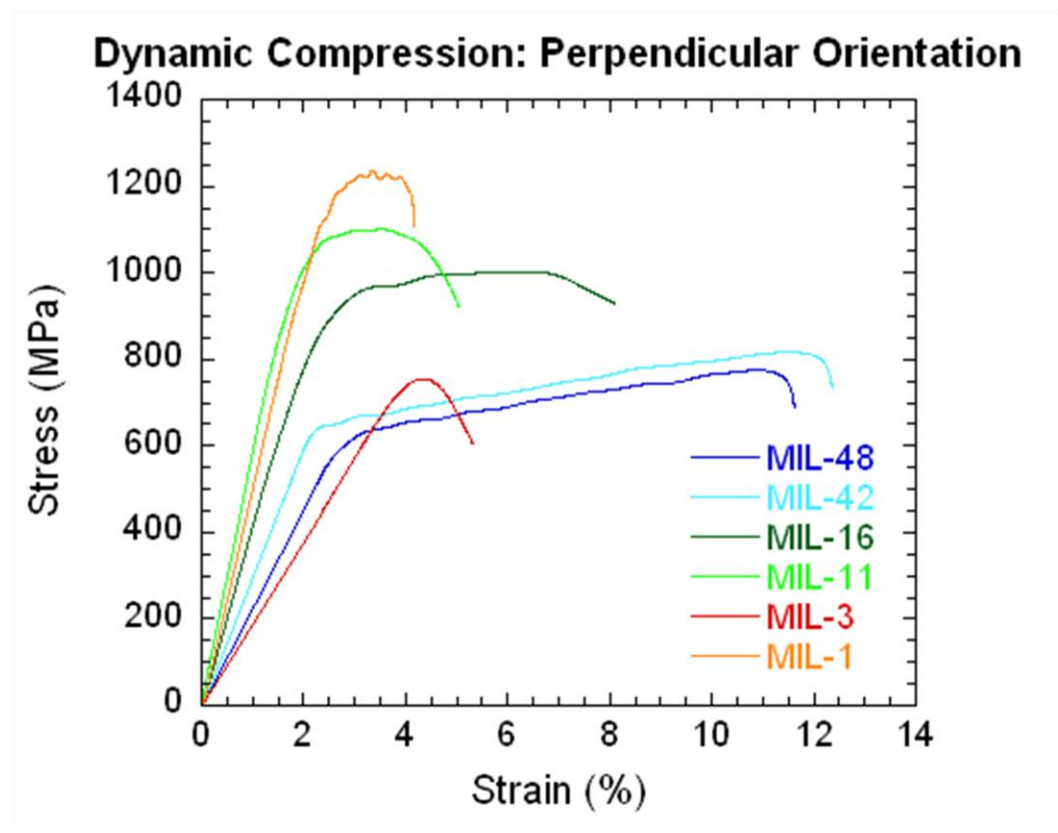


Figure 4.46 – Representative stress-strain curves of each specimen tested under dynamic compression at 1000/s with layers oriented perpendicular to the applied load.

MIL-48 and MIL-42 behaved very similarly in dynamic compression. The average yield stress of MIL-48 was 586.7 MPa, and for MIL-42  $\sigma_y = 631.8$  MPa—not a very significant difference considering a standard deviation of roughly 20 MPa. MIL-48 failed by macrostructural deformation and Al expulsion, as seen in Figure 4.47a, with no microstructural cracking or shear fracture (Figure 4.47b). MIL-42 showed similar failure characteristics, with the addition of intermetallic layer cracking. Figure 4.48b is an SEM micrograph of a single Al layer with bordering intermetallic layers. There is no evidence of shear band growth through the Al layer with renucleation at the adjacent interface. Due to the lack of shear deformation, stress buildup in the  $Al_3Ti$  layers resulted in the high crack density shown.

As in quasi-static compression testing, MIL-16 showed a large increase in strength over MIL-42. The higher strength can be attributed to the introduction of shear fracture as a failure mechanism, made possible by the increase in intermetallic content. For MIL-16,  $\sigma_y = 893.3$  MPa. Comparing Figure 4.49 to Figure 4.19, it is clear that deformation was very similar between the high strain-rate and quasi-statically tested samples.

MIL-11's performance did not differ very much from that of MIL-16 or from its quasi-static results. There are very few differences between the SEM micrographs in Figures 4.50, 4.49, 4.20, and 4.19, indicating that when loaded perpendicular to their layers the strength of the composite was not significantly affected by the decrease in Al volume content from 16% to 11%. In all cases the thickness of the residual Al layers served to prevent the propagation of large cracks from one intermetallic layer to the next through the centerline. The yield stress of MIL-11 was 953.1 MPa, which was an increase of 6.7% over MIL-16.

The average yield stress of MIL-3 samples was 711.2 MPa, which represented a significant deviation from the trend established by the previous 4 specimens (and MIL-1). With similar performance in dynamic compression of parallel samples (Figure 4.38), the

reason is most likely microstructural in nature. Figure 4.51 shows a-type shear fracture surrounded by almost no intermetallic cracking. Due to the instability and unreliability of MIL-3 in dynamic compression (in both orientations), it can be concluded that Al volume content near 3% is disadvantageous.

MIL-1, which had even less residual aluminum than MIL-3, did not show unpredicted results in dynamic compression. With an average yield stress of 1053 MPa, this specimen behaved in accordance with its quasi-static test results. Figure 4.52a shows double-shear failure, which occurred in several of MIL-1 samples. Compared to MIL-3, samples of this specimen exhibited a moderately higher degree of  $\text{Al}_3\text{Ti}$  vertical cracking, though a majority of the cracking was transverse and along the centerline (Figures 4.52b and 4.52c). The transverse intermetallic centerline fracture seen in Figure 4.52c did not have a significant negative effect on the yield stress of the sample.

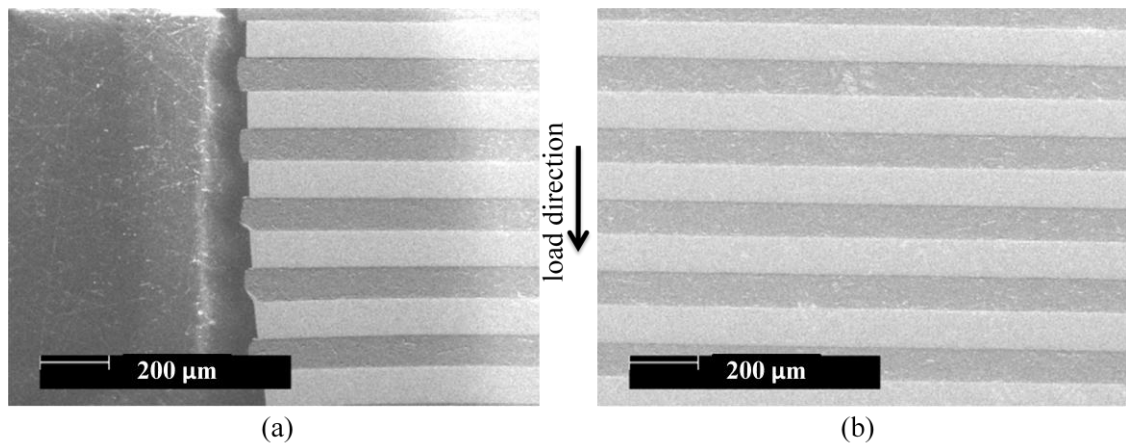


**Figure 4.47 - SEM micrographs of MIL-48 cold-mounted and polished after dynamic compression showing**

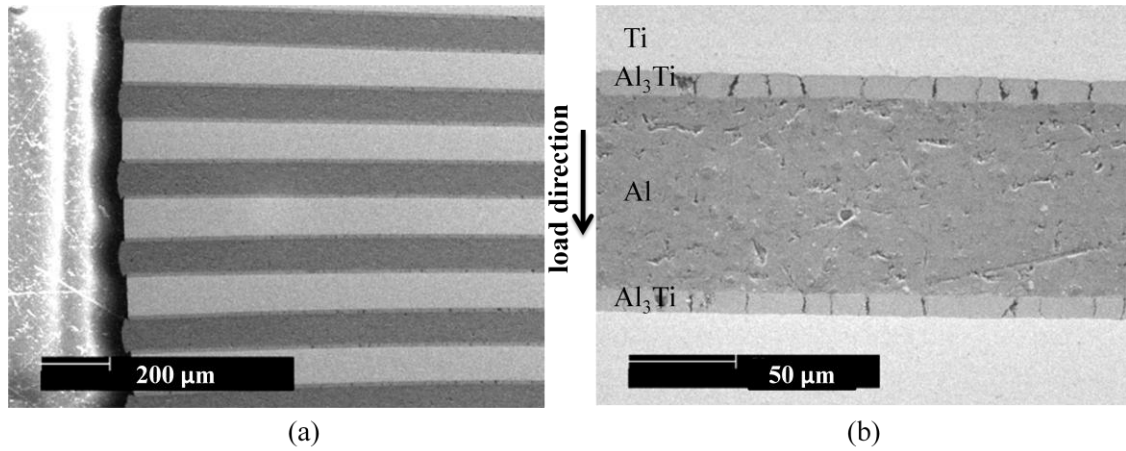


Figure 4.48 - SEM micrographs of MIL-42 cold-mounted and polished after dynamic compression showing

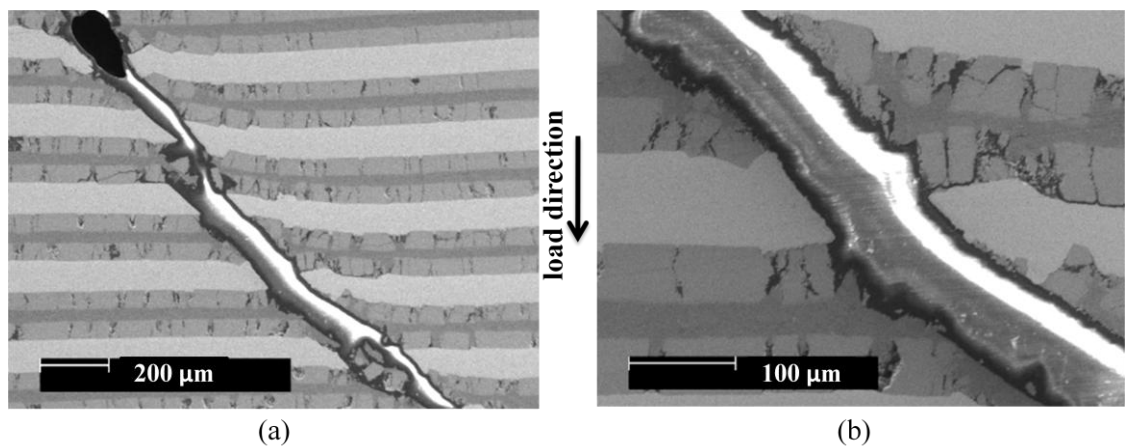


Figure 4.49 - SEM micrographs of MIL-16 cold-mounted and polished after dynamic compression showing (a) shear fracture and (b) and magnified image of intermetallic cracking and Ti shear deformation.

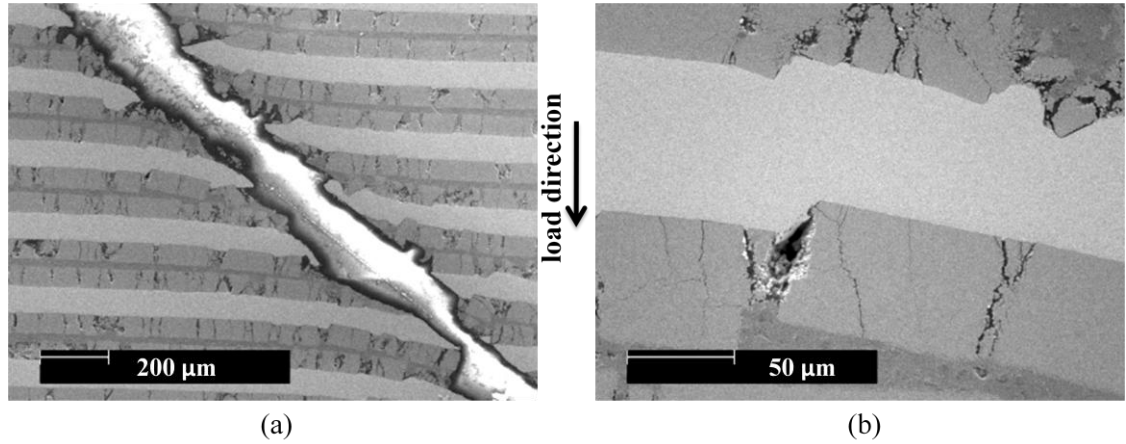


Figure 4.50 - SEM micrographs of MIL-11 cold-mounted and polished after dynamic compression showing (a) shear fracture and (b) magnified image of intermetallic cracking and Ti shear deformation.

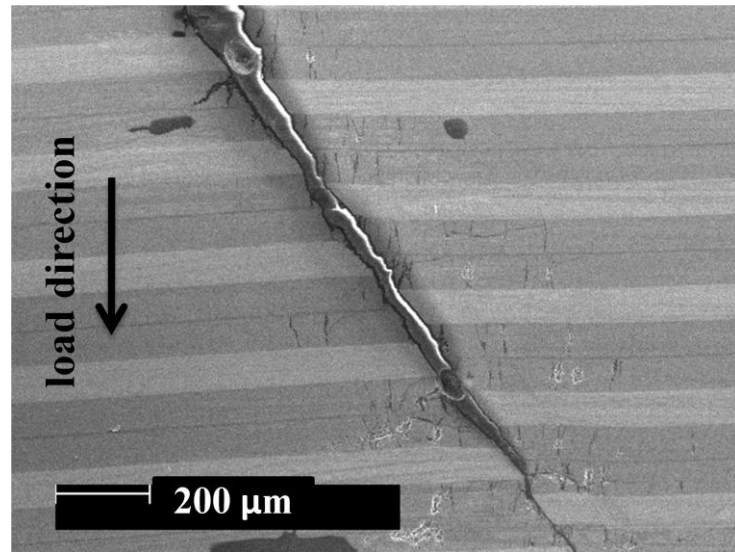
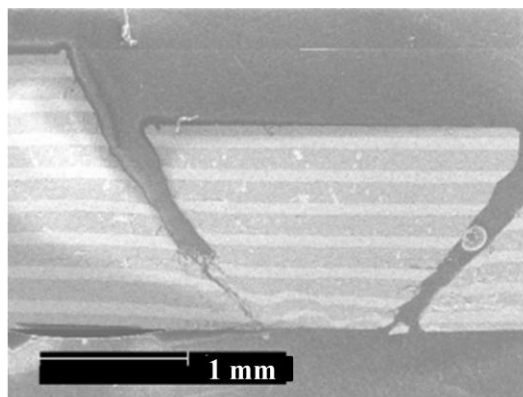
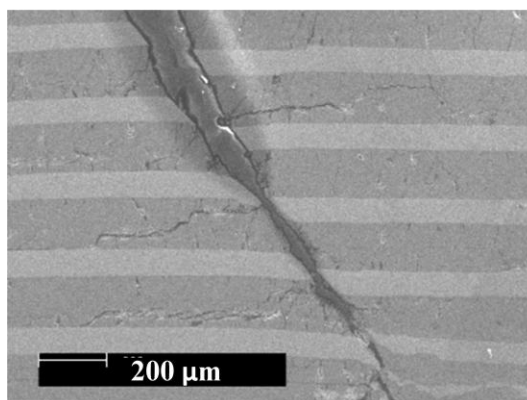


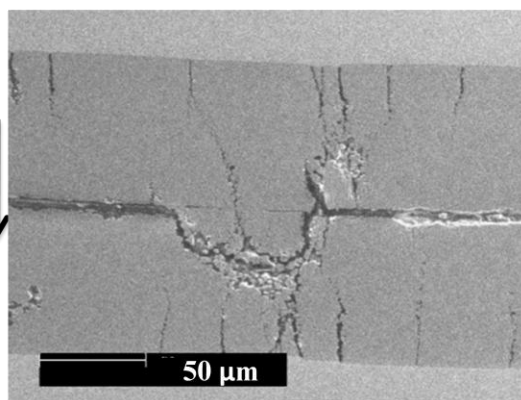
Figure 4.51 - SEM micrograph of MIL-3 cold-mounted and polished after dynamic compression showing a lack of intermetallic cracking.



(a)



(b)



(c)

**Figure 4.52 - SEM micrographs of MIL-1 cold-mounted and polished after dynamic compression showing**

#### 4.2.4 High Strain-Rate Four Point Bend Testing

Four point bend (4PB) tests were performed on small rectangular beams (see Figures 3.3 and 3.4.5). Both extreme layer orientations were tested for each specimen. A brief summary of the results is presented in Table 4.8. Graphical representation of the data is presented in Figure 4.53, showing the relationship between residual Al content and fracture toughness in the parallel and perpendicular orientations. In the parallel orientation, the results are shown for both fracture time determination methods: high-speed camera and strain gage. Though the toughness values given by the strain gage method (“Parallel SG” in Figure 4.53) are consistently lower, the trend is almost identical. Both parallel sample curves show increased performance in MIL-48 and MIL-11 samples. The curve representing perpendicular samples is very similar to the curve seen in quasi-static 4PB (see Figure 4.22).

**Table 4.8 - Summary of fracture toughness values observed in dynamic 4PB testing.**

Specimen	Al Volume Fraction	$K_{IC}$ (MPa $\sqrt{m}$ )	
		Parallel	Perpendicular
MIL-48	0.481	49.08	17.58
MIL-42	0.419	49.69	27.06
MIL-16	0.157	43.28	21.17
MIL-11	0.109	51.76	24.97
MIL-3	0.027	41.10	25.88
MIL-1	0.009	40.69	24.51

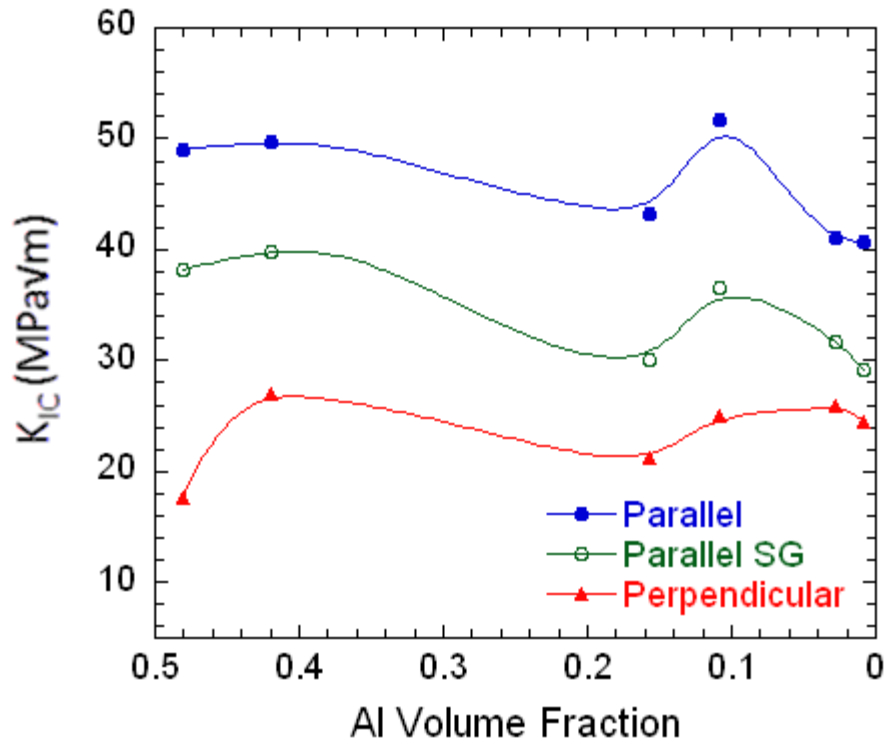


**Figure 4.53 – Affect of residual aluminum volume fraction on fracture toughness  $K_{IC}$  in parallel and perpendicular loading orientations under dynamic 4PB. The parallel orientation curves generated by the high-speed camera and strain gage methods show almost identical trends.**

#### 4.2.4.1 Layers Parallel to the Applied Load

As in quasi-static 4PB testing, no primary crack propagated from the tip of the notch parallel to the applied load in any sample of any specimen. Results from the samples fitted with a strain gage positively confirmed the accuracy of the methodology described in Section 3.3.4 (in which a high-speed camera was used to monitor and accurately time the critical crack initiation moment). As seen in Figure 4.53, the average fracture toughness values calculated generally agree with quasi-static findings, barring the behavior of MIL-48 and MIL-11. Figure 5.54 shows that, typically, crack initiation in each specimen was between 30 and 50 $\mu$ s.



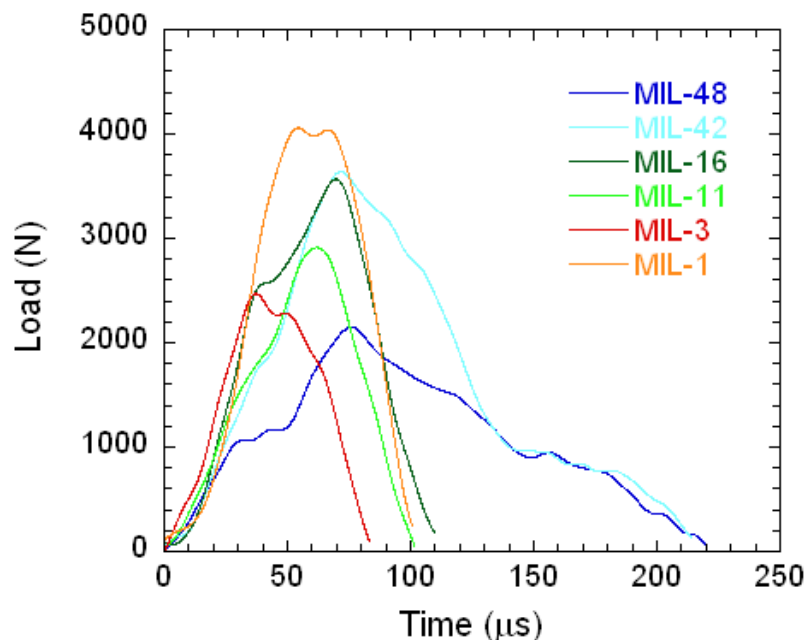


**Figure 4.54 – Representative load-time curves of each specimen tested under high strain-rate 4PB with layers oriented parallel to the applied load.**

MIL-48 samples had an average fracture toughness,  $K_{IC}$ , of  $49.08 \text{ MPa}\sqrt{\text{m}}$ , which was more than twice that of its fracture toughness in quasi-static 4PB— $20.86 \text{ MPa}\sqrt{\text{m}}$  (Table 4.6). This dramatic increase may be attributed to a lack of time given to debonding and layer separation resulting from the high strain-rates of the deformation process, even though the fracture surfaces of the dynamic samples (Figure 4.55) and quasi-static samples (Figure 4.24) are very similar. Figure 4.55b shows Ti slant fracture influenced by points of adhesion between Ti and Al that did not delaminate. This failure characteristic was also seen in quasi-statically tested samples. Figure 4.55c is an SEM micrograph of a de-bonded region in which the thin intermetallic layer remained unbroken on the Ti layer.

MIL-42 represented a small increase in fracture toughness over MIL-48, with  $K_{IC} = 49.69 \text{ MPa}\sqrt{\text{m}}$ . The ubiquitous intermetallic segmentation visible in Figure 4.56 was very similar to what was seen in quasi-static tests (Figure 4.25), though the dynamically tested

samples experienced a higher degree of ply separation. Figure 4.56b is an SEM micrograph showing  $\text{Al}_3\text{Ti}$  bonded to the Al and Ti layers in an anomalous, transverse out-of-plane pattern. Figure 4.56c is a magnified image of a necked and torn aluminum layer with embedded intermetallic fragments.

Fracture toughness decreased to  $43.28 \text{ MPa}\sqrt{\text{m}}$  in MIL-16 samples. This can be attributed to the increase in intermetallic content and the presence of extensive Ti- $\text{Al}_3\text{Ti}$  interface fracture (see Figure 4.57a). Almost identical failure mechanisms were observed in quasi-static loading (see Figure 4.26). Crack front convolution caused by the large difference in elasticity between ductile Al centerline and bonded intermetallic layers prevented the flat cleavage fracture characteristic of brittle failure, and instead lead to the formation of the stair-step fracture seen in Figure 4.57b. This type of fracture is distinguished by non-coplanar transverse intermetallic cracking blunted and redirected by the thick reinforcing Al layer.

MIL-11 showed superior performance in dynamic 4PB that it did not show under quasi-static loading.  $K_{\text{IC}}$  for MIL-11 was  $51.76 \text{ MPa}\sqrt{\text{m}}$ , which may be attributed to an optimal residual Al volume fraction. Failure mechanisms in this specimen were similar to those seen in quasi-static testing (see Figure 4.27a-c), but with far less  $\text{Al}_3\text{Ti}$  flat cleavage fracture. Figure 4.58a-c shows stair step fracture and Al reinforcement comparable to MIL-16, but with a general lack of  $\text{Al}_3\text{Ti}$ -Ti interface fracture. At 11% Al, in dynamic loading the ductile Al layer was still capable of preventing the failure mechanisms common of low  $K_{\text{IC}}$  materials, resulting in a drastic increase in fracture toughness.

The decrease in fracture toughness in MIL-3 to  $K_{\text{IC}} = 41.1 \text{ MPa}\sqrt{\text{m}}$  was caused by an increase in brittle flat-fracture in  $\text{Al}_3\text{Ti}$  layers due to decreased Al content (see Figure 4.59a). Though no cracking initiated at the  $\text{Al}_3\text{Ti}$  bilayer centerline (indicated by arrows in Figure 4.59b), the residual Al layer was no longer thick enough to prevent transverse fracture or

meandering intermetallic cracks. As seen in Figure 4.59c, the Al layer sheared where it was met by horizontal cracks.

A distinct change in failure mechanisms was observed in MIL-1 samples, which had an average fracture toughness of  $40.69 \text{ MPa}\sqrt{\text{m}}$ . Samples of this specimen showed the onset of  $\text{Al}_3\text{Ti}$  bilayer centerline fracture. However, this new mode of fracture did not contribute noticeably to a change in its toughness (only 5.3% lower than MIL-3, which showed no centerline fracture). Figure 4.60 is a collage of SEM micrographs detailing centerline, transverse, and inter- and intragranular cracking in the  $\text{Al}_3\text{Ti}$  layers. The results of dynamic 4PB testing indicate that MIL-3 and MIL-1 have too little residual Al content when compared to the performance of MIL-11.

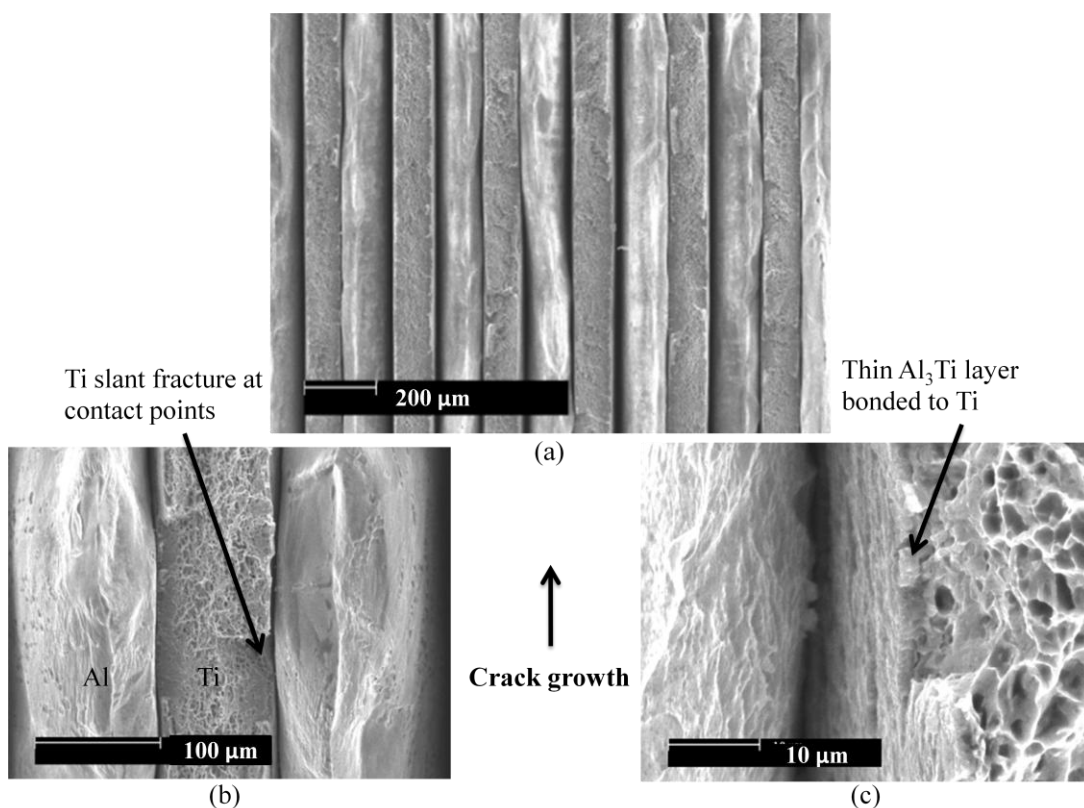


**Figure 4.55** – SEM micrographs of the fracture surface of MIL-48 in dynamic 4PB showing: (a) a fracture surface similar to quasi-static 4PB samples; (b) Al layer tearing, and Ti layer microvoid coalescence and slant fracture; (c) the thin intermetallic layer still bonded to the Ti layer.

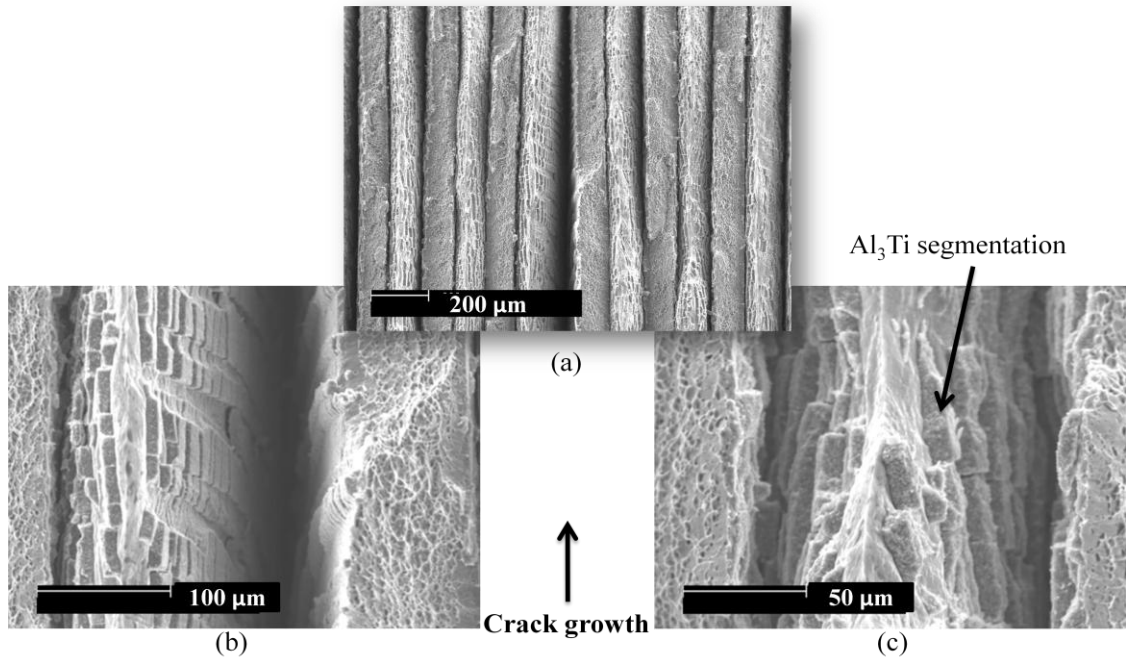


Figure 4.56 – SEM micrographs of the fracture surface of MIL-42 in dynamic 4PB showing: (a) wide-spread ply separation and intermetallic segmentation; (b) and (c) magnifications of intermetallic segmentation.

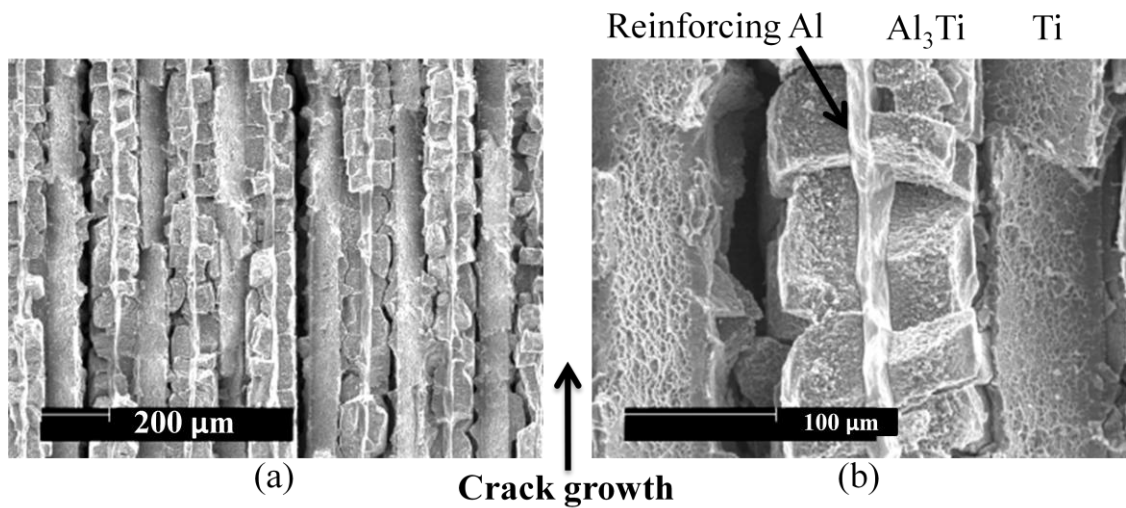
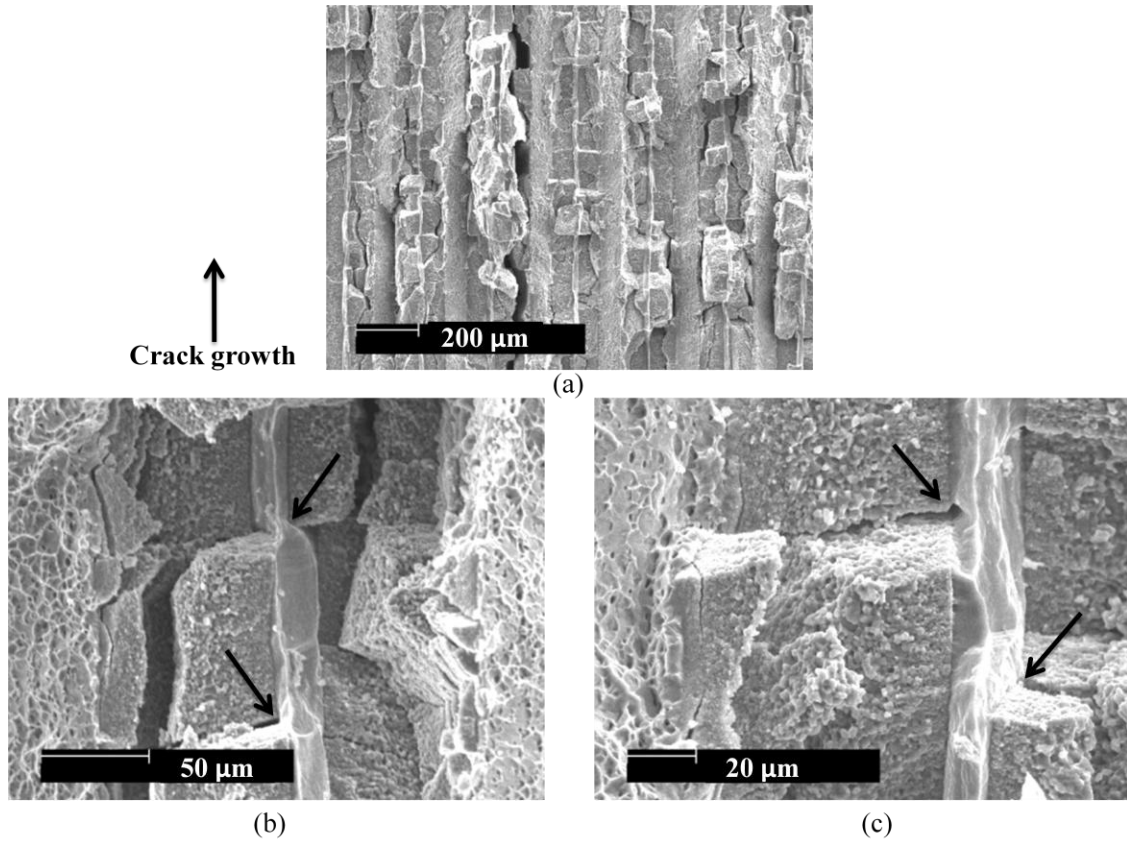


Figure 4.57 – SEM micrographs of the fracture surfaces of MIL-16 in the crack divider orientation after dynamic 4PB testing showing (a) stair-step Al<sub>3</sub>Ti fracture and slanted Ti fracture. (b) Magnification of (a). The Al layer provided enough ductile reinforcement to prevent flat cleavage fracture of the Al<sub>3</sub>Ti layers seen in specimens with less Al content.



**Figure 4.58 – SEM micrographs of the fracture surface of MIL-11 after dynamic 4PB testing showing: (a) less interfacial fracture than MIL-16; (b) and (c) the Al centerline prevented transverse fracture of the Al<sub>3</sub>Ti bilayers.**

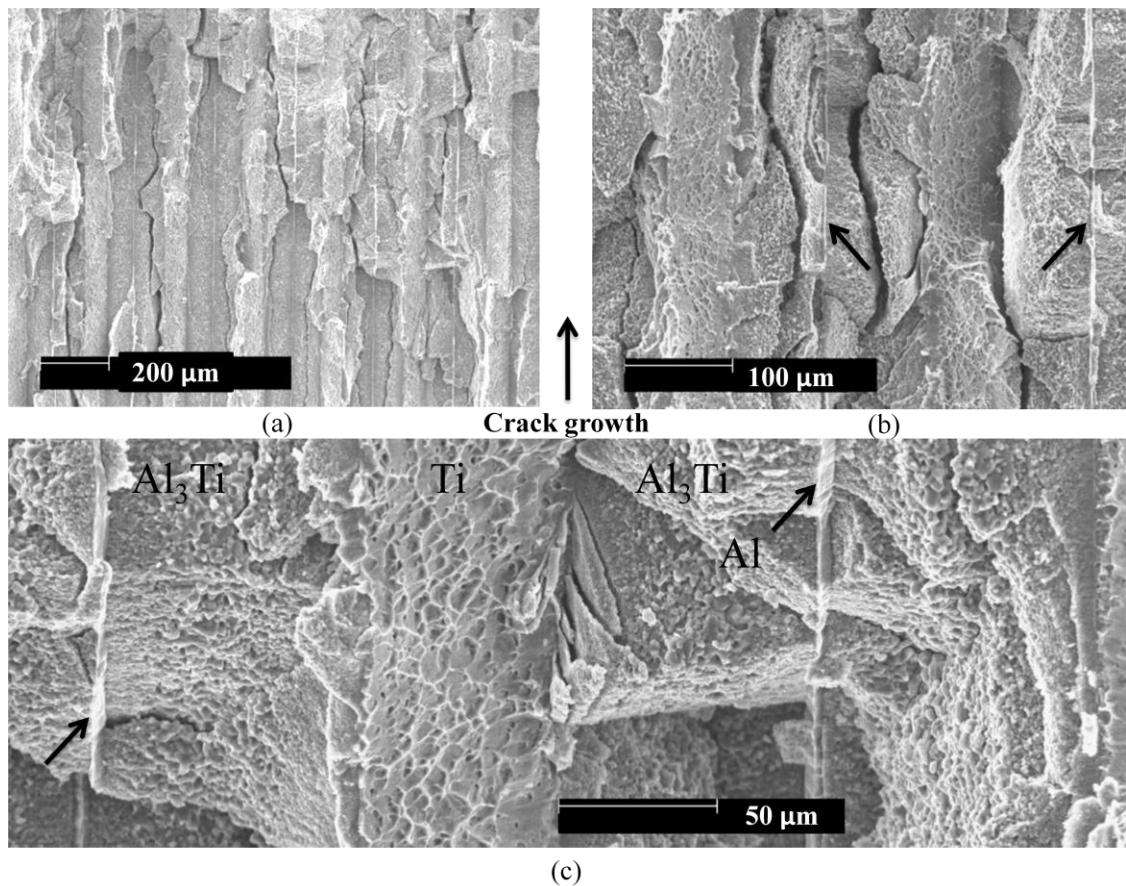
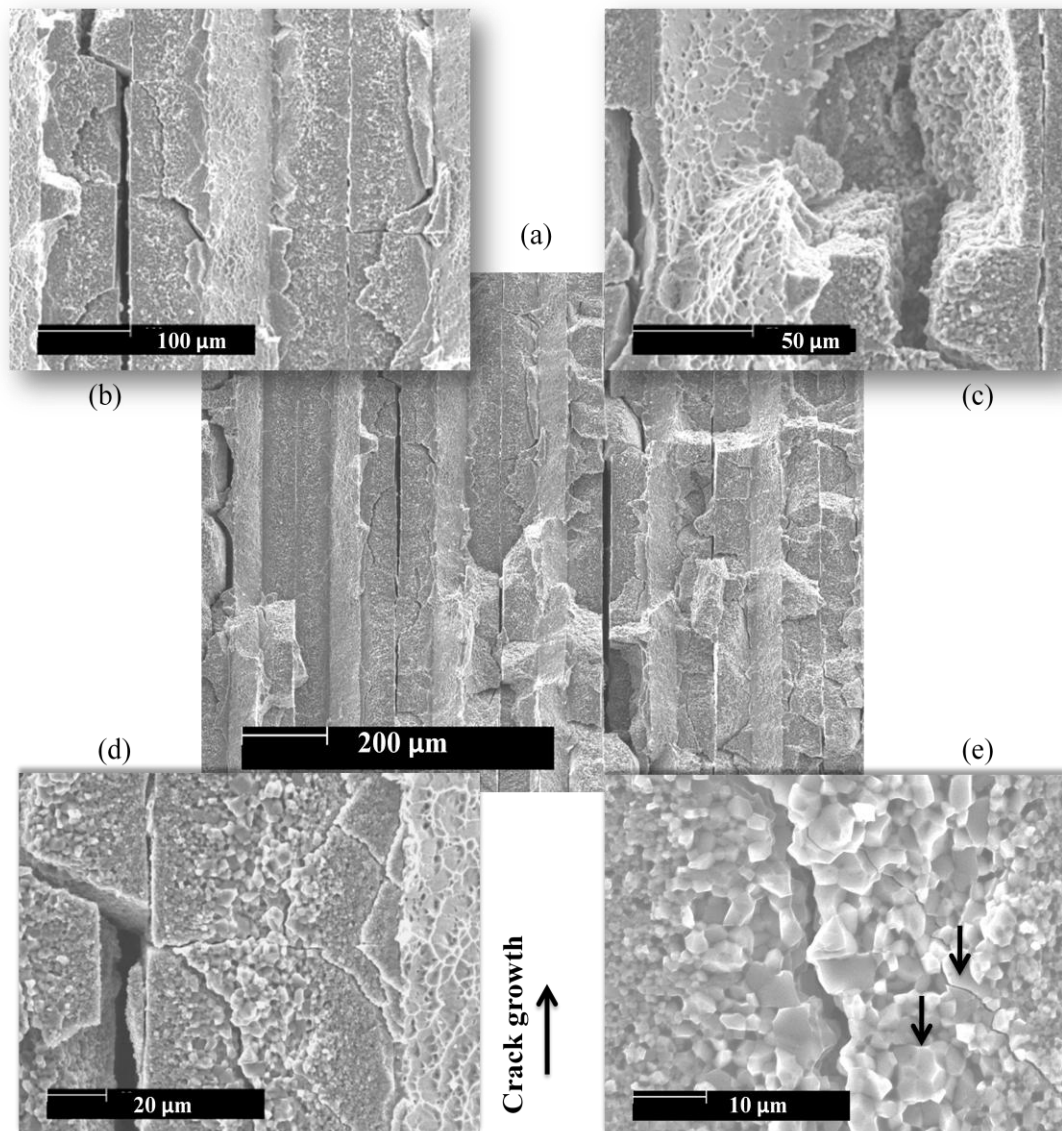


Figure 4.59 – SEM micrographs of the fracture surface of MIL-3 after dynamic 4PB testing showing: (a) increased presence of intermetallic flat cleavage fracture; (b) and (c) the residual Al centerline (indicated by arrows) was not thick enough to prevent transverse fracture in the  $\text{Al}_3\text{Ti}$  bilayers.



**Figure 4.60 – SEM micrographs of the fracture surface of MIL-1 after dynamic 4PB testing showing: (a), (b), (d) emergence of intermetallic centerline fracture as a primary failure mechanism; (c) plastic tearing of the Ti layer; (e) magnified image of (d) showing inter- and intragranular (arrows) cracking in the intermetallic phase.**

#### 4.2.4.2 Layers Perpendicular to the Applied Load

As seen in Figures 4.53 and 4.62, though the trend among crack-arrester samples was similar in dynamic and quasi-static testing, the trend itself did not indicate any significant changes in fracture toughness. Barring the comparatively poor performance of MIL-48 and MIL-16, the other four specimens showed average  $K_{IC}$  values that were almost the same (Table 4.8). Figure 4.61 shows a broken strain gage used to confirm the peak load method used to determine the critical crack initiation load (described in Section 3.3.4). The results indirectly validated the method used in quasi-static testing of crack-arrester samples (and by Zhang and Lewandowski [48]).

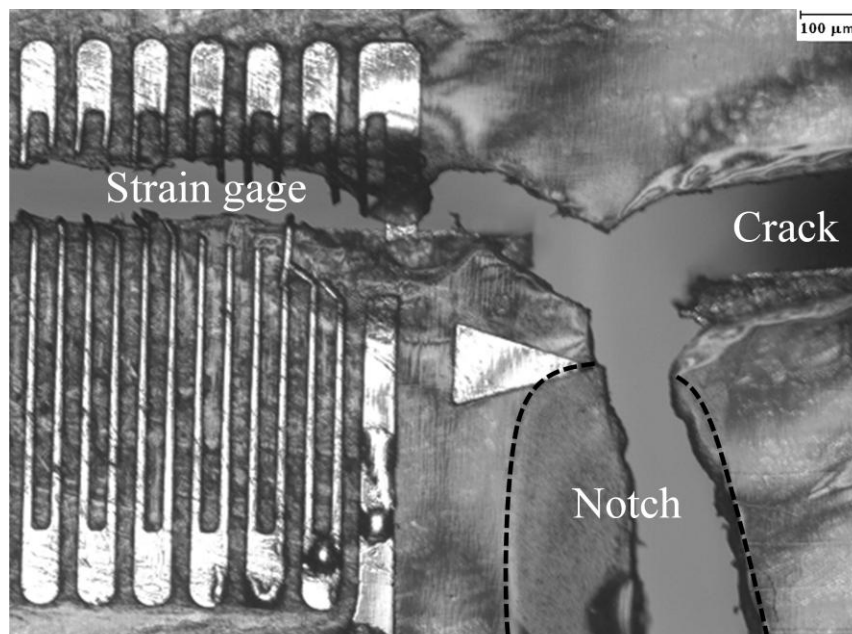


**Figure 4.61 – Optical micrograph of a broken strain gage spanning the transverse crack of a crack-arrester sample.**



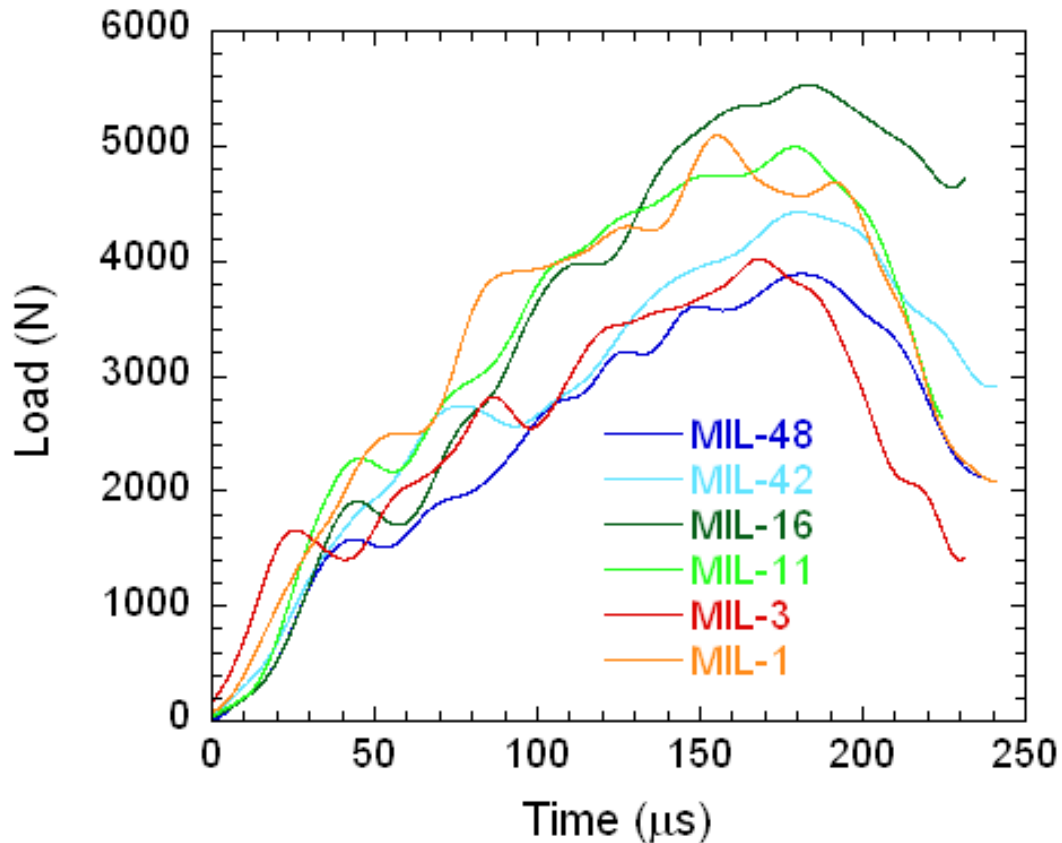


**Figure 4.62 – Representative load-time curves of each specimen tested under high strain-rate 4PB with layers oriented perpendicular to the applied load.**

MIL-48 and MIL-42 behaved very similarly both to each other and to their quasi-statically tested counterparts. With insignificant brittle intermetallic content, failure was primarily plastic deformation and propagation of a single major delamination crack at an Al- $\text{Al}_3\text{Ti}$  interface. Figure 4.63 shows side-by-side images recorded by the high-speed camera of a sample from each specimen well into the deformation process (crack onset typically initiated around 20 to 30  $\mu\text{s}$  after loading). Clearly there was very little difference, considering the large gap in fracture toughness:  $K_{\text{IC}}$  for MIL-48 was 17.58  $\text{MPa}\sqrt{\text{m}}$ ,  $K_{\text{IC}}$  for MIL-42 was 27.06  $\text{MPa}\sqrt{\text{m}}$ . This gap was most likely caused by poor bonding in the MIL-48 samples, which was the explanation put forth to explain the quasi-static results.

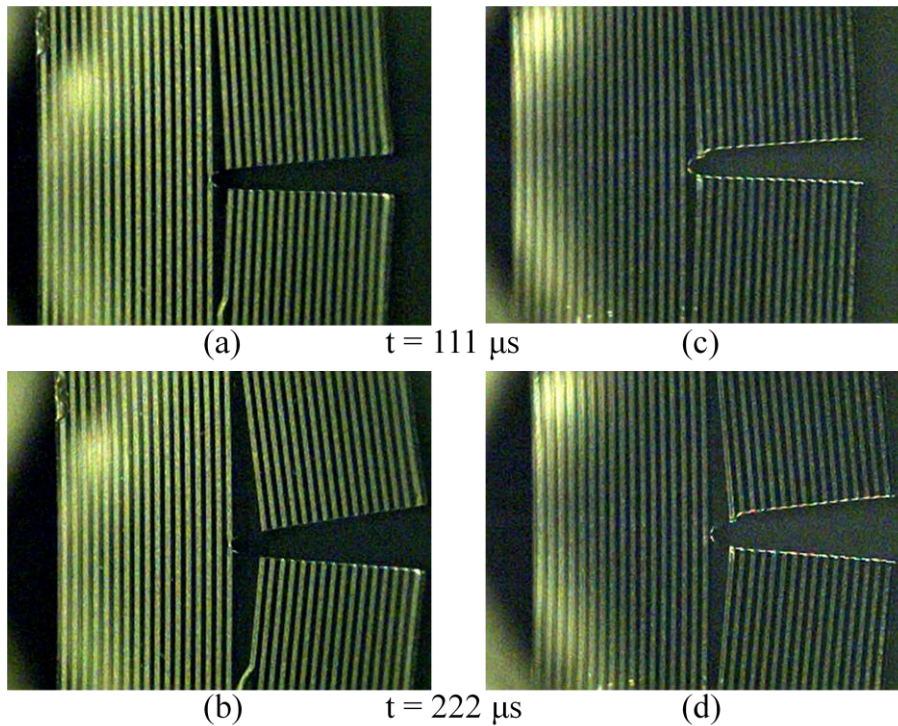


**Figure 4.63 – High-speed camera images showing the failure of (a, b) MIL-48 and (c, d) MIL-42 crack-arrester samples under dynamic 4PB.**

MIL-16 had an average fracture toughness of  $21.17 \text{ MPa}\sqrt{\text{m}}$ , which was roughly halfway between MIL-48 and MIL-42 and almost exactly twice that of the average fracture toughness it showed in quasi-static testing ( $10.76 \text{ MPa}\sqrt{\text{m}}$ ). The high-speed camera did not reveal any novel fracture mechanisms, but optical microscopy of the arrested tips of the transverse delamination crack revealed a substantial increase in microstructural damage (see Figure 4.64). The increase in deformation brought with it an increase in microstructural toughening mechanisms over what was seen in quasi-static testing; crack deflection by delamination ahead of the crack, shear band formation in the Ti and Al layers, and ductile layer crack bridging all exist to some extent.

In quasi-static 4PB, the appearance of additional crack deflection and bridging led to an increase in fracture toughness. Comparison of the failure mechanisms in Figure 4.64 reveals the same trend seen in Figure 4.37: increasing deformation with decreasing Al content,

except for MIL-1. However, MIL-11, MIL-3, and MIL-1 did not differ in fracture toughness to an extent consistent with the different degrees of microstructural damage each experienced. There is not even  $1.5 \text{ MPa}\sqrt{\text{m}}$  between the lowest and highest of the three. MIL-11 showed much less crack bridging than MIL-3, and MIL-1 showed increased levels of delamination with almost no crack bridging. The high speed photographs of MIL-11 in Figure 4.65a reveal the onset of secondary fracture growth above the notch, which was primarily plastic deformation of the Ti layers and transverse boundary cracking in the intermetallic layers (see Figure 4.65b). Figure 4.66 shows that MIL-3 damage was basically an exaggeration of MIL-11, with increased delamination fracture. Figure 4.67 shows the massive damage experienced by MIL-1 during dynamic 4PB. Even with all the apparent differences in failure mechanisms, fracture toughness seemed unaffected. It is possible that in high strain-rate 4PB, aluminum volume fractions below 11% show only minor differences in fracture toughness despite apparently large difference in failure.

This chapter is currently being prepared for submission for publication of the material. The dissertation author was the primary investigator and author of this material.

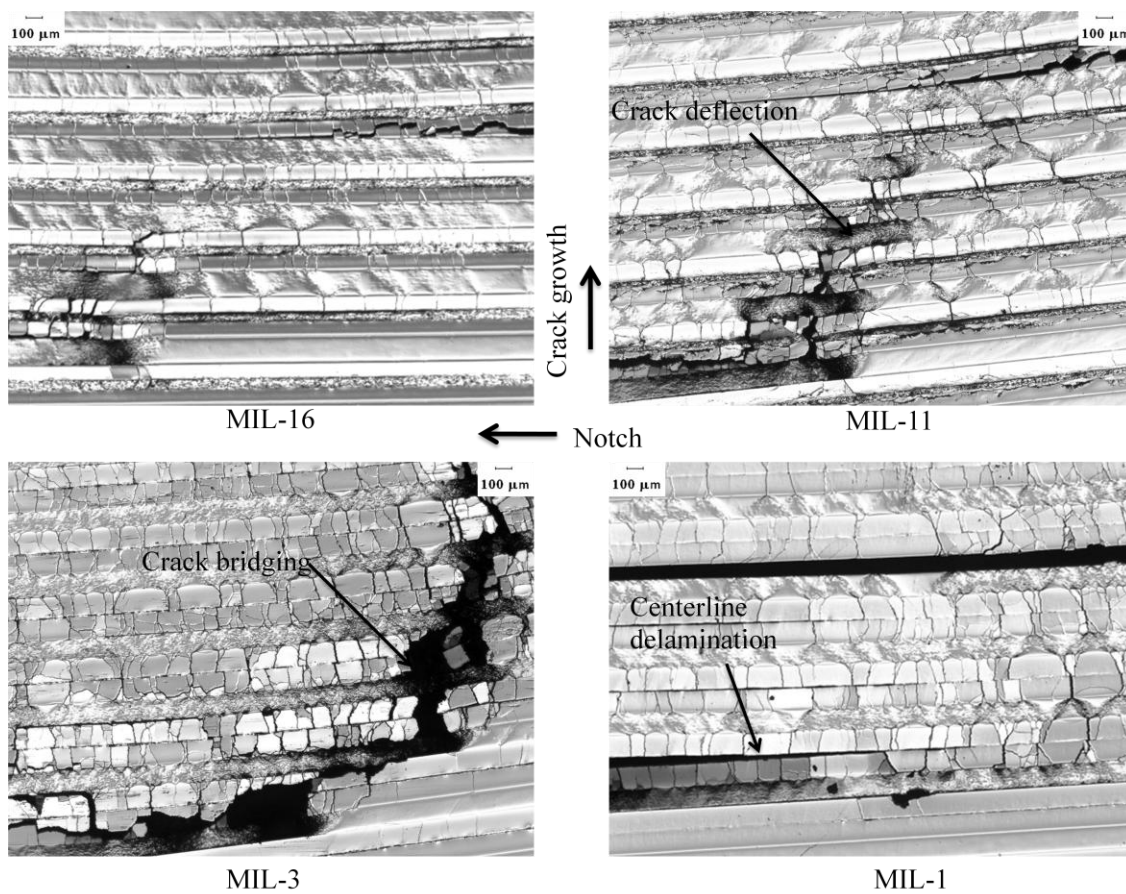
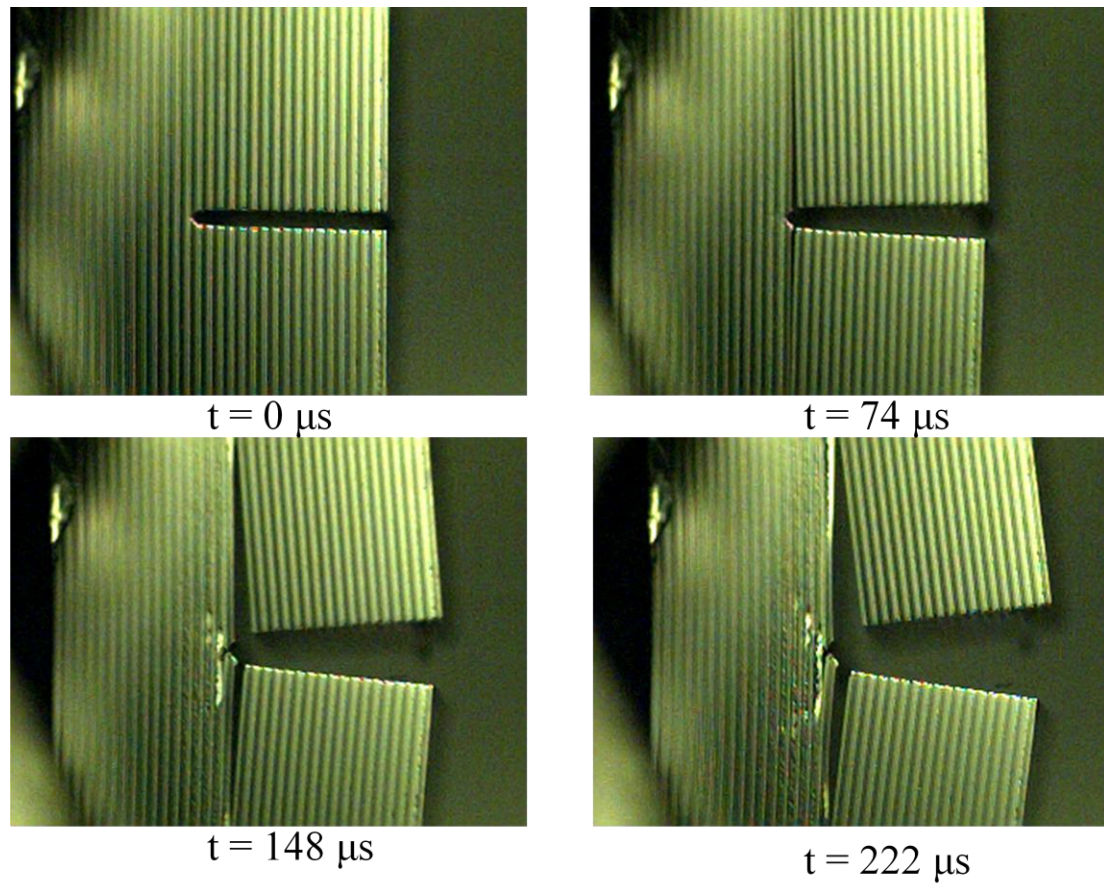
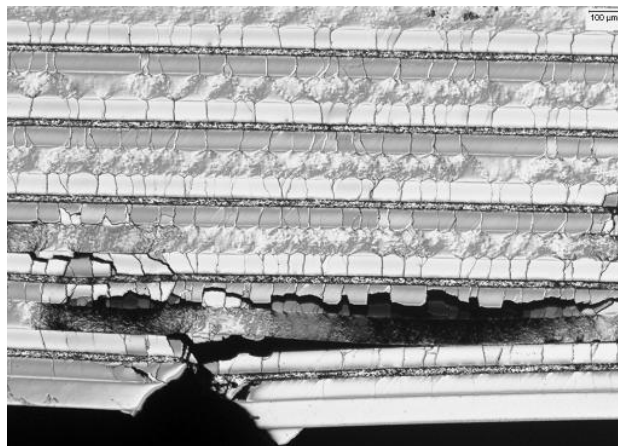


**Figure 4.64 – Optical micrographs depicting the evolution of failure of MIL-16, MIL-11, MIL-3, and MIL-1 crack-arrester samples under dynamic 4PB. Microstructural damage increases up to MIL-1, where delamination plays a larger role.**



(a)



(b)

Figure 4.65 – (a) High-speed camera images showing the failure of MIL-11 under dynamic 4PB. (b) Optical micrograph of the notch tip seen in (a) at 222 microseconds.



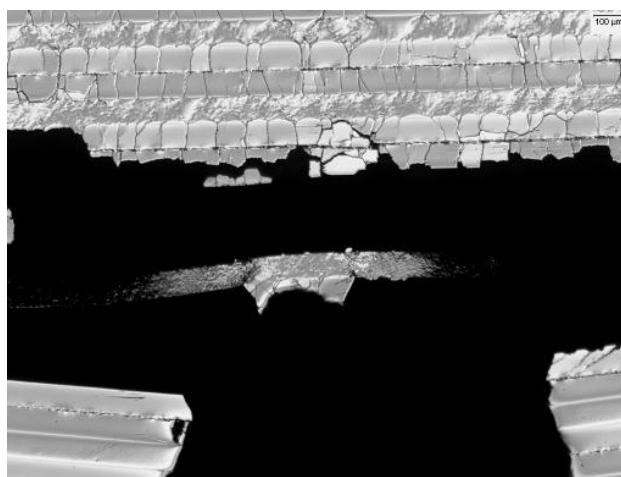
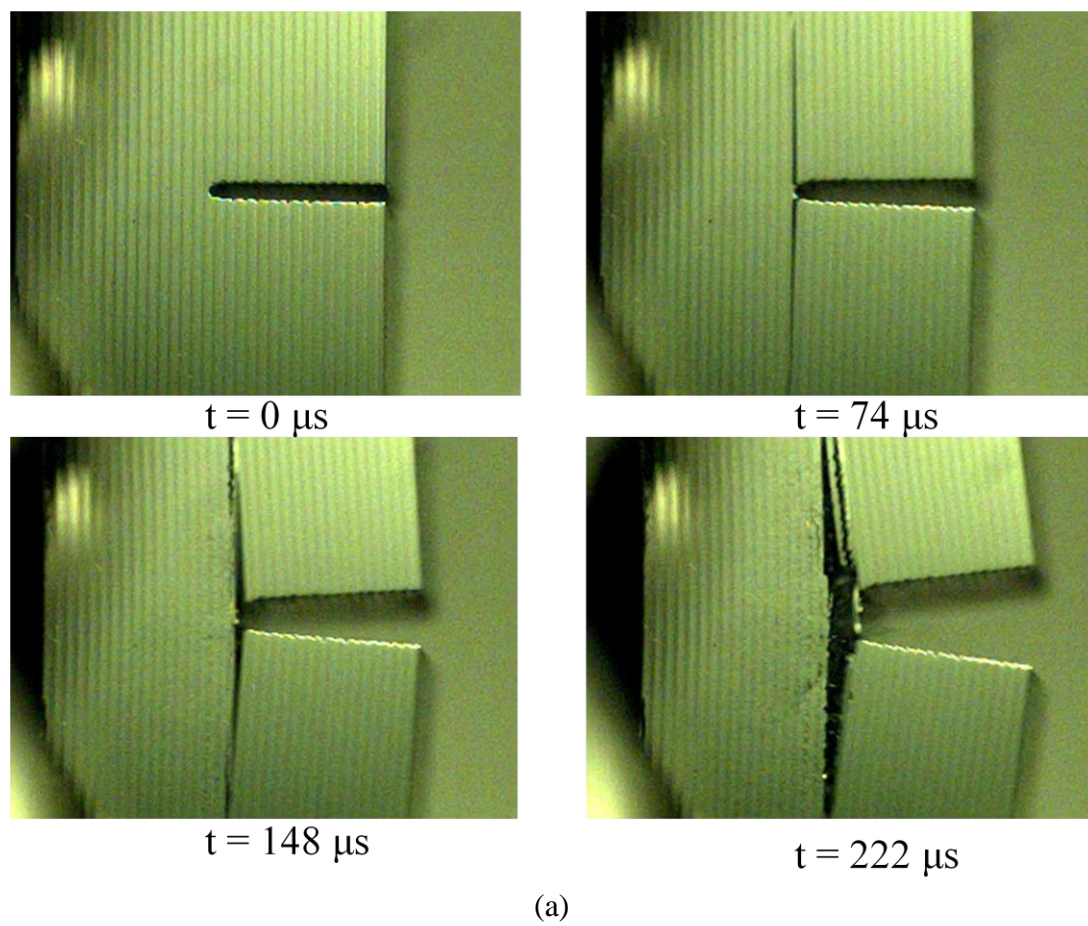
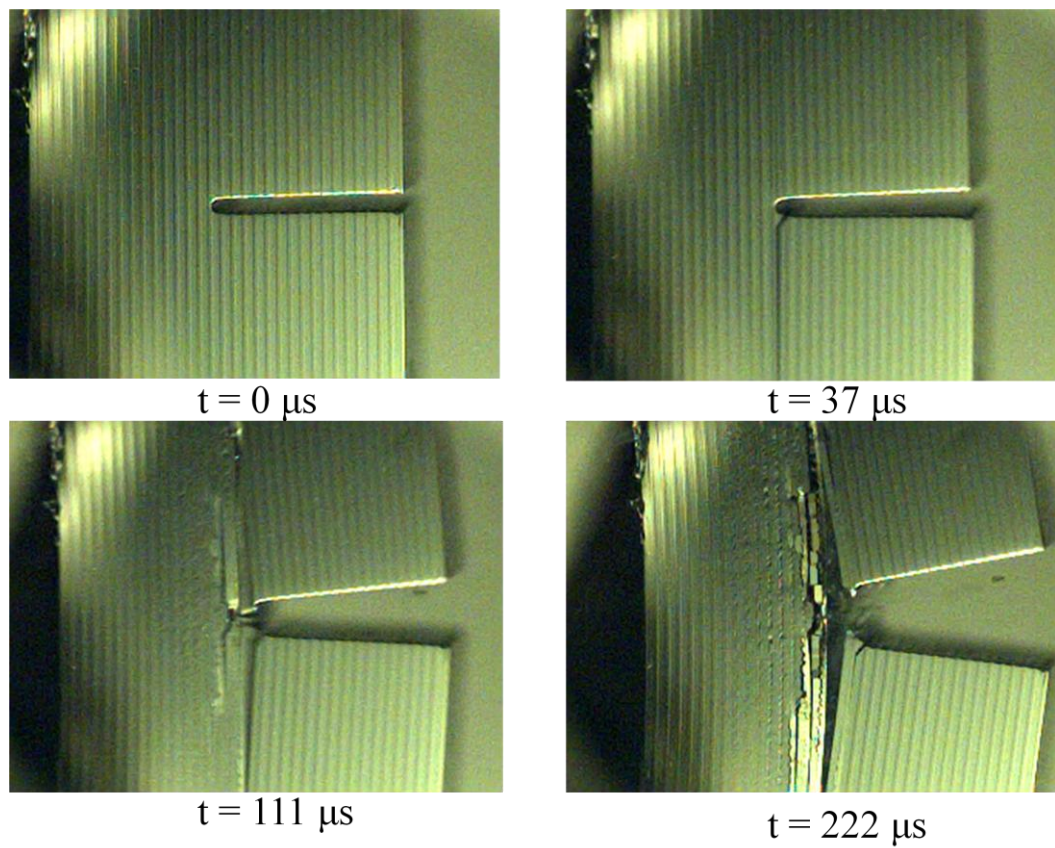


Figure 4.66 – (a) High-speed camera images showing the failure of MIL-3 under dynamic 4PB. (b) Optical micrograph of the notch tip seen in (a) at 222 microseconds.



(a)



(b)

**Figure 4.67– (a) High-speed camera images showing the failure of MIL-1 under dynamic 4PB. (b) Optical micrograph of the notch tip seen in (a) at 222 microseconds.**

## Chapter 5

### Summary and Conclusions

The effects of ductile phase volume fraction on the mechanical properties of Ti-Al<sub>3</sub>Ti metal-intermetallic laminate composites have been investigated, with the primary motivation of determining if the presence of a residual aluminum layer at the intermetallic centerline could potentially increase the performance of a Ti-6Al-4V based MIL composite. Therefore, the first objective of the present research was to produce several composites from initially identical foil stacks with final microstructures varying in aluminum content. The second objective was to perform a gamut of mechanical tests not solely to determine the composites' mechanical properties, but to examine performance trends between specimens.

#### 5.1 Specimens Produced

Six plates of a Ti-Al<sub>3</sub>Ti metal-intermetallic laminate composite were fabricated from commercially available Ti and Al foils of the same thickness by a controlled reaction process in open air that incorporated elevated temperatures and pressures. The processing parameters were varied such that each plate contained a different volume fraction of residual aluminum, with Al content determining specimen designation: MIL-48, MIL-42, MIL-16, MIL-11, MIL-3, MIL-1 (in order of decreasing aluminum content from 48% to 1%). It was shown by SEM EDS analysis that every specimen contained an aluminum layer at the intermetallic centerline, and that the centerline contained all the oxides and impurities initially present on the surfaces of the foils. SEM analysis of the microstructures of the specimens produced, in conjunction with the EDS data, confirmed the success of the reaction sintering process as compared to previous research utilizing the same techniques [8, 29, 30, 39, 42, 43, 50-52].



## 5.2 Compression Testing

Compression tests were performed at quasi-static and dynamic strain-rates ( $10^{-3}$  and  $10^3$  /s, respectively) with composite layers oriented parallel and perpendicular to the load axis. A summary of the results can be seen in Table 5.1 (combination of Tables 4.5 and 4.7).

Quasi-static compression trends:

Parallel orientation: increasing compressive strength with decreasing Al content, up to a maximum at ~11% Al.

Perpendicular orientation: increasing compressive strength with decreasing Al content, then a sharper increase below ~11% Al.

Dynamic compression trends:

Parallel orientation: similar to the quasi-static trend, but with slightly elevated values across the board, and a dramatic decrease at ~3% Al and increase at ~1% Al.

Perpendicular orientation: similar to the quasi-static trend for perpendicular samples, but with a lower strength at ~3% Al in keeping with the trend for dynamic testing of parallel samples.

**Table 5.1 – Summary of average yield stresses observed in quasi-static and dynamic compression**

Specimen	Al Volume Fraction	Yield Stress (MPa)			
		Parallel		Perpendicular	
		Quasi-Static	Dynamic	Quasi-static	Dynamic
MIL-48	0.481	337.4	497.3	404.47	586.7
MIL-42	0.419	483.9	664.9	450.6	631.8
MIL-16	0.157	841.47	776.6	665.93	893.3
MIL-11	0.109	999.2	1085.9	715.8	953.1
MIL-3	0.027	938.3	598.6	996.4	711.2
MIL-1	0.009	908.9	957.6	1047.9	1053

In the parallel orientation under quasi-static compression, shear fracture did not appear as a failure mechanism until Al content had reduced to 16%, corresponding to a large increase in strength. Interface cracking and decohesion occurred primarily at Ti-Al<sub>3</sub>Ti interfaces, rather than Al-Al<sub>3</sub>Ti (i.e. the intermetallic centerline). In the perpendicular orientation, MIL-3 and MIL-1 had the highest compressive strength, due to their high intermetallic content.

Under dynamic compression in both orientations, the failure mechanisms of each specimen corresponded roughly to those seen in quasi-static testing, though obviously greatly exaggerated because of the extreme strain-rates. It became apparent that the microstructure of MIL-3 was unstable when subjected to dynamic loads, as evidenced by the significant departures from trends observed in both quasi-static and dynamic loading. In general, the results indicated that MIL-11 had an optimal aluminum content for ample performance in both quasi-static and dynamic compression testing.

### 5.3 Four Point Bend Testing

Flexure tests were performed quasi-statically and dynamically with composite layers oriented parallel and perpendicular to the load axis. A summary of the results can be seen in Table 5.2 (combination of Tables 4.6 and 4.8).

Quasi-static trends:

Parallel orientation: predictably decreasing toughness with increasing intermetallic content. No apparent contribution to the trend by changing Al content.

Perpendicular orientation: low toughness at 16%Al, followed by slight increase between 11%Al and 3%Al, and a decrease at 1%Al.

Dynamic trends:

Parallel orientation: similar to the quasi-static trend, but with significantly elevated values across the board (double in most cases), and a dramatic increase at ~11%Al.

Perpendicular orientation: similar to the quasi-static trend for perpendicular samples.

For samples in the perpendicular orientation at both strain-rates, increasing microstructural damage corresponded to an increase in toughness. This was primarily because as damage increased, toughening mechanisms like ductile ligament bridging and crack deflection became more prevalent (indicative of R-curve behavior, though this was not specifically tested for).

For samples loaded parallel to their layers, the trend observed for failure mechanisms was increasing flat cleavage fracture of the intermetallic layers with decreasing Al content. This trend was seen at both strain-rates. As the aluminum centerline thinned, the intermetallic layers became less prone to the stair-step fracture indicative of crack front convolution. The evidence was clear from the dynamic results that the ideal residual aluminum volume fraction was ~11%.

**Table 5.2 - Summary of average toughness values observed in quasi-static and dynamic 4PB**

Specimen	Al Volume Fraction	$K_{IC}$ (MPa $\sqrt{m}$ )			
		Parallel		Perpendicular	
		Quasi-Static	Dynamic	Quasi-static	Dynamic
MIL-48	0.481	20.86	49.08	14.16	17.58
MIL-42	0.419	31.65	49.69	20.14	27.06
MIL-16	0.157	28.19	43.28	10.76	21.17
MIL-11	0.109	26.83	51.76	12.09	24.97
MIL-3	0.027	24.91	41.10	12.99	25.88
MIL-1	0.009	24.47	40.69	8.88	24.51

#### 5.4 Conclusions

The conclusions of this research can be summarized as follows:

1. By controlling the duration of the reactive foil sintering process, composites can be fabricated in which a predictable amount of residual aluminum remains.
2. SEM EDS analysis shows that the residual Al layer contains all the oxides and impurities initially present on the foils' surfaces.
3. Quasi-static compression tests performed on the composites clearly indicate a residual aluminum content at which the properties of the composite change.
4. Dynamic compression tests confirm the findings from quasi-static tests, and additionally clarify that below 11%Al the presence of the aluminum centerline may have deleterious effects on mechanical properties.
5. Quasi-static four point bend tests performed on the composites are less indicative of a change in toughness at 11%Al, but do show a sharp decrease at 16%Al when loaded perpendicular to the layers.
6. Dynamic four point bend tests show very similar results to the quasi-static tests, but with a clear maximum toughness at 11%Al in the parallel orientation. The results of

perpendicular samples are less conclusive, but confirm the results from quasi-static tests.

7. Fracture always initiated in the  $\text{Al}_3\text{Ti}$  layers, and interfacial cracking and separation showed varying degrees of preference between Al- $\text{Al}_3\text{Ti}$  and Ti- $\text{Al}_3\text{Ti}$  interfaces. In specimens with Al content between 16% and 3%, the residual Al at the intermetallic centerline served as a ductile reinforcing layer that mitigated  $\text{Al}_3\text{Ti}$  damage to some extent and prevented delamination. In MIL-1 samples, the Al layer was too thin and too highly concentrated with oxides and impurities to prevent  $\text{Al}_3\text{Ti}$  centerline fracture.
8. There is an amount of residual aluminum at the intermetallic centerline that increases (but more importantly does not decrease) the mechanical properties of the Ti- $\text{Al}_3\text{Ti}$  MIL composite. For this particular system with the initial foils used, that optimal Al content is at or near 11%.

This chapter is currently being prepared for submission for publication of the material.

The dissertation author was the primary investigator and author of this material.

## Chapter 6

### Future Work

Because it has been shown that leaving a layer of unreacted aluminum in the composite microstructure can be beneficial to the mechanical properties of the composite, the doorway has been opened to more extensive research in MIL composites incorporating a wider variety of metals, but specifically Ti-6Al-4V.

This chapter is currently being prepared for submission for publication of the material. The dissertation author was the primary investigator and author of this material.

## References

1. Kenneth S. Vecchio. "Synthetic Multifunctional Metallic-Intermetallic Laminate Composites." *JOM Journal of the Minerals, Metals and Materials Society*. Volume 57, Number 3 (2005): 25-31
2. T.C. Lu, A.G. Evans, R.J. Hecht and R. Mehrabian. "Toughening of MoSi<sub>2</sub> with a ductile (niobium) reinforcement." *Acta Metallurgica et Materialia*. Volume 39, Number 8 (1991): 1853-1862
3. P. Hing and G. W. Groves. "The strength and fracture toughness of polycrystalline magnesium oxide containing metallic particles and fibres." *Journal of Materials Science*. Volume. 7, Number 4 (1972): 427-434
4. W.O. Soboyejo, F. Ye, L-C. Chen, N. Bahtishi, D.S. Schwartz and R.J. Lederich. "Effects of reinforcement morphology on the fatigue and fracture behavior of MoSi<sub>2</sub>/Nb composites." *Acta Materialia*. Volume 44, Issue 5 (1996): 2027-2041
5. K.T. Venkateswara Rao, W.O. Soboyejo, and R.O. Ritchie. "Ductile-Phase Toughening and Fatigue-Crack Growth in Nb-Reinforced Molybdenum Disilicide Intermetallic Composites." *Metallurgical and Materials Transactions A*. Volume 23, Number 8 (1992): 2249-2257
6. M.F. Ashby, F.J. Blunt, M. Bannister. "Flow characteristics of highly constrained metal wires." *Acta Metallurgica*. Volume 37, Issue 7 (1989): 1847-1857
7. B.D. Flinn, C.S. Lo, F.W. Zok, A.G. Evans. "Fracture Resistance Characteristics of a Metal-Toughened Ceramic." *Journal of the American Ceramic Society*. Volume 76, Issue 2 (1993): 369 - 375
8. Fengchun Jiang and Kenneth S. Vecchio. "Fracture of ceramic-fiber-reinforced metallic-intermetallic laminate (CFR-MIL) composites." *In review*.
9. A. G. Evans. "The mechanical properties of reinforced ceramic, metal and intermetallic matrix composites." *Materials Science and Engineering A* 143 (1991): 63-76
10. B.J. Dalgleish, K.P. Trumble, A.G. Evans. "The strength and fracture of alumina bonded with aluminum alloys." *Acta Metallurgica*. Volume 37, Issue 7 (1989): 1923-1931
11. M.C. Shaw, D.B. Marshall, M.S. Dadkhah, A.G. Evans. "Cracking and damage mechanisms in ceramic/metal multilayers." *Acta Metallurgica et Materialia*. Volume 41, Issue 11 (1993): 3311-3322
12. J. Heathcote, G.R. Odette, G.E. Lucas, R.G. Rowe, D.W. Skelly. "On the micromechanics of low temperature strength and toughness of intermetallic/metallic microlaminate composites." *Acta Materialia*. Volume 44, Issue 11 (1996): 4289-4299

13. H.E. Deve and M.J. Maloney. "On the Toughening of Intermetallics With Ductile Fibers: Role of Interfaces." *Acta Metallurgica et Materialia*. Volume 39, Number 10 (1991): 2275-2284
14. M. Bannister and M.F. Ashby. "The Deformation and Fracture of Constrained Metal Sheets." *Acta Metallurgica et Materialia*. Volume 39, Number 11 (1991): 2575-2582
15. Zhang Jinxu, Hu Gengxiang, Wu Jiansheng. "Electron structure and bonding characteristics of Al<sub>3</sub>Ti intermetallic alloys." *Journal Of Materials Science Letters*. Volume 19 (2000): 1685 – 1686
16. Sauthoff, G., *Intermetallics*. 1995, Weinheim: VHC. 165
17. S. Djanarthany, J.C Viala, and J. Bouix. "An overview of monolithic titanium aluminides based on Ti<sub>3</sub>Al and TiAl." *Materials Chemistry and Physics* Volume 72 (2001): 301–319
18. Y. Kimura and D.P. Pope. "Ductility and toughness considerations in intermetallics." In: M.V. Nathal *et al.*, Editors, *Structural Intermetallics*, TMS, Warrendale, PA (1997): 99–106.
19. N.S. Stoloff. "Intermetallics: Mechanical Properties," In: K. H. Jurgen Buschow, Robert W. Cahn, Merton C. Flemings, Bernard Ilshner (print), Edward J. Kramer, Subhash Mahajan, and Patrick Veyssiere (updates), Editor(s)-in-Chief, *Encyclopedia of Materials: Science and Technology*, Elsevier, Oxford (2001): 4213-4225
20. J. Mackowiak and L.L. Shreir. "Kinetics of the Interaction of Ti(s) with Al(l)." *Journal of the Less-Common Metals*. Volume 14 (1968): 341-346.
21. J.L Murray. *Phase Diagrams of Binary Titanium Alloys*, ASM International, Metals Park, OH, 1987.
22. G.S. Brady and H. R. Clauser. *Materials Handbook*. 12<sup>th</sup> edition. 1986, New York: McGraw-Hill Book Company.
23. Polmear, I. J. *Light Alloys - Metallurgy of the Light Metals*, 3rd edition, Arnold, (1995)
24. D.E Alman, J.C Rawers, and J.A. Hawk. "Microstructural and failure characteristics of metal-Intermetallic layered sheet composites." *Metallurgical and Materials Transactions A* Volume 26, Number 3 (1995): 589-599.
25. D.E Alman, J.C Rawers, and J.A. Hawk. "Processing, Structure and Properties of Metal-Intermetallic Layered Composites." *Materials Science and Engineering A192/193* (1995): 624-632
26. J.C Rawers, D.E Alman, and J.A. Hawk. "Overview: Layered Metal/Intermetallic Composites Formed by SHS Reactions." *International Journal of Self-Propagating High-Temperature Synthesis*. Volume 2, Number 1 (1993): 12-24.



27. A. Jakob and M. O. Speidel. "Microstructure and tensile properties of TiAl compounds formed by reactive foil metallurgy." *Materials Science and Engineering A* 189 (1994): 129-136.
28. K. Mizuuchi, K. Inoue, M. Sugioka, M. Itami, and M. Kawahara. "Microstructure and mechanical properties of Ti-aluminides reinforced Ti matrix composites synthesized by pulsed current hot pressing." *Materials Science and Engineering A* 368 (2004): 260-268
29. David J. Harach and Kenneth S. Vecchio. "Microstructure evolution in metal-intermetallic laminate (MIL) composites synthesized by reactive foil sintering in air." *Metallurgical and Materials Transactions A* Volume 32A, Number 6 (2001): 1493-1505
30. David J. Harach. "Processing, properties, and ballistic performance of Ti-Al<sub>3</sub>Ti metal-intermetallic laminate (MIL) composites." PH.D thesis, University of California, San Diego, 2000.
31. J. D. Baird. "The formation of intermediate alloy layers in the inter-diffusion of metals." *Journal of Nuclear Energy, Part A: Reactor Science*. Volume 11(1960): 81-88.
32. M. Sujata, S. Bhargava, and S. Sangal. "Microstructural features of TiAl<sub>3</sub> base compounds formed by reaction synthesis." *ISIJ International*. Volume 36, Number 3 (1996): 255-262.
33. M. Sujata, S. Bhargava, and S. Sangal. "On the formation of TiAl<sub>3</sub> during reaction between solid Ti and liquid Al." *Journal of Materials Science Letters*. Volume 16 (1997): 1175-1178.
34. J. Mackowiak, and L.L. Shreir. "The nature and growth of interaction layers formed during the reaction between solid titanium and liquid aluminum." *Journal of the Less-Common Metals*. Volume 1 (1959): 456-466.
35. R.O. Ritchie. "Mechanisms of Fatigue Crack Propagation in Metals, Ceramics and Composites: Role of Crack Tip Shielding." *Materials Science and Engineering*. A 103 (1988): 15-28
36. D.R. Lesuer, C.K. Syn, O.D. Sherby, J. Wadsworth, J.J. Lewandowski, and W.H. Hunt. "Mechanical behavior of laminated metal composites." *International Materials Reviews*. Volume 41, Number 5 (1996): 169-197
37. L.S. Sigl, P.A. Mataga, B.J. Dalgleish, R.M. McMeeking and A.G. Evans. "On the toughness of brittle materials reinforced with a ductile phase." *Acta Metallurgica* Volume 36, Number 4 (1998): 945-953
38. R.O. Ritchie. "Mechanisms of fatigue-crack propagation in ductile and brittle solids." *International Journal of Fracture*. Volume 100 (1999): 55-83.

39. Raghavendra R. Adharapurapu, Kenneth S. Vecchio, Ashish Rohatgi, and Fengchun Jiang. "Fracture of Ti-Al<sub>3</sub>Ti Metal-Intermetallic Laminate Composites: Effects of Lamination on Resistance Curve Behavior." *Metallurgical and Materials Transactions A*. Volume 36A, Number 11 (2005): 3217-3236
40. M. Lugovy, V. Slyunyayev, N. Orlovskaya, G. Blugan, J. Kuebler, M. Lewis. "Apparent fracture toughness of Si<sub>3</sub>N<sub>4</sub>-based laminates with residual compressive or tensile stress in surface layers." *Acta Materialia*. Volume 53 (2005): 289-296.
41. George J. Dvorak. "Composite materials: Inelastic behavior, damage, fatigue and fracture." *International Journal of Solids and Structures*. Volume 37 (2000): 155-170
42. Tiezheng Li, Fengchun Jiang, Eugene A. Olevsky, Kenneth S. Vecchio, Marc A. Meyers. "Damage evolution in Ti6Al4V–Al<sub>3</sub>Ti metal-intermetallic laminate composites." *Materials Science and Engineering A* 443 (2007): 1–15
43. Raghavendra R. Adharapurapu, Kenneth S. Vecchio, Ashish Rohatgi, and Fengchun Jiang. "Effects of ductile laminate thickness, volume fraction, and orientation on fatigue-crack propagation in Ti-Al<sub>3</sub>Ti metal-intermetallic laminate composites." *Metallurgical and Materials Transactions A* Volume 36A, Number 6(2005): 1595-1608
44. H. E. Deve, A. G. Evans, G. R. Odette, R. Mehrabian, M. L. Emiliani and R. J. Hecht. "Ductile reinforcement toughening of  $\gamma$ -TiAl: Effects of debonding and ductility." *Acta Metallurgica et Materialia*. Volume 38 (1990): 1491-1502.
45. D. R. Bloyer, K. T. V. Rao, and R. O. Ritchie. "Fracture Toughness and R-Curve Behavior of Laminated Brittle-Matrix Composites," *Metallurgical and Materials Transactions A*. Volume 29A, Number 10 (1998): 2483-2496.
46. S. Zheng, C.T. Sun. "Delamination interaction in laminated structures." *Engineering Fracture Mechanics*. Volume 59 (1998): 225-240.
47. Dong-Woo Shin, Hai Guo. "A fracture model and prediction of mechanical behavior in Si<sub>3</sub>N<sub>4</sub> laminate composites." *Journal of Ceramic Processing Research*. Volume 6, Number 3 (2005): 266-270
48. J. Zhang and J. J. Lewandowski. "Delamination study using four-point bending of bilayers." *Journal of Materials Science*. Volume 32, Number 14 (1997): 3851-3856
49. J. Rawers and K. Perry. "Crack initiation in laminated metal-intermetallic composites." *Journal of Materials Science*. Volume 31 (1996): 3501-3506
50. Ashish Rohatgi, David J. Harach, Kenneth S. Vecchio, Kenneth P. Harvey. "Resistance-curve and fracture behavior of Ti–Al<sub>3</sub>Ti metallic–intermetallic laminate (MIL) composites." *Acta Materialia* Volume 51, Issue 10 (2003): 2933-2957
51. Fengchun Jiang, Robb M. Kulin and Kenneth S. Vecchio. "Mechanical Properties and Damage Evolution of Ti-Al<sub>3</sub>Ti Metallic-Intermetallic Laminate (MIL) Composites under Quasi-static and High Strain-Rates." *In Review*

52. Tiezheng Li, Eugene A. Olevsky, Marc A. Meyers. "The development of residual stresses in Ti6Al4V-Al<sub>3</sub>Ti metal-intermetallic laminate (MIL) composites." *Materials Science and Engineering A* 473 (2008): 49–57.
53. ASTM E399-90. "Standard Test method for plane strain fracture toughness of metallic materials." *Annual Book of ASTM Standards, ASTM International*. Volume 3, Number 1 (2002)
54. ASTM C1421-99. "Standard test methods for determination of fracture toughness of advanced ceramics at ambient temperature." *Annual Book of ASTM Standards, ASTM International*. Volume 3, Number 1 (2002)
55. Robb M. Kulin, Fengchun Jiang, and Kenneth S. Vecchio. "Aging and loading rate effects on the mechanical behavior of equine bone." *JOM Journal of the Minerals, Metals and Materials Society*. Volume 60, Number 6 (2008): 39-44
56. K. S. Vecchio and F. Jiang. "Improved pulse shaping to achieve constant strain rate and stress equilibrium in split-Hopkinson pressure bar testing." *Metallurgical and Materials Transactions* Volume 35A (2007): 313-317
57. D.J. Frew, M.J. Forrestal and W. Chen. "Pulse Shaping Techniques for Testing Elastic-plastic Materials with a Split Hopkinson Pressure Bar." *Experimental Mechanics*. Volume 45, Number 2 (2005): 186-195
58. Robb M. Kulin, Po-Yu Chen, Fengchun Jiang, Joanna McKittrick and Kenneth S. Vecchio. "Dynamic fracture resilience of elk antler: Biomimetic inspiration for improved crashworthiness." *JOM Journal of the Minerals, Metals and Materials Society*. Volume 62, Number 1(2010): 41-46
59. Robb Kulin. "On the dynamic behavior of mineralized tissues." Doctorate Thesis. University of California, San Diego. 2010.
60. Robb M. Kulin, Fengchun Jiang, Kenneth S. Vecchio. "Loading Rate Effects on the R-curve Behaviour of Cortical Bone." *In Review*.